

An introduction to Isogeometric Analysis with Matlab[®] implementation: FEM and XFEM formulations

Vinh Phu Nguyen^{a,1}, Robert N. Simpson^{a,2}, Stéphane P.A. Bordas^{a,3,*}, Timon Rabczuk^{b,4}

^a*School of Engineering, Institute of Mechanics and Advanced Materials, Cardiff University, Queen's Buildings, The Parade, Cardiff CF24 3AA*

^b*Institute of Structural Mechanics, Bauhaus-Universität Weimar, Marienstraße 15 99423 Weimar*

Abstract

Isogeometric analysis (IGA) is a fundamental step forward in computational mechanics that offers the possibility of integrating methods for analysis into Computer Aided Design (CAD) tools and vice versa. The benefits of such an approach are evident, since the time taken from design to analysis is greatly reduced leading to large savings in cost and time for industry. The tight coupling of CAD and analysis within IGA requires knowledge from both fields and it is one of the goals of the present paper to outline much of the commonly used notation. In this manuscript, through a clear and simple Matlab[®] implementation, we present an introduction to IGA applied to the Finite Element (FE) method and related computer implementation aspects. Furthermore, implementation of the extended IGA which incorporates enrichment functions through the partition of unity method (PUM) is also presented, where several fracture examples are illustrated in both two-dimensions and three-dimensions. The open source Matlab[®] code which accompanies the present paper can be applied to one, two and three-dimensional problems for linear elasticity, linear elastic fracture mechanics and Poisson problems with or without enrichment.

Keywords: isogeometric analysis, linear elasticity, Matlab[®], spline, NURBS, finite elements, partition of unity, enrichment, 3D cracks, boundary conditions, CAD

*Corresponding author

¹nvinhphu@gmail.com

²SimpsonR4@cardiff.ac.uk

³stephane.bordas@alum.northwestern.edu

⁴timon.rabczuk@uni-weimar.de

1. Introduction

1.1. Underlying concepts of isogeometric analysis

The predominant technology that is used by CAD to represent complex geometries is the Non-Uniform Rational B-spline. This allows certain geometries to be represented exactly that can only be approximated by polynomial functions, such as conic and circular sections. There is a vast array of literature focused on Non-Uniform Rational B-splines (NURBS) (e.g. [1], [2]) and as a result of several decades of research, many efficient computer algorithms exist for their fast evaluation and refinement. The key observation that was made by Hughes et al. [3] was that NURBS can not only be used to describe the geometry of a problem, but can also be used to construct finite approximations for analysis and coined the phrase ‘Isogeometric Analysis’ (IGA). Since this seminal paper, a monograph has been published entirely on the subject [4] and applications have been found in several fields including structural mechanics, solid mechanics, fluid mechanics and contact mechanics. This section gives an overview of some of these recent developments while outlining the benefits that have been realised through IGA.

1.2. Applications

In contact formulations using conventional geometry discretisations, faceted surfaces are often found on contact surfaces that can lead to jumps and oscillations in tractions unless very fine meshes are used. The benefits of using NURBS over such an approach are therefore evident, since the contact surface is now smooth leading to more physically accurate contact stresses. Recent work in this area includes [5, 6, 7, 8]. Another area where IGA has shown advantages over traditional approaches is optimisation problems [9, 10, 11, 12]. IGA is particularly suited to such problems due to the tight coupling with CAD models and offers an extremely attractive approach for industrial applications. Moreover, it is found that certain numerical methods can be integrated with CAD very tightly where only a surface or boundary representation is required. Simpson et al. [13] demonstrated an isogeometric boundary element method where no meshing is required at all allowing CAD models to be used directly for analysis. Shell and plate formulations also offer such an approach [14, 15, 16, 17, 18] where beneficial properties have been demonstrated over conventional approaches. Furthermore, the smoothness of the NURBS basis functions allows for a straightforward construction of plate/shell elements. The smoothness of NURBS basis functions is attractive for analysis of fluids [19, 20] and for fluid-structure interaction problems [21, 22]. In addition, due to the ease of constructing high order continuous basis functions, IGA has been used with great success in solving PDEs that incorporate fourth order (or higher) derivatives of the field variable such as the Hill-Cahnard equation [23], explicit gradient damage models [24] and gradient elasticity [25]. NURBS have also shown advantageous properties for structural vibration problems [26] with the mathematical properties of IGA studied in detail by Evans et al.[27].

1.3. Shortcomings of NURBS and alternative geometry discretisations

NURBS are ubiquitous in CAD but have been shown to exhibit major shortcomings, such as the inability to produce watertight geometries with no gaps and overlaps which often complicate mesh generation. From the perspective of analysis however, perhaps the most major shortcoming is the tensor product structure of NURBS where refinement is found to be a global operation. Refinement algorithms required for error estimation and adaptivity are therefore inefficient. As a solution to this, T-splines [28] have been recently developed to overcome the limitations of NURBS while making use of existing NURBS algorithms. T-splines correct the deficiencies of NURBS since local refinement and coarsening is permitted, and gap/overlaps are precluded. However, [29] note that linear independence of the T-spline basis functions is not guaranteed on generic T-meshes. Therefore, [30] propose analysis-suitable T-splines, a mildly restricted subset of T-splines which meets the demands of both design and analysis. Utilization of T-splines in an IGA framework has been illustrated in [31, 32]. Scott et al.[33] have shown that through an efficient Beziér extraction process, T-splines can be incorporated efficiently into existing FE codes. Alternatives to the T-spline are the polycube spline [34], PHT-splines [35] or LR-spline [36] among others. The PHT-spline (polynomial spline over hierarchical T-meshes) was extended to rational splines and applied by [37, 38] to problems in elasticity for continua and thin structures. Adaptive refinement with PHT-splines is particularly simple. Though T-splines allow for local adaptive refinement, the complexity of knot insertion under adaptive refinement is complex, particularly in 3D. In the computer aided geometric design, patching multiple NURBS to form complex topology is not easy for certain continuity between adjacent patches should be maintained. Trimming technique provides a promising alternative for representing complex NURBS domains. In [39] a trimmed surface based analysis framework has been proposed.

1.4. Discontinuities

IGA has been applied to cohesive fracture [40] with a framework for modeling debonding material interfaces using NURBS and propagating cohesive cracks using T-splines. The method hinges on the ability to specify the continuity of NURBS/T-splines through a process known as knot insertion. As an extension of the eXtended Finite Element Method (XFEM) [41], IGA has been applied to fracture using the partition of unity method (PUM) to capture two dimensional strong discontinuities and crack tip singularities efficiently [42, 43].

1.5. Alternatives to IGA

Other techniques which integrate CAD and analysis have been demonstrated, such as the use of subdivision surfaces to model shells [44], NURBS-enhanced finite elements [45, 46] and NURBS for BEM shape optimisation [47]. Immersed boundary methods such as the structured XFEM, see e.g., [48] and references therein, the finite cell method [49] are yet

another alternatives to tying numerical simulations and CAD. But we must recognise that for the fields of CAD and analysis to work seamlessly, the technologies used for discretisation in each must either be the same or be converted easily between the two. For this reason, the idea of IGA is preferred and is anticipated as having the greatest impact on industry for engineering simulations.

1.6. Available implementations

Some implementation aspects of IGA have been reported in [4] and more recently, an open source IGA Matlab[®] code has been described in [50] with a restriction to scalar PDEs. An additional open source IGA code written in Matlab[®] is given in [51] with details of incorporating IGA within an object-oriented FE code discussed in [52]. Implementation details for enriched formulations within an IGA framework are reported in [53] using commercial FE software.

1.7. Outline

In this paper, we present in detail an isogeometric Bubnov-Galerkin finite element method applied for two- and three-dimensional elasto-static problems and traction free crack modelling problems. The discussion is confined to NURBS for the sake of simplicity. The remainder of the paper is structured as follows: Section 2 presents the basis of B-splines. Section 3 describes NURBS curves, surfaces and solids. The finite element formulation using NURBS is treated in Section 4 together with Matlab[®] implementation details. An extended isogeometric formulation based on the concept of PUM is a subject of Section 5. Numerical examples are given in Section 6.

2. B-splines

In this section a brief discussion on B-splines is given since the same technology is utilised for more advanced geometrical functions (e.g. NURBS, T-splines). We begin with some basic concepts and define commonly used notations and introduce B-spline curves and surfaces. Most of the algorithms used to implement B-spline and NURBS in our Matlab[®] code are described in the book [1].

2.1. Knot vectors

A *knot vector* (defined for a given direction) is a sequence in ascending order of parameter values, written $\Xi = \{\xi_1, \xi_2, \dots, \xi_{n+p+1}\}$ where ξ_i is the i th knot, n is the number of basis functions and p is the polynomial order. The knot vector divides the parametric space into intervals usually referred to as *knot spans*. Consecutive knots can have the same value i.e., more than one knot can be located at the same coordinate in the parametric space. A number of coinciding knots is referred to as a knot with a certain *multiplicity*. A knot vector is said to be *open* if its first and last

knots have multiplicity equal to the polynomial order plus one ($p + 1$). An important property of open knot vectors is that the resulting basis functions are interpolatory at the ends of the parametric space. A *uniform knot vector* is associated to evenly distributed knots. Otherwise it is said to be a *non-uniform knot vector*.

2.2. Basis functions

Given a knot vector Ξ , the B-spline basis functions are defined recursively starting with the zeroth order basis function ($p = 0$) as

$$N_{i,0}(\xi) = \begin{cases} 1 & \text{if } \xi_i \leq \xi < \xi_{i+1}, \\ 0 & \text{otherwise.} \end{cases} \quad (1)$$

and for a polynomial order $p \geq 1$

$$N_{i,p}(\xi) = \frac{\xi - \xi_i}{\xi_{i+p} - \xi_i} N_{i,p-1}(\xi) + \frac{\xi_{i+p+1} - \xi}{\xi_{i+p+1} - \xi_{i+1}} N_{i+1,p-1}(\xi). \quad (2)$$

This is referred to as the **Cox-de Boor recursion formula**. Note that when evaluating these functions, ratios of the form $0/0$ are defined as zero.

2.2.1. Properties

1. B-spline basis functions constitute a partition of unity $\sum_{i=1}^n N_{i,p}(\xi) = 1$
2. Each basis function is nonnegative over the entire domain $N_{i,p}(\xi) \geq 0, \forall \xi$
3. B-spline basis functions are linearly independent i.e., $\sum_{i=1}^n \alpha_i N_i(\xi) = 0 \Leftrightarrow \alpha_k = 0, k = 1, 2, \dots, n$
4. The support of a B-spline function of order p is $p + 1$ knot spans i.e., $N_{i,p}$ is non-zero over $[\xi_i, \xi_{i+p+1}]$.
5. Basis functions of order p have $p - m_i$ continuous derivatives across knot ξ_i where m_i is the multiplicity of knot ξ_i .
6. Scaling or translating the knot vector does not alter the basis functions.
7. B-spline basis are generally only approximants and not interpolants. That is, they do not satisfy the Kronecker delta property $N_{i,p}(\xi_j) \neq \delta_{ij}$. Only in the case $m_i = p$, then $N_{i,p}(\xi_i) = 1$.

Figure 1 illustrates linear and quadratic B-spline basis functions for a uniform knot vector while Figure 2 illustrates similar functions for an open non-uniform knot vector. Note that the basis functions are interpolatory at each end of the interval and also at $\xi = 4$, the location of a repeated knot where only C^0 -continuity is attained. Elsewhere, the functions are C^1 -continuous. The ability to control continuity by means of knot insertion is particularly useful for modeling discontinuities such as cracks or material interfaces [40] although it requires knots to be placed on the

discontinuity surfaces which is not as flexible as PUM enrichment. Property 2 has implications in developing lumped mass matrices in transient analysis. Property 4 at first glance would give an impression that the bandwidth of the discrete matrix depends on the order of the basis. However the bandwidth is always $2p + 1$. See for the example, in Fig. (2), that $N_{3,2}$ intersects with 5 ($= 2 \times 2 + 1$) other basis functions including itself. Property 7 requires special techniques to treat Dirichlet boundary conditions which will be discussed in Section 4.8. It should be emphasized that, in contrast to meshless basis, B-spline basis satisfy a so-called weak Kronecker delta property. We refer to Section 4.8 for details.

[Figure 1 about here.]

[Figure 2 about here.]

2.2.2. Derivatives

The first derivative of a B-spline basis function is given by

$$\frac{d}{d\xi} N_{i,p}(\xi) = \frac{p}{\xi_{i+p} - \xi_i} N_{i,p-1}(\xi) - \frac{p}{\xi_{i+p+1} - \xi_{i+1}} N_{i+1,p-1}(\xi). \quad (3)$$

Derivatives of higher order can be found in [1] but for the purpose of this paper, first derivatives are sufficient for all examples given.

2.3. B-spline curves

Let the number of space dimensions be denoted by d . Given n B-splines basis functions $N_{i,p}$ and n control points $\mathbf{B}_i \in \mathbb{R}^d$, a piecewise-polynomial B-spline curve is constructed as

$$\mathbf{C}(\xi) = \sum_{i=1}^n N_{i,p}(\xi) \mathbf{B}_i. \quad (4)$$

This equation can be interpreted as a linear combination of B-spline basis functions with control points as coefficients. Equation (4) defines the B-spline completely. Piecewise linear interpolation of the control points gives the so-called *control polygon*.

2.3.1. Examples

Figures 3 and 4 give some examples of B-spline curves. B-spline curves inherit all of the continuity properties of their underlying bases. The use of open knots ensures that the first and last points are interpolated. In addition, in Fig. 4, the curve interpolates control point \mathbf{P}_6 where the knot multiplicity is two (see Property 6 of B-spline basis functions).

[Figure 3 about here.]

[Figure 4 about here.]

2.4. *h-, p- and k-refinement*

The B-spline basis can be enriched by three types of refinement which are termed *h-*, *p-* and *k-* refinement. In computer aided geometric design notation, these are referred to as knot insertion, degree elevation and degree and continuity elevation respectively. *h-* and *p-* refinement have a direct analogue in standard FEM while *k-* refinement has no equivalence. The present section disusses each of these refinement procedures in an analysis context.

2.4.1. *Knot insertion*

Knot insertion is found to preserve the geometry of B-spline curves and surfaces but has a direct influence on the continuity of the approximation where knots are repeated. Let us consider a knot vector defined by $\Xi = \{\xi_1, \xi_2, \dots, \xi_{n+p+1}\}$ with the corresponding set of control points denoted by \mathbf{B}_i . A new extended knot vector given by $\bar{\Xi} = \{\bar{\xi}_1 = \xi_1, \bar{\xi}_2, \dots, \bar{\xi}_{n+m+p+1} = \xi_{n+p+1}\}$ is formed where m knots are added. The $n + m$ new control points $\bar{\mathbf{B}}_i$ are formed from the original control points by

$$\bar{\mathbf{B}}_i = \alpha_i \mathbf{B}_i + (1 - \alpha_i) \mathbf{B}_{i-1}, \quad (5)$$

where

$$\alpha_i = \begin{cases} 1 & 1 \leq i \leq k - p, \\ \frac{\bar{\xi} - \xi_i}{\xi_{i+p} - \xi_i} & k - p + 1 \leq i \leq k, \\ 0 & k + 1 \leq i \leq n + p + 2. \end{cases} \quad (6)$$

Example Consider a quadratic B-spline curve with knot vector $\Xi = \{0, 0, 0, 0.5, 1, 1, 1\}$ and control points as shown in Fig. 5 (left). On the right of the same figure, two new knots $\xi = 0.25$ and $\xi = 0.75$ have been added. Consequently, two new control points have been formed. Although the curve is not changed geometrically and parametrically, the basis functions are now richer and may be more suitable for the purpose of analysis.

[Figure 5 about here.]

[Figure 6 about here.]

Let us now consider a quadratic B-spline defined with $\Xi = \{0, 0, 0, 1, 1, 1\}$. The three basis functions for this curve are illustrated in Fig. (6a). We now suppose that a discontinuity is required at $\xi = 0.5$. This can be achieved by inserting

a new knot $\bar{\xi} = 0.5$ three ($= p + 1$) times. The new knot vector is then given by $\Xi' = \{0, 0, 0, 0.5, 0.5, 0.5, 1, 1, 1\}$ and the new basis functions are shown in Fig. (6b). To demonstrate the resulting properties on a B-spline, let us build a B-spline curve with the control net defined by \mathbf{B} given in Eq. (7) with the new control net \mathbf{B}' created through knot insertion also detailed

$$\mathbf{B} = \begin{bmatrix} 0.0 & 0.0 \\ 0.5 & 0.5 \\ 1.0 & 0.0 \end{bmatrix}, \quad \mathbf{B}' = \begin{bmatrix} 0.00 & 0.00 \\ 0.25 & 0.25 \\ 0.50 & 0.25 \\ 0.50 & 0.25 \\ 0.75 & 0.25 \\ 1.00 & 0.00 \end{bmatrix}. \quad (7)$$

where it should be noted that $\mathbf{B}'_3 = \mathbf{B}'_4$. The B-spline curve corresponding to the original and refined basis is found to be identical and is illustrated in Fig. (6c). Imagine now that point \mathbf{B}'_4 is deviated slightly vertically with the resulting B-spline curve exhibiting a strong discontinuity at $x = 0.5$ shown in Fig. (6d). This technique of inserting knot values $p + 1$ times has been used in [40] to model the decohesion of material interfaces. The application of this method in two/three dimensions also resembles the usage of zero-thickness interface elements by doubling nodes in the FE framework.

2.4.2. *p-refinement*

p-refinement (order elevation) raises the polynomial order of the basis functions. During this process, the multiplicity of each knot is increased by one but no new knots are added. As with *h*-refinement, the geometry and the parametrization are not changed. We refer to [1] for the mathematical details but as an example of *p*-refinement, let us consider a quadratic B-spline curve shown in Fig. (7) (left). We raise the order of the basis from quadratic to cubic with the new basis functions shown in Fig. (7) (right).

[Figure 7 about here.]

2.4.3. *k-refinement*

k-refinement refers to the process in which order elevation is followed by knot insertion. This process results in a higher order and higher continuity basis than the process of knot insertion followed by order elevation. This non-commutative nature of refinement was first realised in [3]. Figure 8 illustrates the difference between *p*-refinement and *k*-refinement. We refer to the files `pRefinementExample1.m` and `kRefinementExample1.m` for the source code

used to generate these plots (this example was given in [3]). We start with the coarsest mesh (in this example one linear element). According to the p -refinement, the mesh is first refined by knot insertion to obtain three linear elements with C^0 continuity across the element boundaries (left figure on the second row of Fig. (8)). Order elevation is then performed on this mesh to obtain a mesh of three quadratic elements with C^0 continuity across the element boundaries (left figure on third row of Fig. (8)). The process is reversed in the k -refinement—order elevation is first performed to raise the basis functions to the desired order (right figure of second row of Fig. (8)) and then knot insertion is carried out (right figure of third row of Fig. (8)). Note that C^1 basis functions are obtained with k -refinement. For $p = 3$, we do not show the intermediate results of the order elevation step. As can be seen, k -refinement produces a few high order basis functions compared to p -refinement which results in a large number of C^0 functions.

[Figure 8 about here.]

2.5. B-spline surfaces

Given two knot vectors (one for each parametric direction) $\Xi = \{\xi_1, \xi_2, \dots, \xi_{n+p+1}\}$ and $\mathcal{H} = \{\eta_1, \eta_2, \dots, \eta_{m+q+1}\}$ and a control net $\mathbf{B}_{i,j} \in \mathbb{R}^d$, a tensor-product B-spline surface is defined as

$$\mathbf{S}(\xi, \eta) = \sum_{i=1}^n \sum_{j=1}^m N_{i,p}(\xi) M_{j,q}(\eta) \mathbf{B}_{i,j}, \quad (8)$$

where $N_{i,p}(\xi)$ and $M_{j,q}(\eta)$ are the univariate B-spline basis functions of order p and q corresponding to knot vectors Ξ and \mathcal{H} , respectively. The above can be rewritten in a more compact form as follows

$$\mathbf{S}(\xi, \eta) = \sum_{i=1}^n \sum_{j=1}^m N_{i,j}^{p,q}(\xi, \eta) \mathbf{B}_{i,j}, \quad (9)$$

where $N_{i,j}^{p,q}(\xi, \eta) = N_{i,p}(\xi) M_{j,q}(\eta)$ are the bivariate B-spline basis function. In Fig. (9) a bi-cubic B-Spline basis function is presented.

[Figure 9 about here.]

Let us consider the construction of an annular surface with inner radius equal to one and outer radius of two as shown in Fig.(10). The knot vectors are $\Xi = \{0, 0, 0, 0.5, 1, 1, 1\}$ (with a basis of order $p = 2$) and $\mathcal{H} = \{0, 0, 1, 1\}$ (with a linear basis), respectively.

[Figure 10 about here.]

[Figure 11 about here.]

The next example concerns the construction of an L-shaped surface as shown in Fig. (11). This example shows how to create a C^1 surface using quadratic ($p = q = 2$) B-splines for problems containing corner points. Although this geometry can be represented exactly using a C^0 surface, the use of a C^1 surface is beneficial from an analysis point of view. The control net and knot vectors for this example are given in Listing 1. The surface is actually generated using a NURBS code in which the weights are specified. As a final example, Fig. (12) presents a three dimensional B-spline surface. The corresponding data is given in Listing 2. The plot was then generated using function **plotMesh3**.

Listing 1: Matlab[®] data for the L-shaped domain shown in Fig. (11).

```
2;
2;
t = [0 0 0 0.5 1 1 1];
t = [0 0 0 1 1 1];
hts = [1 1 1 1 1 1 1 1 1 1 1 1]';
rolPts = [ -1 1; -1 -1; -1 -1; 1 -1;
5 1; -0.7 0; 0 -0.7; 1 -0.65;
0 0; 0 0; 1 0];
```

[Figure 12 about here.]

Listing 2: Matlab[®] data for half cylinder geometry shown in Fig. (12)

```
t = [0 0 0 0.5 0.5 1 1 1];
t = [0 0 1 1];
rolPts = [0 0 0; 0 0 1; 1 0 1; 2 0 1; 2 0 0;
0; 0 2 1; 1 2 1; 2 2 1; 2 2 0];
2;
1;
sX = 5;
sY = 2;
hts = ones(1,10)';
```

2.5.1. Derivatives

The derivatives of bivariate B-spline basis functions with respect to the parametric coordinates are computed as:

$$\frac{\partial N_{i,j}(\xi, \eta)}{\partial \xi} = \frac{d}{d\xi} \left(N_i(\xi) \right) M_j(\eta), \quad \frac{\partial N_{i,j}(\xi, \eta)}{\partial \eta} = \frac{d}{d\eta} \left(M_j(\eta) \right) N_i(\xi), \quad (10)$$

where the derivatives of the univariate B-spline basis functions are given in Eq. (3). The preceding sections have presented the construction of B-spline curves and surfaces, but they are known to exhibit certain limitations. The next section is devoted to a discussion of NURBS which, due to their inherent flexibility, are used henceforth in the paper.

3. NURBS

B-Splines are convenient for free-form modelling, but they lack the ability to exactly represent some simple shapes such as circles and ellipsoids. This is why today, the *de facto* standard technology in CAD is a generalization of B-Splines referred to as NURBS (Non-Uniform Rational B-Splines). NURBS are rational functions of B-Splines and inherit all their favourable properties. They can be shown to be a superset of B-Splines and are favoured over their counterparts since they allow exact representations of conic sections such as spheres and ellipsoids etc. In addition, there exist efficient algorithms for their evaluation and refinement (see e.g., [1]).

3.1. NURBS basis functions

NURBS basis functions are defined as

$$R_{i,p}(\xi) = \frac{N_{i,p}(\xi)w_i}{W(\xi)} = \frac{N_{i,p}(\xi)w_i}{\sum_{j=1}^n N_{j,p}(\xi)w_j}, \quad (11)$$

where $N_{i,p}(\xi)$ denotes the i th B-spline basis function of order p and w_i are a set of n positive weights. Selecting appropriate values for the w_i permits the description of many different types of curves including polynomials and circular arcs. For the special case in which $w_i = c \forall i$, the NURBS basis reduces to the B-spline basis. Note that for simple geometries, the weights can be defined analytically see e.g., [1]. For complex geometries, the weights are obtained from CAD packages such as Rhino [54] and can be defined by the user.

3.1.1. Derivatives of NURBS basis functions

The first derivative of a NURBS basis function $R_{i,p}(\xi)$ is computed using the quotient rule. That is,

$$\frac{d}{d\xi} R_{i,p}(\xi) = w_i \frac{N'_{i,p}(\xi)W(\xi) - N_{i,p}(\xi)W'(\xi)}{W(\xi)^2}, \quad (12)$$

where $N'_{i,p}(\xi) = \frac{d}{d\xi}N_{i,p}(\xi)$ and

$$W'(\xi) = \sum_{i=1}^n N'_{i,p}(\xi)w_i. \quad (13)$$

The Matlab[®] code to compute a NURBS basis function $R_{i,p}(\xi)$ at a parametric coordinate ξ is shown in Listing 3. The code also computes the first derivatives of the basis functions at ξ since these are required for calculating element stiffness matrices for FE analysis. Because computing such basis functions is expensive and has to be done repeatedly in a NURBS-based numerical method, the code is in effect implemented in a C file and interfaced with Matlab[®] using a MEX file⁵.

Listing 3: Matlab[®] code to compute a specific NURBS function and derivatives. We refer to **NURBSbasis.c** for the source code.

```

compute basis function N_i and derivative w.r.t XI at xi
th order p. The computation is implemented in
C file and interfaced with Matlab using a MEX file
N] = NURBSbasis (i, p, xi, knotVec, weights);

```

3.2. NURBS curves

In a similar fashion to B-spline curves, the NURBS curve is defined as

$$\mathbf{C}(\xi) = \sum_{i=1}^n R_{i,p}(\xi)\mathbf{B}_i, \quad (14)$$

where \mathbf{B}_i denotes the set of control points.

[Figure 13 about here.]

As a first example to illustrate NURBS curves, let us construct a quarter of a circle having a unit radius, as shown in Fig. (13), using only one NURBS curve. The Matlab[®] code to reproduce this figure is given in Listing 4. Function **NURBSinterpolation** is described later. The control points and the knot vector for a complete circle, shown in Fig. (14), are given in Listing 5.

Listing 4: Matlab[®] code to build NURBS curve as shown in Fig. (13).

⁵Interested readers can refer to <http://www.mathworks.com/support/tech-notes/1600/1605.html>.

```

s = [0 0 0 1 1 1];
= [0 0; 0 1; 1 1];
2;
= [1 1 1]; % b-spline weights
= [1 1/sqrt(2) 1]; % NURBS weights
s = 60;
linspace(0,1,noPts);
= zeros(2,noPts);
= zeros(2,noPts);
i=1:noPts
1,i)=NURBSinterpolation(xi(i),p,knots,pts(:,1),wts1);
2,i)=NURBSinterpolation(xi(i),p,knots,pts(:,2),wts1);
1,i)=NURBSinterpolation(xi(i),p,knots,pts(:,1),wts2);
2,i)=NURBSinterpolation(xi(i),p,knots,pts(:,2),wts2);

ot commands

```

[Figure 14 about here.]

Listing 5: Matlab[®] code to build NURBS curve as shown in Fig. (14). See file **circle.m**.

```

s = [0 0 0 1 1 2 2 3 3 4 4 4];
rolPts = [1 0;1 1;0 1;-1 1;-1 0;-1 -1;0 -1;1 -1;1 0];
2;
hts = ones(1,9)';
hts(2) = 1/sqrt(2);
hts(4) = 1/sqrt(2);
hts(6) = 1/sqrt(2);
hts(8) = 1/sqrt(2);

```

Listing 6 can be used to compute a NURBS interpolation given a parametric coordinate thus allowing a point in a NURBS curve to be determined (Eq. (14)) or the displacement field at a certain point to be found. Due to the local

support of the basis functions, at a point $\bar{\xi}$, it is found that there are $p + 1$ non-zero basis functions. Therefore for efficiency, the NURBS interpolation can be implemented as

$$\mathbf{C}(\bar{\xi}) = \sum_i R_{i,p}(\bar{\xi})\mathbf{B}_i, \quad (15)$$

where the sum is taken over the $(p + 1)$ non-zero basis functions $R_{i,p}$ where $i \in [span - p + 1, span + 1, \dots]$ where $span$ denotes the knot span in which $\bar{\xi}$ falls. An example is given here by considering eight quadratic B-spline basis functions with $\Xi = \{0, 0, 0, 1, 2, 3, 4, 4, 5, 5, 5\}$ as shown in Fig. (2) and $\bar{\xi} = 0.5$. The knot span of $\bar{\xi}$ is found to be two. Hence, the three non-zero basis functions at this point are R_1 , R_2 and R_3 . Equation 15 in this case reads $\mathbf{C}(\bar{\xi}) = R_1(\bar{\xi})\mathbf{B}_1 + R_2(\bar{\xi})\mathbf{B}_2 + R_3(\bar{\xi})\mathbf{B}_3$.

Listing 6: Matlab[®] code to interpolate a NURBS curve at a parametric coordinate.

```

: parametric coordinate
: order of basis
ot : knot vector
ints : control point coords or displacement coefficients
ights : NURBS weights
er interpDer] = NURBSinterpolation(xi, p, knot, points, weights);

```

The effect of a decreasing weight on a NURBS curve is demonstrated in Fig. (15). As can be seen, as the weight w_i decreases, the curve is pulled towards point \mathbf{B}_i . Likewise, as a weight is increased, the curved is pulled towards the associated control point.

[Figure 15 about here.]

3.3. NURBS surfaces

Given two knot vectors (one for each direction) $\Xi = \{\xi_1, \xi_2, \dots, \xi_{n+p+1}\}$ and $\mathcal{H} = \{\eta_1, \eta_2, \dots, \eta_{m+q+1}\}$ and a control net $\mathbf{B}_{i,j} \in \mathbb{R}^d$, a tensor-product NURBS surface is defined as

$$\mathbf{S}(\xi, \eta) = \sum_{i=1}^n \sum_{j=1}^m R_{i,j}^{p,q}(\xi, \eta)\mathbf{B}_{i,j}, \quad (16)$$

where the bivariate basis functions $R_{i,j}^{p,q}$ are given by

$$R_{i,j}^{p,q}(\xi, \eta) = \frac{N_i(\xi)M_j(\eta)w_{i,j}}{\sum_{i=1}^n \sum_{j=1}^m N_i(\xi)M_j(\eta)w_{i,j}}. \quad (17)$$

In order to compute a point on a NURBS surface, it is more convenient to work with homogeneous coordinates in a four-dimensional space. The non-rational B-spline surface in a four-dimensional space is given by

$$\mathbf{S}^w(\xi, \eta) = \sum_{i=1}^n \sum_{j=1}^m N_{i,p}(\xi) M_{j,q}(\eta) \mathbf{B}_{i,j}^w, \quad (18)$$

where $\mathbf{B}_{i,j}^w = (w_{i,j}x_{i,j}, w_{i,j}y_{i,j}, w_{i,j}z_{i,j}, w_{i,j})$. Finally the NURBS surface $\mathbf{S}(\xi, \eta)$ is obtained from $\mathbf{S}^w(\xi, \eta)$ by a projection operator as follows

$$S_1(\xi, \eta) = \frac{S_1^w(\xi, \eta)}{S_4^w(\xi, \eta)}, \quad S_2(\xi, \eta) = \frac{S_2^w(\xi, \eta)}{S_4^w(\xi, \eta)}, \quad S_3(\xi, \eta) = \frac{S_3^w(\xi, \eta)}{S_4^w(\xi, \eta)}. \quad (19)$$

[Figure 16 about here.]

Example Let us construct a plate with a circular hole using only two quadratic elements as shown in Fig. 16. The control points and knot vectors are given in Listing 7. The element edges in the mesh are the NURBS curves of the corresponding knot lines. An example of a knot line is $\xi = 0$ and $\eta = \{0, 0.1, \dots, 1\}$. For a given point (ξ, η) on a knot line, Eq. (18) is used to compute the point on the element edge (see lines 32-35 of Listing 8). This is achieved using function **SurfacePoint**. Line 34 and 35 implement the projection given in Eq. (19). Listing 8 which is an adaptation of the ISOGAT program [50], gives Matlab[®] code to plot the mesh as shown in Fig. (16).

Listing 7: Control points, weights and knot vectors to construct geometry of a plate with a circular hole as shown in Fig. (16).

```

2;
2;
rolPts = zeros(4,3,2);
rolPts(1,1,:) = [-1 0];
rolPts(1,2,:) = [-2.5 0];
rolPts(1,3,:) = [-4 0];
rolPts(2,1,:) = [-1 sqrt(2)-1];
rolPts(2,2,:) = [-2.5 0.75];
rolPts(2,3,:) = [-4 4];
rolPts(3,1,:) = [1-sqrt(2) 1];
rolPts(3,2,:) = [-0.75 2.5];
rolPts(3,3,:) = [-4 4];
rolPts(4,1,:) = [0 1];

```

```

rolPts(4,2,:) = [0 2.5];
rolPts(4,3,:) = [0 4];
t = [0 0 0 0.5 1 1 1];
t = [0 0 0 1 1 1];
sX = size(controlPts,1);
sY = size(controlPts,2);
rolPtsX = reshape(controlPts(:,:,1),noPtsX,noPtsY);
rolPtsY = reshape(controlPts(:,:,2),noPtsX,noPtsY);
rolPts = reshape(controlPts,noPtsX*noPtsY,2);
hts = ones(1,noPtsX*noPtsY)';
hts(2) = weights(3)=0.5*(1+1/sqrt(2));

```

Listing 8: Matlab[®] code to generate Fig. (16).

```

1  scretize the xi and eta directions
2  s = 20;
3  c = linspace(0,max(uKnot),noPts);
4  ec = linspace(0,max(vKnot),noPts);
5  scard zero measure knot spans
6  tVec = unique(uKnot);
7  tVec = unique(vKnot);
8  mber of distinct knot values
9  otsU = length(uKnotVec);
10 otsV = length(vKnotVec);
11 zeros(noKnotsU,noPts);
12 zeros(noKnotsU,noPts);
13 zeros(noKnotsV,noPts);
14 zeros(noKnotsV,noPts);
15 RBS curves of knot lines corresponding to xi direction
16 coord = nurb2proj(noPtsX*noPtsY, controlPts, weights);
17 = size(projcoord,2);

```



```

18 uk=1:noKnotsU
19   uKnotVec(uk);
20 i=1:noPts
21   = etaVec(i);
22   = SurfacePoint(noPtsX-1,p,uKnot,noPtsY-1,q,...
23   t, projcoord,dim,xi,eta);
24   k,i) = tem(1)/tem(3);
25   k,i) = tem(2)/tem(3);
26
27
28 RBS curves of knot lines corresponding to eta direction
29 vk=1:noKnotsV
30   = vKnotVec(vk);
31 i=1:noPts
32   xiVec(i);
33   = SurfacePoint(noPtsX-1,p,uKnot,noPtsY-1,q,...
34   t, projcoord,dim,xi,eta);
35   k,i) = tem(1)/tem(3);
36   k,i) = tem(2)/tem(3);
37
38
39   on
40   (x1',y1','r-','LineWidth',1.2);
41   (x2',y2','r-','LineWidth',1.2);
42   (controlPtsX, controlPtsY,'ro-');
43   (controlPtsX', controlPtsY','ro-');

```

3.3.1. NURBS derivatives

The first derivatives of the bivariate NURBS basis are given by

$$\frac{\partial R_{i,j}^{p,q}}{\partial \xi} = w_{i,j} \frac{N'_{i,p} M_{j,q} W - N_{i,p} M_{j,q} W'_\xi}{W^2} \quad (20a)$$

$$\frac{\partial R_{i,j}^{p,q}}{\partial \eta} = w_{i,j} \frac{N_{i,p} M'_{j,q} W - N_{i,p} M_{j,q} W'_\eta}{W^2}, \quad (20b)$$

where

$$W'_\xi = \sum_{i=1}^n \sum_{j=1}^m N'_{i,p} M_{j,q} w_{i,j} \quad (21a)$$

$$W'_\eta = \sum_{i=1}^n \sum_{j=1}^m N_{i,p} M'_{j,q} w_{i,j} \quad (21b)$$

$$W = \sum_{i=1}^n \sum_{j=1}^m N_{i,p} M_{j,q} w_{i,j}. \quad (21c)$$

3.3.2. NURBS surface subdivision

This section presents a simple global h -refinement algorithm applied to a NURBS surface. The idea here is to transform the original knot vector into one where additional knots are inserted between the unique values of the existing points. For example $\Xi = [0, 0, 0.5, 1, 1]$ becomes $\Xi = [0, 0, 0.25, 0.5, 0.75, 1, 1]$ after refinement. Let us consider the refinement of a unit square with $\Xi = [0, 0, 1, 1]$, $p = 1$, $\mathcal{H} = [0, 0, 1, 1]$, $q =$ and four control points $\mathbf{B}_i, i = 1, \dots, 4$ as shown in Fig. (17). In the first step, one knot is inserted into Ξ to give $\Xi_1 = [0, 0, 0.5, 1, 1]$ and \mathcal{H} is kept fixed. The refinement is applied to $\mathbf{B}_1, \mathbf{B}_2$ (corresponding to $\eta = 0$) to obtain \mathbf{B}_5 (using the knot insertion algorithm given in Section 2.4) and then also to $\mathbf{B}_3, \mathbf{B}_4$ (corresponding to $\eta = 1$) to give \mathbf{B}_6 . The process is then repeated for the η direction with $\mathcal{H}_1 = [0, 0, 0.5, 1, 1]$ in exactly the same manner.

[Figure 17 about here.]

This global h -refinement algorithm is implemented in the script **hRefinement2d.m** which is based on the code given in [50]. An example of mesh refinement using knot insertion is given in Fig. (18). The control points and weights for the coarsest mesh (upper left figure) are given in Listing 7. Listing 9 outlines the Matlab[®] code used to generate Fig. (18).

[Figure 18 about here.]

Listing 9: Matlab[®] code used to generates meshes as shown in Fig. (18).

```

initial control points, weights, knot vectors, p and q defined for the
arsest mesh
rst refinement
neCount=1
inement2d
Mesh (controlPts,weights,uKnot,vKnot,p,q,50,'r-','try.eps');
cond refinement
inement2d
Mesh (controlPts,weights,uKnot,vKnot,p,q,50,'r-','try.eps');
ird refinement
inement2d
Mesh (controlPts,weights,uKnot,vKnot,p,q,50,'r-','try.eps');

```

3.4. NURBS solids

NURBS solids are simply an extension of NURBS surfaces to a trivariate representation and are defined as

$$\mathbf{S}(\xi, \eta, \zeta) = \sum_{i=1}^n \sum_{j=1}^m \sum_{k=1}^l R_{i,j,k}^{p,q,r}(\xi, \eta, \zeta) \mathbf{B}_{i,k,j}, \quad (22)$$

where $R_{i,j,k}^{p,q,r}$ are given by

$$R_{i,j,k}^{p,q,r}(\xi, \eta, \zeta) = \frac{N_i(\xi)M_j(\eta)P_k(\zeta)w_{i,j,k}}{\sum_{\hat{i}=1}^n \sum_{\hat{j}=1}^m \sum_{\hat{k}=1}^l N_{\hat{i}}(\xi)M_{\hat{j}}(\eta)P_{\hat{k}}(\zeta)w_{\hat{i},\hat{j},\hat{k}}}. \quad (23)$$

The first derivatives of these trivariate NURBS basis can be computed using the chain rule in a similar fashion as Eq. (20).

4. Finite element analysis with NURBS

4.1. Isoparametric discretisation

The isoparametric concept refers to the use of the same basis functions for both the geometry and unknown field discretisation. Both FEM and IGA formulations most commonly utilise the isoparametric concept. However, they differ from each other by the type of basis functions used. That is,

- Finite elements: the basis which is chosen to approximate the unknown field, is also used to approximate the known geometry. This most commonly takes the form of polynomial functions and the geometry is in most cases only approximated.
- Isogeometric analysis: the basis is chosen to exactly capture the geometry and this is also used to approximate the unknown field. Refinement may be required for the unknown fields, but the exact geometry is used at all stages of analysis.

From an FEM analysis standpoint, a finite element mesh is usually generated by so-called mesh generation programs or ‘meshers’ that give an approximation of the geometry of the object under consideration. A mesh usually consists of nodal coordinates and element connectivity data. In contrast, the input for an IGA computation is a CAD model defined in terms of NURBS curves which can be used directly for analysis. The input data would most commonly take the form of knot vectors, control points and degree orders, although more efficient algorithms have been recently developed to further simplify the use of CAD data for analysis [55, 33]. The physical domain is denoted by Ω and the parametric domain by $\hat{\Omega}$, where we refer to Fig. (19) for the illustration of these terms. In two dimensions, the parametric domain is a square and in three dimensions it is a cube. The mapping from the parametric domain to the physical domain is then given by

$$\mathbf{x} = \sum_{I=1}^n \Phi_I(\boldsymbol{\xi}) \mathbf{B}_I \quad (24)$$

where the shape function $\Phi_I(\boldsymbol{\xi})$ refers to either the univariate NURBS basis function if Ω is a curve or the bivariate NURBS basis function in case Ω is a surface. The number of control points is denoted by n . In the above, $\boldsymbol{\xi}$ is the parametric coordinate i.e., ξ in one dimension, (ξ, η) in two dimensions and (ξ, η, ζ) in three dimensions and \mathbf{B}_I denotes the control point number I . In an isoparametric formulation, the displacement field is approximated by the same shape functions. That is,

$$\mathbf{u}(\mathbf{x}) = \sum_{I=1}^n \Phi_I(\boldsymbol{\xi}) \mathbf{u}_I, \quad (25)$$

where \mathbf{u}_I denotes the value of the displacement field at the control point \mathbf{B}_I . It is therefore referred to as a *control variable* or more generally a degree of freedom (dof). It should be emphasized that since control points do not generally locate inside the domain of interest, see for example Fig. (10), \mathbf{u}_I thus does not usually represent a physical nodal displacement as in conventional FEM. For control points inside the physical domain, \mathbf{u}_I also does not represent a physical nodal displacement due to the non-interpolatory nature of NURBS. This is similar to the case of meshless methods built on non-interpolatory shape functions such as the moving least squares (MLS).

4.2. Spatial derivatives of shape functions

Before computing the spatial derivatives of the shape functions $N_{I,x}$ and $N_{I,y}$, it is necessary to compute the Jacobian matrix of the geometry mapping defined in Eq. (24)

$$\mathbf{J}_\xi = \begin{bmatrix} x_{,\xi} & x_{,\eta} \\ y_{,\xi} & y_{,\eta} \end{bmatrix}, \quad (26)$$

with the components calculated as (using Eq. (24))

$$\frac{\partial x_i}{\partial \xi_j} = \frac{\partial \Phi_I}{\partial \xi_j} B_{iI}, \quad (27)$$

where B_{iI} represents the i coordinate of control point I . The determinant of \mathbf{J}_ξ is denoted by $|\mathbf{J}_\xi|$. Derivatives of basis functions with respect to the physical domain coordinates are given by

$$\begin{bmatrix} \Phi_{I,x} & \Phi_{I,y} \end{bmatrix} = \begin{bmatrix} \Phi_{I,\xi} & \Phi_{I,\eta} \end{bmatrix} \begin{bmatrix} \xi_{,x} & \xi_{,y} \\ \eta_{,x} & \eta_{,y} \end{bmatrix} = \begin{bmatrix} \Phi_{I,\xi} & \Phi_{I,\eta} \end{bmatrix} \mathbf{J}_\xi^{-1}, \quad (28)$$

where $\Phi_{I,\xi}, \Phi_{I,\eta}$ are computed using Eq. (10) in the case of B-spline surfaces or Eq. (20) for NURBS curves.

4.3. Numerical integration

Integrals over the entire geometry (physical domain Ω) are split into element integrals with a domain denoted by Ω_e . These integrals are pulled back to the parametric element $\hat{\Omega}_e$ via the geometry mapping, Eq. (24). Finally, integrals over the parametric element are pulled back to the parent domain \square where existing integration rules are usually defined. Refer to Fig. (19) for an illustration. Mathematically, we write for a function of two variables x and y

$$\begin{aligned} \int_{\Omega} f(x, y) d\Omega &= \sum_{e=1}^n \int_{\Omega_e} f(x, y) d\Omega_e \\ &= \sum_{e=1}^n \int_{\hat{\Omega}_e} f(x(\xi), y(\eta)) |\mathbf{J}_\xi| d\hat{\Omega}_e \\ &= \sum_{e=1}^n \int_{\square} f(\bar{\xi}, \bar{\eta}) |\mathbf{J}_\xi| |\mathbf{J}_{\bar{\xi}}| d\square. \end{aligned} \quad (29)$$

The final integral can be performed using standard Gauss-Legendre quadrature. Specially, a $(p+1) \times (q+1)$ Gaussian quadrature is adopted for two dimensional elements with p and q denoting the orders of the NURBS basis in the ξ and η directions. It should be emphasized that Gaussian quadrature is not optimal for IGA. One reason which contributes to this is that the higher order NURBS basis functions employed in IGA possess a certain degree of smoothness across

element boundaries. This results in a reduction in the number of basis functions and unknowns when compared with standard FEs for the same mesh. Hence evaluation of a NURBS basis requires fewer quadrature points [56]. In the cited work, an optimal quadrature rule—the half-point rule—for IGA has been presented. In our paper, only a standard Gauss-Legendre quadrature implementation is used.

[Figure 19 about here.]

The transformation from the parent domain \square to a parametric domain $[\xi_i, \xi_{i+1}] \times [\eta_j, \eta_{j+1}]$ is given by

$$\xi = \frac{1}{2}[(\xi_{i+1} - \xi_i)\bar{\xi} + (\xi_{i+1} + \xi_i)] \quad (30)$$

$$\eta = \frac{1}{2}[(\eta_{j+1} - \eta_j)\bar{\eta} + (\eta_{j+1} + \eta_j)]. \quad (31)$$

Therefore, the Jacobian of this transformation reads

$$|J_{\bar{\xi}}| = \frac{1}{4}(\xi_{i+1} - \xi_i)(\eta_{j+1} - \eta_j). \quad (32)$$

4.4. Assembly for one dimensional problems

To illustrate the use of the isogeometric concept in a finite element context, an example is best suited for explanation. Let us consider the following one dimensional Poisson equation

$$u_{,xx}(x) + b(x) = 0 \quad x \in [0, 1]; \quad u(0) = 0, \quad u(1) = 0, \quad (33)$$

with $b(x) = x$. It should be emphasized that the boundary conditions given above are homogeneous Dirichlet boundary conditions which can be imposed directly as in FEM by setting the corresponding control variables as zeros. This is due to the use of an open knot vector which ensures that the first and last points of the curve are interpolatory (see Section 2). More details on imposition of boundary conditions are provided in Section 4.8. The exact solution of this problem is

$$u(x) = -\frac{1}{6}x^3 + \frac{1}{6}x. \quad (34)$$

The weak form associated with Eq. (33) is given by

$$\text{Find } u \in \mathcal{U} \mid \forall v \in \mathcal{U}^o, \quad \int_0^1 \frac{du}{dx} \frac{dv}{dx} dx = \int_0^1 b(x)v(x)dx, \quad (35)$$

where \mathcal{U} and \mathcal{U}^o are the usual trial and test spaces. The discrete form of this equation reads

$$\left(\int_0^1 N_{I,x}(x)N_{J,x}(x)dx \right) u_J = \int_0^1 b(x)N_I(x)dx, \quad (36)$$

using Eq. (25). In matrix notation, we have

$$K_{IJ}u_J = f_I, \quad (37)$$

where the stiffness matrix and the force vector are defined as

$$K_{IJ} = \int_{\Omega} N_{I,x}(x)N_{J,x}(x)d\Omega, \quad f_I = \int_{\Omega} b(x)N_I(x)d\Omega. \quad (38)$$

In order to build the global stiffness matrix, first the elementary stiffness matrices are computed. They are then assembled into the global stiffness matrix \mathbf{K} . In the same manner, one obtains the global force vector \mathbf{f} . The solution is then given by $\mathbf{u} = \mathbf{K}^{-1}\mathbf{f}$.

[Figure 20 about here.]

To illustrate the assembly of the elementary stiffness into the global stiffness matrix, let us consider the example given in Fig. (20). Recall that for element $e = [\xi_i, \xi_{i+1}]$, there are $p + 1$ non-zero basis functions N_{α} with $i - p \leq \alpha \leq i$. This can be seen from Fig. (20). For this problem, the data is therefore as follows

element	range	non-zero basis	dofs	control points	
1	$[\xi_3, \xi_4]$	N_1, N_2, N_3	u_1, u_2, u_3	$\mathbf{B}_1, \mathbf{B}_2, \mathbf{B}_3$, (39)
2	$[\xi_4, \xi_5]$	N_2, N_3, N_4	u_2, u_3, u_4	$\mathbf{B}_2, \mathbf{B}_3, \mathbf{B}_4$	

where the dofs data is used to assemble the global stiffness matrix. One can consider this mesh as composed of two elements of which each has three nodes (control points). In this paper we use nodes and control points interchangeably. Box 1 outlines the steps to compute K_{IJ} for element 1 of the problem given in Fig. (20). The Matlab[®] implementation of Eq. (36) is shown in Listing 10 where we have used 3 Gauss points for the numerical integration. This implementation follows the procedure given in Box 1. The function **generateIGA1DMesh** reads the CAD data (knots and control points) and then creates the element connectivity matrix and the element geometry i.e., $[\xi_i, \xi_{i+1}]$. Its interface is given in Listing 11. Note that for this one dimensional problem (Eq. (33)), the y coordinates of control points are simply zero. The good agreement of the numerical results for linear, quadratic and cubic B-spline elements compared to the exact solution as shown in Fig. (21) verifies the implementation. The solution gives us the displacements at the control points. A NURBS interpolation is then used to compute the displacement at any point of interest as shown in Listing 12.

Listing 10: Isogeometric analysis Matlab[®] code for the 1D PDE given in Eq. (33) (see file **iga1D.m**).

PUT

Box 1 Procedure for evaluation of Eq. (38) for element $[\xi_i, \xi_{i+1}]$.

1. $\mathbf{x} = [\mathbf{B}_1; \mathbf{B}_2; \mathbf{B}_3]$
2. $sctr = [1, 2, 3]$
3. Set $\mathbf{K}_e = 0$
4. Loop over Gauss points (GPs) $(\bar{\xi}, w)^*$
 - (a) Compute parametric coordinate $\xi = 0.5[(\xi_{i+1} - \xi_i)\bar{\xi} + \xi_{i+1} + \xi_i]$
 - (b) Compute derivatives $N_{I,\xi}$ ($I = 1, 2, 3$) at point ξ
 - (c) Define vector $\mathbf{N}_\xi = [N_{1,\xi} \ N_{2,\xi} \ N_{3,\xi}]$
 - (d) Compute the first Jacobian $J_\xi = \|\mathbf{N}_\xi \mathbf{x}\|$
 - (e) Compute the second Jacobian $J_{\bar{\xi}} = 0.5(\xi_{i+1} - \xi_i)$
 - (f) Compute shape function derivatives $\mathbf{N}_x = J_\xi^{-1} \mathbf{N}_\xi^T$
 - (g) $\mathbf{K}_e = \mathbf{K}_e + J_\xi J_{\bar{\xi}} w \mathbf{N}_x \mathbf{N}_x^T$
5. End loop over GPs
6. Assemble \mathbf{K}_e to the global matrix $\mathbf{K}(sctr, sctr) = \mathbf{K}(sctr, sctr) + \mathbf{K}_e$

* w denotes the weight of a Gauss point.

```

Vec = [0 0 0 1 1 1];
rolPts = [0 0; 0.5 0; 1 0];
2;
hts = ones(1,size(controlPts,1));
s = 3; % # of GPs per element
nement = 2; % # of h-refinement
%%%%%%%%%%%%%%%%%%%%%%%%%%%%%%%%%%%%%%%%%%%%%%%%%%%%%%%%%%%%%%%%%%%%%%%%
PRE-PROCESSING
rateIGA1DMesh;
rPts = size(controlPts,1); % no of control points
ems = size(elConn,1); % no of elements
itialization
zeros(noCtrPts,noCtrPts); % global stiffness matrix
zeros(noCtrPts,1); % displacement vector
zeros(noCtrPts,1); % external force vector
%%%%%%%%%%%%%%%%%%%%%%%%%%%%%%%%%%%%%%%%%%%%%%%%%%%%%%%%%%%%%%%%%%%%%%%%
PROCESSING
uss quadrature rule
]=quadrature(noGPs, 'GAUSS', 1); % 1D quadrature
stem of equations assembly
iffness matrix and external force vector
op over elements (knot spans)
e=1:noElems
= elRange(e,:); % [xi_i,xi_i+1]
= elConn(e,:);
s = length(conn);
op over Gauss points
gp=1:size(W,1)
Q(gp,:);
W(gp);

```

```

    0.5 * ( ( xiE(2) - xiE(1) ) * pt
E(2) + xiE(1));% in param space
    0.5 * ( xiE(2) - xiE(1) );
[];
i = [];
compute deriv. of basis functions wrt param. coord
in=1:noFns
dNi] = NURBSbasis (conn(in),p,Xi,...,
Vec,controlPts(:,3)');
[N Ni];
i = [dNdx_i dNi];

compute the jacobian of physical and parameter
main mapping then the derivative w.r.t physical coordinates
b1 = dNdx_i*controlPts(conn,1:2);
    norm (jacob1);
    = (1/J1)*dNdx_i;
compute elementary stiffness matrix and
semble into global stiffness matrix
nn,conn) = K(conn,conn) + dNdx_i'*dNdx_i*J1*J2*wt;
compute the external element force vector
d assemble into global force vector
N * controlPts(conn,1:2);
    X(1);
nn) = f(conn) + bx * N' * J1 * J2 * wt;

ply bound. conds. and solve system of equations
=mean(diag(K));
s = [1 noCtrPts];

```

```

ed = [0 0]';
f-K(:,udofs)*uFixed;
ofs) = bcwt*uFixed;
ofs,udofs) = bcwt*speye(length(udofs));
f;

```

Listing 11: Script generateIGA1DMesh.m.

```

rolPts = [controlPts weights'];
-----
----- h-refinement -----
-----
e idea here is to take the original knot vector
d add knots at points in between existing points
ueKnots=unique(knotVec);
-----
---Define element connectivities ---
-----
length(uniqueKnots)-1;% number of elements
nge = zeros(ne,2); % initialise matrices
nn = zeros(ne,p+1);
otIndices = zeros(ne,2);
termine element ranges and corresponding knot indices

```

[Figure 21 about here.]

Listing 12: NURBS interpolation to compute the displacement field at any desired point.

```

= 20; % number of sampling points where u is computed
linspace(0,1,noXi);
= zeros(noXi,1);
= zeros(noXi,1);

```

```

i=1:noXi
i,1) = NURBSinterpolation(xi(i), p, knotVec, U', controlPts(:,3)');
i,1) = NURBSinterpolation(xi(i), p, knotVec, ...
rolPts(:,1)', controlPts(:,3)');

```

4.5. Assembly process for two dimensional elastostatic analysis

Consider a domain Ω , bounded by Γ . The boundary is partitioned into two sets: Γ_u and Γ_t with displacements prescribed on Γ_u and tractions $\bar{\mathbf{t}}$ prescribed on Γ_t . The weak form of a linear elastostatics problem is to find \mathbf{u} in the trial space ⁶, such that for all test functions $\delta\mathbf{u}$ in the test space ⁷,

$$\int_{\Omega} \boldsymbol{\varepsilon}(\mathbf{u}) : \mathbf{D} : \boldsymbol{\varepsilon}(\delta\mathbf{u}) d\Omega = \int_{\Gamma_t} \bar{\mathbf{t}} \cdot \delta\mathbf{u} d\Gamma + \int_{\Omega} \mathbf{b} \cdot \delta\mathbf{u} d\Omega, \quad (40)$$

where the elasticity matrix is denoted by \mathbf{D} and \mathbf{b} refers to a body force. Using the Bubnov-Galerkin method where the same shape functions Φ_I are used for both \mathbf{u} and $\delta\mathbf{u}$, we can write

$$\mathbf{u}(\mathbf{x}) = \sum_I^n \Phi_I(\boldsymbol{\xi}) \mathbf{u}_I, \quad \delta\mathbf{u}(\mathbf{x}) = \sum_I^n \Phi_I(\boldsymbol{\xi}) \delta\mathbf{u}_I, \quad (41)$$

where $\delta\mathbf{u}_I$ denote the nodal displacement variations. Substitution of these approximations into Eq. (40) gives the discrete set of equations

$$\mathbf{K} \mathbf{u} = \mathbf{f}, \quad (42)$$

with

$$\mathbf{K}_{IJ} = \int_{\Omega} \mathbf{B}_I^T \mathbf{D} \mathbf{B}_J d\Omega, \quad \mathbf{f}_I = \int_{\Gamma_t} \Phi_I \bar{\mathbf{t}} d\Gamma + \int_{\Omega} \Phi_I \mathbf{b} d\Omega. \quad (43)$$

In two dimensions, the \mathbf{B} matrix (not to be confused with the control net) is given by

$$\mathbf{B}_I = \begin{bmatrix} \Phi_{I,x} & 0 \\ 0 & \Phi_{I,y} \\ \Phi_{I,y} & \Phi_{I,x} \end{bmatrix}, \quad (44)$$

where the shape function derivatives are computed according to Eq. (28). We now consider the two dimensional problem as shown in Fig. (22). In this case, the knot vectors are $\Xi = [0, 0, 1, 1]$ and $\mathcal{H} = [0, 0, 0, 0.5, 1, 1, 1]$, respectively. The

⁶contains C^0 functions

⁷contains C^0 functions but vanishes on Γ_u

orders of the basis functions are $p = 1$ and $q = 2$. Eight control points are defined: two points along the ξ direction and four points along the η direction.

[Figure 22 about here.]

The domain and non-zero basis functions for Element 1 are given by

direction	range	non zero basis	
ξ	$[\xi_2, \xi_3]$	N_1, N_2	(45)
η	$[\eta_3, \eta_4]$	M_1, M_2, M_3	

Hence there are six non-zero basis functions on element $e = 1$ which can be assembled into a vector \mathbf{R} as follows

$$\mathbf{R}_1 = [N_1M_1, N_2M_1, N_1M_2, N_2M_2, N_1M_3, N_2M_3]. \quad (46)$$

These six basis functions are associated with six global basis number indices given by

$$\text{element}(1, :) = [1, 2, 3, 4, 5, 6] \quad (47)$$

Similarly, for element 2, the shape function vector is given by

$$\mathbf{R}_2 = [N_1M_2, N_2M_2, N_1M_3, N_2M_3, N_1M_4, N_2M_4] \quad (48)$$

with the associated global indices

$$\text{element}(2, :) = [3, 4, 5, 6, 7, 8] \quad (49)$$

Control points are stored in a two dimensional matrix of dimensions $n \times 2$ (n denotes the number of control points in the mesh). The connectivity data is stored in a two dimensional matrix of dimensions $n_{el} \times (p + 1) * (q + 1)$ where n_{el} denotes the number of elements. For the example under consideration, these two matrices are given by

$$\text{controlPts} = \begin{bmatrix} \mathbf{B}_{11} \\ \mathbf{B}_{21} \\ \mathbf{B}_{12} \\ \mathbf{B}_{22} \\ \mathbf{B}_{13} \\ \mathbf{B}_{23} \\ \mathbf{B}_{14} \\ \mathbf{B}_{24} \end{bmatrix}, \quad \text{element} = \begin{bmatrix} 1 & 2 & 3 & 4 & 5 & 6 \\ 3 & 4 & 5 & 6 & 7 & 8 \end{bmatrix} \quad (50)$$

The knot ranges along the ξ and η directions are stored in the following matrices

$$\text{elRangeU} = \begin{bmatrix} 0 & 1 \end{bmatrix}, \quad \text{elRangeV} = \begin{bmatrix} 0 & 0.5 \\ 0.5 & 1 \end{bmatrix} \quad (51)$$

where the number of rows is equal to the number of elements (non-zero knot spans) in each direction. With this vector of basis functions \mathbf{R} , we can compute the derivatives of the basis functions. The derivatives of the basis functions with respect to x are stored in the following vector

$$\mathbf{R}_{,x} = \left[R_{1,x} \quad R_{2,x} \quad R_{3,x} \quad R_{4,x} \quad R_{5,x} \quad R_{6,x} \right]^T \quad (52)$$

Similarly, we have $\mathbf{R}_{,y}$ for the derivatives of the basis functions with respect to y . Having these basis function derivatives, we are now ready to define the \mathbf{B} matrix for any element e

$$\mathbf{B}_e = \begin{bmatrix} \mathbf{R}[1],x & \mathbf{R}[2],x & \cdots & \mathbf{R}[6],x & 0 & \cdots & 0 \\ 0 & 0 & \cdots & 0 & \mathbf{R}[1],y & \cdots & \mathbf{R}[6],y \\ \mathbf{R}[1],y & \mathbf{R}[2],y & \cdots & \mathbf{R}[6],y & \mathbf{R}[1],x & \cdots & \mathbf{R}[6],x \end{bmatrix} \quad (53)$$

where the control point displacement vector is stored in the following order $\mathbf{u} = [u_{1x}, u_{2x}, \dots, u_{nx}, u_{1y}, u_{2y}, \dots, u_{ny}]^T$. The element stiffness matrix is then given by

$$\mathbf{K}_e = \int_{\Omega_e} \mathbf{B}_e^T \mathbf{D} \mathbf{B}_e d\Omega_e \quad (54)$$

which is then assembled to the global stiffness matrix using the element connectivity matrix. For implementation convenience, Box 2 gives a procedure of an isogeometric analysis for 2D elasticity problems. Listing 13 gives the input for the problem given in Fig. (22). The initial mesh consists of one single element with six control points. This mesh is then refined using a global h -refinement process (refer to Section 3.3.2). Finally, the function `generateIGA2DMesh` computes the number of elements, the element connectivity matrix, the knot ranges etc.. The processing (assembly of stiffness matrix, boundary conditions enforcement and solution of the system) is given in Listing 14. Note that only the step of assembly was given here since all other steps are considered standard procedures. Our IGA implementation is based on the FE Matlab[®] code written by Chessa [57]. It should be emphasized that the IGA-FEM code shows many similarities to a standard FEM code. In order to compute the external force vector, it is convenient to define a boundary mesh as shown in Fig. (23). The Matlab[®] code to automatically generate this boundary mesh is given in Listing 15. The computation of the external force vector $\int_{\Gamma} \mathbf{R}^T \bar{\mathbf{t}} d\Gamma$ then follows the one dimensional assembly procedure given in Listing 10.

Box 2 Procedure for isogeometric analysis of 2D elasticity problems.

1. Loop over elements, $e = 1, \dots, nel$
 - (a) Determine NURBS coordinates $[i, i + 1] \times [j, j + 1]$
 - (b) Get connectivity array, $sctr = element(e, :)$
 - (c) Define $sctrB = sctr + n$ used for assembly *
 - (d) $\mathbf{K}_e = \mathbf{0}$
 - (e) Loop over Gauss points, $(\bar{\xi}, w)$
 - i. Compute ξ and η corresponding to $\bar{\xi}$ (Eq. 31)
 - ii. Compute $|\mathbf{J}_{\bar{\xi}}|$ (Eq. 32)
 - iii. Compute derivatives of shape functions $\mathbf{R}_{,\xi}$ and $\mathbf{R}_{,\eta}$
 - iv. Compute \mathbf{J}_{ξ} using $controlPts(sctr, :)$, $\mathbf{R}_{,\xi}$ and $\mathbf{R}_{,\eta}$ (Eq. 27)
 - v. Compute Jacobian inverse \mathbf{J}_{ξ}^{-1} and determinant $|\mathbf{J}_{\xi}|$
 - vi. Compute derivatives of shape functions $\mathbf{R}_{,\mathbf{x}} = [\mathbf{R}_{,\xi} \ \mathbf{R}_{,\eta}] \mathbf{J}_{\xi}^{-1}$ (Eq. 28)
 - vii. Use $\mathbf{R}_{,\mathbf{x}}$ to build the strain-displacement matrix \mathbf{B}
 - viii. Compute $\mathbf{K}_e = \mathbf{K}_e + w |\mathbf{J}_{\bar{\xi}}| |\mathbf{J}_{\xi}| \mathbf{B}^T \mathbf{D} \mathbf{B}$
 - (f) End loop over Gauss points
 - (g) Assemble \mathbf{K}_e : $\mathbf{K}(sctrB, sctrB) \leftarrow \mathbf{K}_e$
2. End loop over elements

* n denotes the number of control points.

Listing 13: Matlab[®] code for input and mesh generation.

```

t = [0 0 0 1 1 1];
t = [0 0 1 1];
rolPts=[-1 0;-1 1;0 1;
;-2 2; 0 2];
sX = 3;
sY = 2;
hts = ones(1,noPtsX*noPtsY)';
hts(2)=1/sqrt(2);
hts(5)=1/sqrt(2);
inement2d
rPts = noPtsX * noPtsY;
fs = noCtrPts * 2;
rateIGA2DMesh

```

Listing 14: Matlab[®] code for IGA of 2D elasticity problems, see file **iga2d.m**.

```

]=quadrature(4, 'GAUSS', 2); % 4x4 point quadrature
semble system of equations
e=1:noElems % Loop over elements (knot spans)
= index(e,1);
= index(e,2);
= elRangeU(idu,:); % [xi_i,xi_i+1]
= elRangeV(idv,:); % [eta_j,eta_j+1]
= element(e,:); % element scatter vector
B = [sctr sctr+noFnsU*noFnsV]; % B scatter vec.
length(sctr);
zeros(3,2*nn);
op over Gauss points
gp=1:size(W,1)
Q(gp,:);

```



```

W(gp);
compute coords in parameter space
parent2ParametricSpace(xiE,pt(1));
= parent2ParametricSpace(etaE,pt(2));
jacobianPaPaMapping(xiE,etaE);
private of R=Nxi*Neta w.r.t xi and eta
xi dRdeta] = NURBS2Dders([Xi;Eta],p,q,...
t,vKnot,weights');
jacobian matrix
= controlPts(sctr,:);
b = pts'*[dRdxi' dRdeta'];
det(jacob);
acob = inv(jacob);
= [dRdxi' dRdeta'] * invJacob;
matrix
1:nn) = dRdx(:,1)';
nn+1:2*nn) = dRdx(:,2)';
1:nn) = dRdx(:,2)';
nn+1:2*nn) = dRdx(:,1)';
compute elementary stiffness matrix and
semble it into the global stiffness matrix
trB,sctrB) = K(sctrB,sctrB) + B'*C*B*J1*J2*wt;

```

[Figure 23 about here.]

Listing 15: Matlab[®] code for generating a boundary mesh used in the computation of the external force.

```

edNodes = find(controlPts(:,1)==0)';
tPoints = controlPts(forcedNodes,:);
tEdgeMesh = zeros(noElemsV,q+1);
i=1:noElemsV

```

```
tEdgeMesh(i,:) = forcedNodes(i:i+q);
```

4.6. Three dimensional IGA

Based on the two dimensional IGA code previously presented, it is a straightforward task to implement a 3D formulation. After reading the NURBS data, the 3D mesh is created using the script **generateIGA3DMesh.m**. The assembly of the stiffness matrix is given in List 16 which is only a slight modification of List 14 for the 2D formulation.

Listing 16: Matlab[®] code for 3D IGA for elasticity

```
uss quadrature rule
]=quadrature(noGPs, 'GAUSS', 3);
semble system of equations
e=1:noElems
= index(e,1);
= index(e,2);
= index(e,3);
= elRangeU(idu,:); % [xi_i,xi_i+1]
= elRangeV(idv,:); % [eta_j,eta_j+1]
E = elRangeW(idw,:); % [zeta_k,zeta_k+1]
= element(e,:);
B = [sctr sctr+noCtrPts sctr+2*noCtrPts];
length(sctr);
op over Gauss points
gp=1:size(W,1)
Q(gp,:);
W(gp);
mpute coords in parameter space
parent2ParametricSpace(xiE,pt(1) );
= parent2ParametricSpace(etaE,pt(2) );
= parent2ParametricSpace(zetaE,pt(3));
jacobianPaPaMapping3d(xiE,etaE,zetaE);
```

```

rivative of basis functions w.r.t parameter coord
Rdxi dRdeta dRdzeta] = NURBS3DBasisDers([Xi;Eta;Zeta],...
r,uKnot,vKnot,wKnot,weights');
compute the jacobian, spatial derivatives
= controlPts(sctr,:);
b = pts'*[dRdxi' dRdeta' dRdzeta'];
det(jacob);
acob = inv(jacob);
= [dRdxi' dRdeta' dRdzeta'] * invJacob;
matrix
strainDispMatrix3d(nn,dRdx);
compute elementary stiffness matrix and
semble into global stiffness matrix
trB,sctrB) = K(sctrB,sctrB) + B'*C*B*J1*J2*wt;

```

As an example to illustrate 3D IGA, the pinched cylinder shown in Fig. (24) is analysed. A quadratic NURBS mesh ($p = q = r = 2$) was used for discretisation. Details can be found in the file **igaPinchedCylinder.m**. Figure 25 shows the mesh and the contour plot of the displacement in the point load direction. Post-processing is achieved through Paraview where more details can be found in Section 4.7. We recognise that the problem under consideration is a shell like structure that would be more accurately modelled using appropriate shell elements, but the example is merely intended to illustrate the ability of the method to analyse 3D geometries.

[Figure 24 about here.]

[Figure 25 about here.]

4.7. Post-processing

We present here a simple technique to visualize the IGA results, reusing available visualization techniques for finite elements. In the first step, a mesh consisting of four-noded quadrilateral (Q4) elements is generated (see Fig. (26)). In the second step, quantities of interest (e.g., stresses) are computed at the nodes of the Q4 mesh. This mesh along with nodal values can then be exported to a visualization program such as Paraview [58]. It should be emphasized that due to high order continuity of the NURBS basis, there is no need to perform nodal averaging as required in standard

C^0 finite element analysis. Listing 17 gives the Matlab[®] code for building the Q4 visualization mesh, computing the stresses at nodes and exporting the result to Paraview.

[Figure 26 about here.]

Listing 17: Matlab[®] code for post-processing.

```

dVisualizationMesh; % build Q4 mesh for visualization purposes
ss = zeros(noElems, size(elementV, 2), 3);
    = zeros(noElems, size(elementV, 2), 2);
e=1:noElems
= index(e, 1);
= index(e, 2);
= elRangeU(idu, :); % [xi_i, xi_i+1]
    = elRangeV(idv, :); % [eta_j, eta_j+1]
    = element(e, :); % element scatter vector
B = [sctr sctr+noCtrPts]; % vector that scatters a B matrix
    length(sctr);
zeros(3, 2*nn);
= controlPts(sctr, :);
n = FindSpan(noPtsX-1, p, xiE(1), uKnot);
n = FindSpan(noPtsY-1, q, etaE(1), vKnot);
op over Gauss points
    1;
iv=1:2
iv==2)
= sort(xiE, 'descend');

iu=1:2
    xiE(iu);
= etaE(iv);
Rdxi dRdeta] = NURBS2DBasisDersSpecial([Xi; Eta], ...

```

```

uKnot,vKnot,weights',[uspan;vspan]);
en the derivative w.r.t spatial physical coordinates
b = pts' * [dRdxi' dRdeta'];
acob = inv(jacob);
      = [dRdxi' dRdeta'] * invJacob;
matrix from dRdx as usual
1:nn) = dRdx(:,1)';

in = B*U(sctrB);
ss(e,gp,:) = C*strain;
gp +1;

ot contour directly in Matlab
ssComp=3;
re

_field(node,elementV,'Q4',stress(:,:,,stressComp));
on
rbar
e('Stress in x direction')
off
port to VTK format to plot in Paraview
aXX = zeros(size(node,1),1);
aYY = zeros(size(node,1),1);
aXY = zeros(size(node,1),1);
X = zeros(size(node,1),1);
Y = zeros(size(node,1),1);
e=1:size(elementV,1)

```

```

ect = elementV(e,:);
in=1:4
= connect(in);
aXX(nid) = stress(e,in,1);
aYY(nid) = stress(e,in,2);
aXY(nid) = stress(e,in,3);

ostProcess(node,elementV,2,'Quad4','out.vtu',...
maXX sigmaYY sigmaXY],[dispX dispY]);

```

For three-dimensional problems, the same procedure is used where a mesh of tri-linear brick elements is created and the values of interest are computed at the nodes of this mesh (see file **plotStress3d.m**).

4.8. Boundary condition enforcement

[Figure 27 about here.]

Figure 27 illustrates two kinds of Dirichlet boundary conditions: on edge AD , $u_x = 0$ and on edge BC , $u_y = \bar{u}$. The former is known as homogeneous Dirichlet boundary conditions (BCs) while the latter is referred to as uniform inhomogeneous Dirichlet BCs. Homogeneous Dirichlet BCs can be enforced by setting the corresponding control variables as zeros (in this example, setting $u_{xI} = 0, I = 2, 4, 6, 8$). For edge BC , the inhomogeneous Dirichlet BCs can also be satisfied by setting $u_{yI} = \bar{u}, I = 1, 3, 5, 7$. This is due to the partition of unity property of the NURBS basis i.e., $u_y^{BC} = M_1(\eta)u_{y1} + M_2(\eta)u_{y3} + M_3(\eta)u_{y5} + M_4(\eta)u_{y7} = (M_1(\eta) + M_2(\eta) + M_3(\eta) + M_4(\eta))\bar{u} = \bar{u}$. Inhomogeneous Dirichlet BCs applied on corner control points (black points in Fig. (27)) are enforced by simply setting the corner control variables equal to the prescribed values since the NURBS shape functions at these points satisfy the Kronecker delta property (assuming the use of open knot vectors). This is called direct imposition of Dirichlet BCs. For cases other than the ones previously discussed such as a prescribed displacement imposed at interior control point 3 or a non-uniform Dirichlet BC⁸ applied on edge BC , special treatment of Dirichlet BCs have to be employed as is the case for meshless methods. Techniques available include the Lagrange multiplier method, the penalty method, the augmented Lagrangian method and we refer to [59] for an overview of these techniques in the context of meshless methods. In

⁸Dirichlet BCs that vary from point to point.

[60] a transformation method has been proposed to impose inhomogeneous Dirichlet BCs in IGAFEM. The authors in [42] presented a weak enforcement of general inhomogeneous Dirichlet BCs using a least squares minimization and the implementation is described in what follows. The same procedure has been used in imposing BCs in meshless methods to couple a fluid to a solid domain through a master-slave concept [61]. The basic idea of the least squares method is to find the parameters of the boundary control points that minimize the following quantity

$$\begin{aligned} J &= \frac{1}{2} \sum_C \|\mathbf{u}(\mathbf{x}_C) - \bar{\mathbf{u}}(\mathbf{x}_C)\|^2 \\ &= \frac{1}{2} \sum_C \left\| \sum_A \Phi_A(\mathbf{x}_C) \mathbf{q}_A - \bar{\mathbf{u}}(\mathbf{x}_C) \right\|^2, \end{aligned} \quad (55)$$

where \mathbf{x}_C denotes a set of collocation points distributed on the essential boundary Γ_u , \mathbf{q}_A are the parameters of the control points defining Γ_u and Φ_A represents the NURBS basis functions that are non-zero at \mathbf{x}_C . For the sake of clarity, let us consider the case where there is only one collocation point and a quadratic basis (thus there are 3 non-zero Φ_A at \mathbf{x}_C). So, we have

$$J = \frac{1}{2} \|\Phi_1(\mathbf{x}_C) \mathbf{q}_1 + \Phi_2(\mathbf{x}_C) \mathbf{q}_2 + \Phi_3(\mathbf{x}_C) \mathbf{q}_3 - \bar{\mathbf{u}}(\mathbf{x}_C)\|^2. \quad (56)$$

The partial derivatives of J with respect to \mathbf{q}_i are given by

$$\begin{aligned} \frac{\partial J}{\partial \mathbf{q}_1} &= [\Phi_1(\mathbf{x}_C) \mathbf{q}_1 + \Phi_2(\mathbf{x}_C) \mathbf{q}_2 + \Phi_3(\mathbf{x}_C) \mathbf{q}_3 - \bar{\mathbf{u}}(\mathbf{x}_C)] \Phi_1(\mathbf{x}_C) \\ \frac{\partial J}{\partial \mathbf{q}_2} &= [\Phi_1(\mathbf{x}_C) \mathbf{q}_1 + \Phi_2(\mathbf{x}_C) \mathbf{q}_2 + \Phi_3(\mathbf{x}_C) \mathbf{q}_3 - \bar{\mathbf{u}}(\mathbf{x}_C)] \Phi_2(\mathbf{x}_C) \\ \frac{\partial J}{\partial \mathbf{q}_3} &= [\Phi_1(\mathbf{x}_C) \mathbf{q}_1 + \Phi_2(\mathbf{x}_C) \mathbf{q}_2 + \Phi_3(\mathbf{x}_C) \mathbf{q}_3 - \bar{\mathbf{u}}(\mathbf{x}_C)] \Phi_3(\mathbf{x}_C). \end{aligned} \quad (57)$$

The condition $\frac{\partial J}{\partial \mathbf{q}} = 0$ thus gives the following linear system

$$\begin{bmatrix} \Phi_1 \Phi_1 & \Phi_2 \Phi_1 & \Phi_3 \Phi_1 \\ \Phi_1 \Phi_2 & \Phi_2 \Phi_2 & \Phi_3 \Phi_2 \\ \Phi_1 \Phi_3 & \Phi_2 \Phi_3 & \Phi_3 \Phi_3 \end{bmatrix}_{\mathbf{x}_C} \begin{bmatrix} q_1^x & q_1^y \\ q_2^x & q_2^y \\ q_3^x & q_3^y \end{bmatrix} = \begin{bmatrix} \bar{u}_x(\mathbf{x}_C) \Phi_1(\mathbf{x}_C) & \bar{u}_y(\mathbf{x}_C) \Phi_1(\mathbf{x}_C) \\ \bar{u}_x(\mathbf{x}_C) \Phi_2(\mathbf{x}_C) & \bar{u}_y(\mathbf{x}_C) \Phi_2(\mathbf{x}_C) \\ \bar{u}_x(\mathbf{x}_C) \Phi_3(\mathbf{x}_C) & \bar{u}_y(\mathbf{x}_C) \Phi_3(\mathbf{x}_C) \end{bmatrix}. \quad (58)$$

By collecting all the NURBS basis at point \mathbf{x}_C in a column vector $\mathbf{N}(\mathbf{x}_C)$, the control points displacements in x and y directions in \mathbf{q}_x and \mathbf{q}_y , respectively, Eq. (58) can be written in a compact form as

$$\begin{aligned} (\mathbf{N}(\mathbf{x}_C) \mathbf{N}(\mathbf{x}_C)^T) \mathbf{q}_x &= \bar{u}_x(\mathbf{x}_C) \mathbf{N}(\mathbf{x}_C) \\ (\mathbf{N}(\mathbf{x}_C) \mathbf{N}(\mathbf{x}_C)^T) \mathbf{q}_y &= \bar{u}_y(\mathbf{x}_C) \mathbf{N}(\mathbf{x}_C). \end{aligned} \quad (59)$$

Repeating the same analysis for other collocation points \mathbf{x}_C on the Dirichlet boundary, one obtains the linear system $\mathbf{A} \mathbf{q} = \mathbf{b}$ with two different \mathbf{b} (one for the x component and the other for the y component). The dimension of \mathbf{A} is $n \times n$

where n denotes the number of control points defining the Dirichlet boundary. Having these boundary control points displacements, the enforcement of Dirichlet BCs (when solving $\mathbf{Ku} = \mathbf{f}$) are then treated as in standard FEM. We note that this procedure involves only control points that define the essential boundary. This is in sharp contrast to meshless shape functions such as the MLS used in the Element Free Galerkin method [62] where the displacements at a point on the essential boundary depend on not only the nodes on that boundary but also the neighbouring interior nodes. The NURBS therefore satisfy the so-called weak Kronecker delta property. Listing 18 gives the Matlab[®] implementation of the least-squares method. We refer to Fig. (28) for an illustration of this method.

[Figure 28 about here.]

Listing 18: Matlab[®] implementation of the least-squares method

```

zeros(noDispNodes ,noDispNodes);
  zeros(noDispNodes ,1);
  zeros(noDispNodes ,1);
  = 4; % number of collocation pts/element
op over bottom edge
ie=1:noElemsU
  = bottomEdgeMeshIGA(ie,:); % standard connectivity array
  = controlPts(sctr,:); % control pts of element ie
A = bndElement(ie,:); % connectivity array for A matrix
  = elRangeU(ie,:); % parametric coords of ie
r = linspace(xiE(1),xiE(2),noxC); % collocation pts x_C
ic=1:noxC
  xiArr(ic);
Ndx] = NURBS1DBasisDers(xi,p,uKnot,weights);
trA,sctrA) = A(sctrA,sctrA) + N'*N;
N *pts;
act displacements
uy] = exact_Griffith(x,E0,nu0,sigmat0,xTip,seg,cracklength);
ctrA) = bx(sctrA) + ux*N';
ctrA) = by(sctrA) + uy*N';

```



```

op over other edges if neccessary
lve the system Aq_x=bx and Aq_y=by
UU] = lu(A);
mp = LL\bx;
mp = LL\by;
UU\qxTemp;
UU\qyTemp;
ter, before solving Ku=f, qx and qy will be used
enforce BCs as in conventional FEM.

```

In our Matlab[®] code implementation are provided for the penalty method, the Lagrange multiplier method and the least squares method. The implementation of the two former methods are considered standard and the reader is referred to [59] for details.

5. Extended isogeometric finite element method

Inspired by the extended finite element method (XFEM) (see e.g., [41] and [63] for a recent review), a 2D extended isogeometric finite element formulation (XIGA) has been presented in [42, 43] in which the displacement field is enriched for traction-free crack modelling using the following approximation

$$\mathbf{u}^h(\mathbf{x}) = \sum_{I \in \mathcal{S}} \Phi_I(\mathbf{x}) \mathbf{u}_I + \sum_{J \in \mathcal{S}^c} \Phi_J(\mathbf{x}) H(\mathbf{x}) \mathbf{a}_J + \sum_{K \in \mathcal{S}^f} \Phi_K(\mathbf{x}) \left(\sum_{\alpha=1}^4 B_\alpha \mathbf{b}_K^\alpha \right), \quad (60)$$

where $\Phi_{I,J,K}$ are NURBS basis functions. In addition to the standard dofs \mathbf{u}_I , additional dofs \mathbf{a}_J and \mathbf{b}_K^α are introduced. The set \mathcal{S}^c includes the nodes whose support is cut by the crack and the set \mathcal{S}^f are nodes whose support contains the crack tip \mathbf{x}_{tip} , see Fig. (29). Note that we use a topological tip enrichment and in the literature another tip enrichment scheme called geometrical enrichment with a fixed area (to ensure that the role of enrichment in the approximation space does not vanish as the mesh is refined) is present see e.g., [64]. The Heaviside function $H(\mathbf{x})$ is given by

$$H(\mathbf{x}) = \begin{cases} +1 & \text{if } (\mathbf{x} - \mathbf{x}^*) \cdot \mathbf{n} \geq 0 \\ -1 & \text{otherwise} \end{cases} \quad (61)$$

where \mathbf{x}^* is the projection of point \mathbf{x} on the crack. And the branch functions are given by

$$[B_1, B_2, B_3, B_4] = \left[\sqrt{r} \sin \frac{\theta}{2}, \sqrt{r} \cos \frac{\theta}{2}, \sqrt{r} \sin \frac{\theta}{2} \cos \theta, \sqrt{r} \cos \frac{\theta}{2} \cos \theta \right], \quad (62)$$

where r and θ are polar coordinates in the local crack front coordinate system (see e.g., [41] for details). It is noted that B_1 is discontinuous along the crack face.

[Figure 29 about here.]

Using the standard Bubnov-Galerkin procedure as outlined in Section 4.5 the discrete system of equations $\mathbf{K}\mathbf{u} = \mathbf{f}$ are formed by an enlarged \mathbf{B} matrix given by

$$\mathbf{B} = \left[\mathbf{B}^{\text{std}} \mid \mathbf{B}^{\text{enr}} \right], \quad (63)$$

where \mathbf{B}^{std} is the standard \mathbf{B} and \mathbf{B}^{enr} is the enriched \mathbf{B} matrix:

$$\mathbf{B}_I^{\text{enr}} = \begin{bmatrix} (\Phi_I)_{,x} \Psi_I + \Phi_I(\Psi_I)_{,x} & 0 \\ 0 & (\Phi_I)_{,y} \Psi_I + \Phi_I(\Psi_I)_{,y} \\ (\Phi_I)_{,y} \Psi_I + \Phi_I(\Psi_I)_{,y} & (\Phi_I)_{,x} \Psi_I + \Phi_I(\Psi_I)_{,x} \end{bmatrix}. \quad (64)$$

Ψ_I may represent either the Heaviside function H or the branch functions B_α . The unknown vector \mathbf{u} contains both displacements and enriched dofs. This extended IGAFEM can be implemented within an available IGAFEM code with little modification following the ideas given in [59]. Fictitious control points are added to handle additional dofs \mathbf{a} and \mathbf{b} . We now present a way in which to select enriched nodes that reuse most of the tools present in an existing XFEM code.

Selection of enriched control points We use the approximate Q4 mesh used for visualization as discussed in Section 4.7 for selection of enriched control points. The level set values of the crack at the vertices of this mesh are then computed. Based on these level sets, elements cut by the crack and elements containing the crack tip can be determined [65]. For example, element ABCD in Fig. (29) is cut by the crack. In a FEM context, its four nodes are then enriched using the Heaviside function. In an isogeometric framework, however, the control points associated to this element are enriched. Listing 19 details the Matlab[®] implementation of this process. Note that this list is taken directly from our XFEM code [59] and the technique used is different and considered simpler than that adopted in [43]. We emphasize that the crack geometry is defined in the physical space in keeping with XFEM notation.

Listing 19: Selection of enriched nodes.

```
ch_node = zeros(noCtrPts,1);
t1 = 0;
```

```

t2 = 0;
iel = 1 : numelem
    = elementV(iel,:);
IGA = element(iel,:);
= ls(sctr,1); % normal level set
= ls(sctr,2); % tangent level set
max(phi)*min(phi) < 0 )
ax(psi) < 0
t1 = count1 + 1 ; % one split element
t_elem(count1) = iel;
ch_node(sctrIGA) = 1;
if max(psi)*min(psi) < 0
t2 = count2 + 1 ; % one tip element
elem(count2) = iel;
ch_node(sctrIGA) = 2;

t_nodes = find(enrich_node == 1);
nodes = find(enrich_node == 2);

```

Remark 5.1. Note that for simple geometries as those tackled in this paper, the use of level sets is certainly not necessary. More generally, describing open surfaces (cracks) with level sets requires two level sets functions that, for crack growth simulations, must be reinitialised for stability (this decreases accuracy) and reorthogonalised every few time steps. This is particularly cumbersome and justifies along with the difficulties in dealing intersecting and branching cracks the recent trend of research efforts in the area of phase field models of fracture, see e.g., [66, 67].

Crack visualization We have $H(\mathbf{x}^+) - H(\mathbf{x}^-) = 2$ and $B_1(\mathbf{x}^+) - B_1(\mathbf{x}^-) = 2\sqrt{r}$, therefore the displacement jump at a point \mathbf{x} on the crack face is given by

$$\llbracket \mathbf{u} \rrbracket(\mathbf{x}) = 2 \sum_{J \in \mathcal{S}^c} \Phi_J(\mathbf{x}) \mathbf{a}_J + 2\sqrt{r} \sum_{K \in \mathcal{S}^f} \Phi_K(\mathbf{x}) \mathbf{b}_K^1. \quad (65)$$

Note that other branch functions B_α , $\alpha = 2, 3, 4$ are continuous functions and thus do not contribute to the displacement jump.

[Figure 30 about here.]

[Figure 31 about here.]

Figure 30 illustrates the idea for crack visualization with the script `crackedMeshNURBS.m` providing implementation details. The contour plots of the displacement and stress field of a mode I cracked sample are given in Fig. (31). Note that the stresses at points on the crack are simply set to zero (traction-free cracks) and the stresses of the new nodes of the tip element are interpolated from the values of the four nodes of this Q4 element.

Remark 5.2. As is the case for XFEM, integration over elements cut by the cracks usually require subdivision of the elements into integration subcells. We refer to [68] for a recent discussion on this issue. In our current implementation, a simple integration rule is used—elements crossed by the crack and tip-enriched elements are numerically integrated using a regular Gauss-Legendre quadrature with a large number of Gauss points.

6. Verification examples

In this section, numerical examples in linear elasticity and linear elastic fracture mechanics in 2D and 3D are presented with the purpose to verify the discussed Matlab[®] code. They include the Timoshenko beam under bending, an infinite plate with a circular hole under constant in-plane tension, a plate with a center inclusion, an edge cracked plate in tension and a three-dimensional mode I fracture problem. Unless otherwise stated, standard direct imposition of Dirichlet BCs is used. Units are standard International System (SI) units.

6.1. Timoshenko beam

Consider a beam of dimensions $L \times D$, subjected to a parabolic traction at the free end as shown in Fig. (32). The beam is considered to be of unit depth and is in a state of plane stress. The imposed parabolic traction is given by

$$t_y(y) = -\frac{P}{2I} \left(\frac{D^2}{4} - y^2 \right), \quad (66)$$

where $I = D^3/12$ denotes the moment of inertia. The exact displacement field for this problem is given by [69]

$$\begin{aligned} u_x(x, y) &= \frac{Py}{6EI} \left[(6L - 3x)x + (2 + \nu) \left(y^2 - \frac{D^2}{4} \right) \right] \\ u_y(x, y) &= -\frac{P}{6EI} \left[3\nu y^2(L - x) + (4 + 5\nu) \frac{D^2 x}{4} + (3L - x)x^2 \right], \end{aligned} \quad (67)$$

and the exact stresses written as

$$\sigma_{xx}(x, y) = \frac{P(L-x)y}{I}; \quad \sigma_{yy}(x, y) = 0, \quad \sigma_{xy}(x, y) = -\frac{P}{2I} \left(\frac{D^2}{4} - y^2 \right). \quad (68)$$

Material properties are taken as $E = 3.0 \times 10^7$, $\nu = 0.3$ and the beam dimensions are $D = 12$ and $L = 48$. The shear force applied is $P = 1000$. The left edge of the beam is fixed in both directions. Table 1 demonstrates the convergence of u_y displacement at point $(L, -D/2)$ to the exact value under mesh refinement. The distribution of the vertical displacement u_y along the line $y = 0$ and comparison with exact solution is given in Fig. (34). A contour plot of σ_{xx} realized in Matlab[®] is shown in Fig. (35). A smooth stress distribution is obtained.

[Figure 32 about here.]

[Figure 33 about here.]

[Table 1 about here.]

[Figure 34 about here.]

[Figure 35 about here.]

Finally, the displacement and energy norms are evaluated with the energy norm given by

$$e_{\text{energy}} = \left[\frac{1}{2} \int_{\Omega} (\boldsymbol{\varepsilon}_{\text{num}} - \boldsymbol{\varepsilon}_{\text{exact}}) \cdot \mathbf{D} \cdot (\boldsymbol{\varepsilon}_{\text{num}} - \boldsymbol{\varepsilon}_{\text{exact}}) d\Omega \right]^{\frac{1}{2}}, \quad (69)$$

and the displacement norm defined as

$$e_{\text{displacement}} = \left\{ \frac{\int_{\Omega} [(\mathbf{u}_{\text{num}} - \mathbf{u}_{\text{exact}}) \cdot (\mathbf{u}_{\text{num}} - \mathbf{u}_{\text{exact}})] d\Omega}{\int_{\Omega} [\mathbf{u}_{\text{exact}} \cdot \mathbf{u}_{\text{exact}}] d\Omega} \right\}^{1/2}, \quad (70)$$

where $\boldsymbol{\varepsilon}_{\text{num}}$, and $\boldsymbol{\varepsilon}_{\text{exact}}$ are the numerical strain vector and exact strain vector, respectively. The same notation applies to the displacement vector \mathbf{u}_{num} and $\mathbf{u}_{\text{exact}}$. In the post-processing step, the above norms are calculated using the same Gauss-Legendre quadrature that has been adopted for the stiffness matrix computation. For the computation of the norms, the exact displacements given in Eq. (67) are imposed on the entire boundary of the beam using the least squares method. The results are shown in Fig. (37). The quadratic meshes used for this computation are given in Fig. (36) (meshes *b*, *c* and *d*). These three meshes are obtained from mesh *a* by the *h*-refinement described in Section 3.3.2 with one modification—the new knots are not inserted at the midpoints of the existing knots. The location of the new knots are defined in such a way that the resulting mesh in the physical space is uniform. We refer to [3] for a detailed description of this *h*-refinement algorithm.

[Figure 36 about here.]

[Figure 37 about here.]

6.2. Infinite plate with a circular hole

The next problem considered is that of an infinite plate with a circular hole in the centre under constant in-plane tension at infinity as shown in Fig. (38) where, due to symmetry, only a quarter of the plate is modeled. The plate dimension is taken to be $L \times L$ and the circular hole has a radius R . The exact stress field in the plate is given by

$$\sigma_{xx}(r, \theta) = 1 - \frac{R^2}{r^2} \left(\frac{3}{2} \cos 2\theta + \cos 4\theta \right) + \frac{3}{2} \frac{R^4}{r^4} \cos 4\theta \quad (71a)$$

$$\sigma_{yy}(r, \theta) = -\frac{R^2}{r^2} \left(\frac{1}{2} \cos 2\theta - \cos 4\theta \right) - \frac{3}{2} \frac{R^4}{r^4} \cos 4\theta \quad (71b)$$

$$\sigma_{xy}(r, \theta) = -\frac{R^2}{r^2} \left(\frac{1}{2} \sin 2\theta + \sin 4\theta \right) + \frac{3}{2} \frac{R^4}{r^4} \sin 4\theta, \quad (71c)$$

where r, θ are the usual polar coordinates centered at the center of the hole.

[Figure 38 about here.]

The material properties are specified as $E = 10^3$, Poisson's ratio $\nu = 0.3$ and the geometry is such that $L = 4$, $R = 1$. A plane stress condition is assumed. The problem is solved with quadratic NURBS meshes such as those shown in Fig. (18). The control points for the coarsest mesh are provided in Listing 7 and are reproduced from [3]. Figure 39, generated in Paraview, illustrates the contour plot of numerical σ_{xx} . Note that the stress concentration at point $(R, 3\pi/2)$ is well captured and a smooth stress field is obtained throughout.

[Figure 39 about here.]

Remark 6.1. Using the visualization technique described in Section 4.7 for this problem, a note should be made on the evaluation of the stress field at the top left corner where there are two coincident points. This causes a singular Jacobian matrix. Therefore at this corner, the stresses at a point slightly shifted from the original position are used.

Remark 6.2. Note that at the top left corner with coordinates $(-4, 4)$, there are two overlapping control points as detailed in Listing 7 and Fig. (16). We simply adopted a penalty formulation to enforce them to have the same displacement. This kind of constraint has the form $\mathbf{u}_a = \mathbf{u}_b$ and is described in [70].

The energy and displacement norms obtained with four meshes denoted by 8×4 , 16×8 , 32×16 and 64×32 elements are shown in Fig. (40). The exact displacements used for the computation of the displacement norm can be found in [69] or in [43].

[Figure 40 about here.]

6.3. Plate with a circular inclusion

The problem of an infinite plate with a center inclusion subjected to a uniaxial tension as shown in Fig. (41) is now studied. The material properties of the matrix are $E_1 = 1000$, $\nu_1 = 0.3$ with the material characteristics of the soft inclusion prescribed as $E_2 = 1$, $\nu_2 = 0.3$. Due to symmetry, only a quarter of the model is analysed. Symmetry boundary conditions are applied on the right and bottom edges of the model and a negative displacement ($\bar{u} = -0.04$) is applied on the left edge. The plate is discretized using quadratic ($p = q = 2$) NURBS meshes that are shown in Fig. (42). Across the matrix/inclusion interface, the strain field is discontinuous. This is modelled by using a knot $\mathcal{H} = [0, 0, 0, 0.15, 0.3, 0.3, 0.7, 1, 1, 1]$ in the radial direction. Note the knot $\eta = 0.3$ has a multiplicity of two ($= q$), therefore the basis functions are only C_0 at the interface. Listing 20 gives the data for the control points and weights for the coarse mesh (8 elements). It should be emphasized that this problem can also be solved by using a two-patch NURBS object—one patch for the inclusion and one for the matrix. Our Matlab[®] code provides also a simple implementation of a multi-patch IGA where an assumption was made on the compatibility at the interface of the connecting patches. We refer to the file `igaTBeamMultiPatches.m` for such an implementation.

[Figure 41 about here.]

[Figure 42 about here.]

[Figure 43 about here.]

Listing 20: Control points and weights for the 8 element mesh of the plate with a center inclusion, see file `plateInclusionC1Data.m`.

```
i8 = tan(pi/8);
rolPts = [0 0;0 0;0 0;0 0;
0; -0.3 0.3*tanPi8;-0.3*tanPi8 0.3; 0 0.3;
0;-0.6 tanPi8;-tanPi8 0.6; 0 0.6;
;-1 tanPi8;-tanPi8 1; 0 1;
```

```

0;-1.5 1.5*tanPi8;-1.5*tanPi8 1.5; 0 1.5;
0;-3.1 3.1*tanPi8;-3.1*tanPi8 3.1; 0 3.1;
;-4 4;-4 4;0 4];
t = [0 0 0 0.5 1 1 1];
t = [0 0 0 0.15 0.3 0.3 0.7 1 1 1];
sX = 4;
sY = 7;
2;
2;
= 0.5*(1+1/sqrt(2));
hts = ones(noPtsX*noPtsY,1);
hts([6,7,10,11,14,15,18,19,22,23]) = cont;

```

Note that at the top left corner with coordinates $(-4, 4)$, there are two overlapping control points. We simply adopted a penalty formulation to enforce them to have the same displacement. At the lower right corner, there are four coinciding control points. However no special treatment is needed since they are subject to zero Dirichlet boundary conditions. In Fig. (43), the distribution of σ_{xx} obtained with standard FEM (7016 three-noded triangular elements, 7230 dofs) and with IGAFEM (4556 dofs) is plotted. The smooth stress field obtained with IGAFEM is evident.

6.4. Edge cracked plate in tension

A plate of dimension $b \times 2h$ is loaded by a tensile stress $\sigma = 1.0$ over the top edge and bottom edge as shown in Fig. (44). In the computation, the displacement along the y -axis is fixed at the bottom edge and the bottom left corner is fixed in both x and y directions. The material parameters are $E = 10^3$ and $\nu = 0.3$. A plane strain condition is assumed. The reference mode I stress intensity factor (SIF) for this problem is given in [71] and is calculated as

$$K_I = F\left(\frac{a}{b}\right)\sigma\sqrt{\pi a}, \quad (72)$$

where a is the crack length, b is the plate width, and $F(a/b)$ is an empirical function. For $a/b \leq 0.6$, the function F is given by

$$F\left(\frac{a}{b}\right) = 1.12 - 0.23\left(\frac{a}{b}\right) + 10.55\left(\frac{a}{b}\right)^2 - 21.72\left(\frac{a}{b}\right)^3 + 30.39\left(\frac{a}{b}\right)^4. \quad (73)$$

In the present implementation, this problem is solved using both XFEM and an extended isogeometric formulation. The SIF is computed using an interaction integral. We refer to [41] for details.

[Figure 44 about here.]

We first verify the implementation of the XIGA code by comparing the XIGA result with the XFEM result for the case of $a = 0.45$, $b = 1$ and $h = 1$. The XFEM and XIGA meshes are given in Fig. (45). Both meshes have the same uniform distribution of nodes. For the XFEM mesh, bilinear Q4 elements are used. For the XIGA mesh, cubic ($p = q = 3$) B-spline basis functions are adopted. Figure 46 shows the contour plots of the vertical displacement obtained with XFEM and XIGA.

[Figure 45 about here.]

[Figure 46 about here.]

We now consider the computation of the mode I SIF for a crack of length $a = 0.3$. The reference SIF for this problem is $K_I^{\text{ref}} = 1.6118$. Both linear and cubic B-spline basis are used for three different meshes. The results are given in Table 2. It should be emphasized that in the computation of the interaction integral, we use bilinear Lagrange shape functions i.e., shape functions of Q4 elements to compute the derivatives of the weight function. This guarantees that the weight function takes a value of unity on an open set containing the crack tip and vanishes on an outer contour as shown in Fig. (47).

[Figure 47 about here.]

[Table 2 about here.]

6.5. Three-dimensional mode I fracture problem

This example aims to show the capability of our Matlab[®] code for solving three-dimensional (3D) fracture problems. For 3D cracks, the polar coordinates in the branch functions given in Eq. (62) are defined in terms of the level sets as [72]

$$r = \sqrt{\varphi(\xi, \eta, \zeta)^2 + \psi(\xi, \eta, \zeta)^2}, \quad \theta = \text{atan} \left(\frac{\varphi(\xi, \eta, \zeta)}{\psi(\xi, \eta, \zeta)} \right), \quad (74)$$

where the level set field $\Phi = (\varphi, \psi)$ is interpolated as

$$\Phi(\xi, \eta, \zeta) = \sum_I \phi_I(\xi, \eta, \zeta) \Phi_I. \quad (75)$$

We refer to [72] for details concerning the derivatives of the branch functions with respect to the parametric coordinates (ξ, η, ζ) . The mode I 3D fracture problem we are solving is given in Fig. (48). The exact displacement field is given by

$$\begin{aligned} u_x(r, \theta) &= \frac{2(1+v)}{\sqrt{2\pi}} \frac{K_I}{E} \sqrt{r} \cos \frac{\theta}{2} \left(2 - 2v - \cos^2 \frac{\theta}{2} \right) \\ u_y(r, \theta) &= 0 \\ u_z(r, \theta) &= \frac{2(1+v)}{\sqrt{2\pi}} \frac{K_I}{E} \sqrt{r} \sin \frac{\theta}{2} \left(2 - 2v - \cos^2 \frac{\theta}{2} \right), \end{aligned} \tag{76}$$

where $K_I = \sigma\sqrt{\pi a}$ is the stress intensity factor, ν is Poisson's ratio and E is Young's modulus. In our example, $a = 100$ mm; $E = 10^7$ N/mm², $\nu = 0.3$, $\sigma = 10^4$ N/mm². On the bottom, right and top surfaces, essential BCs taken from Eq. (76) are imposed using the penalty method. A penalty parameter of $1e10$ was used. We note that this problem can be more effectively solved with two-dimensional elements. This example however aims at presenting how 3D extended IGA can be implemented. Furthermore, it also illustrates how Dirichlet BCs are enforced on surfaces rather than the usual case of line boundaries. To this end, a two-dimensional NURBS mesh for a given surface is generated from the set of control points that define this surface (see the file **surfaceMesh.m**).

[Figure 48 about here.]

The problem is first solved using a linear NURBS basis. A mesh of $9 \times 9 \times 1$ elements is used. The mesh, enriched nodes and comparison of the numerical deformed configuration against the exact profile are given in Fig. (49). Next, a mesh of $7 \times 7 \times 2$ elements is used where in the through-thickness direction there are two linear elements ($q = 1$) and for the two other directions, a quadratic basis ($p = r = 2$) is used. The result is given in Fig. (50) and we note a good qualitative agreement between Figs. (49) and (50).

[Figure 49 about here.]

[Figure 50 about here.]

7. Conclusion

We have presented a Matlab[®] implementation for two and three-dimensional isogeometric finite element analysis for linear elasticity. This paper is addressed to students or researchers who wish to learn the concepts of IGA in a clear and concise manner and is especially suited to those with solid mechanics applications in mind. NURBS are used throughout, where the underlying construction of the basis functions is detailed along with associated refinement algorithms essential for numerical analysis. Differences to conventional FE implementations are made clear with the

use of Matlab[®] source code to illustrate isogeometric FE concepts explicitly. In addition, the implementation of an isogeometric XFEM formulation for both two-dimensional and three-dimensional problems is described allowing for linear elastic fracture analysis. Through the development of the code, the benefits and shortcomings of isogeometric analysis are outlined. In particular, it is emphasized throughout the paper that the exact geometry is used at all stages of analysis and that, similarly to meshless methods, the NURBS basis functions used confer higher order continuity to the approximation. Although not presented, the code supports multi-patch analysis in which there is a compatibility between connecting patches. In addition, PUM enrichment for holes and inclusions is provided along with implementation of the least squares method for imposing essential boundary conditions. The code is available for download from <https://sourceforge.net/projects/cmcodes/>. The preliminary concepts and implementation details of isogeometric analysis have been described, but many challenges remain in the field. These include the creation of suitable volume discretisations from given CAD boundary representations, efficient integration schemes, a posteriori error estimators and adaptivity. We note that the present work relies entirely with NURBS-based isogeometric analysis which are known to exhibit several shortcomings. We plan to release T-spline versions of the code in due course, which will help reduce those limitations. Other avenues for future development of the code include interfacing the code with mainstream CAD software such as Rhino, CATIA, and including recent developments such as NURBS-enhanced FEM described in [46, 73, 74, 45, 75, 76, 77].

Acknowledgements

The first author would like to express his gratitude towards Professor L.J. Sluys at Delft University of Technology, The Netherlands for his support to VPN during the PhD period. The authors would like to acknowledge the partial financial support of the Framework Programme 7 Initial Training Network Funding under grant number 289361 “Integrating Numerical Simulation and Geometric Design Technology”. Stéphane Bordas also thanks partial funding for his time provided by 1) the EPSRC under grant EP/G042705/1 Increased Reliability for Industrially Relevant Automatic Crack Growth Simulation with the eXtended Finite Element Method and 2) the European Research Council Starting Independent Research Grant (ERC Stg grant agreement No. 279578) entitled “Towards real time multiscale simulation of cutting in non-linear materials with applications to surgical simulation and computer guided surgery”.

References

- [1] L. A. Piegl, W. Tiller, The NURBS Book, Springer, 1996.
- [2] D. F. Rogers, An Introduction to NURBS with Historical Perspective, Academic Press, 2001.

- [3] T. Hughes, J. Cottrell, Y. Bazilevs, Isogeometric analysis: CAD, finite elements, NURBS, exact geometry and mesh refinement, *Computer Methods in Applied Mechanics and Engineering* 194 (39-41) (2005) 4135–4195.
- [4] J. A. Cottrell, T. J. Hughes, Y. Bazilevs, *Isogeometric Analysis: Toward Integration of CAD and FEA*, Wiley, 2009.
- [5] I. Temizer, P. Wriggers, T. Hughes, Contact treatment in isogeometric analysis with NURBS, *Computer Methods in Applied Mechanics and Engineering* 200 (9-12) (2011) 1100–1112.
- [6] L. Jia, Isogeometric contact analysis: Geometric basis and formulation for frictionless contact, *Computer Methods in Applied Mechanics and Engineering* 200 (5-8) (2011) 726–741.
- [7] I. Temizer, P. Wriggers, T. Hughes, Three-Dimensional Mortar-Based frictional contact treatment in isogeometric analysis with NURBS, *Computer Methods in Applied Mechanics and Engineering* 209–212 (2012) 115–128.
- [8] L. De Lorenzis, I. Temizer, P. Wriggers, G. Zavarise, A large deformation frictional contact formulation using NURBS-bases isogeometric analysis, *International Journal for Numerical Methods in Engineering* 87 (13) (2011) 1278–1300.
- [9] W. A. Wall, M. A. Frenzel, C. Cyron, Isogeometric structural shape optimization, *Computer Methods in Applied Mechanics and Engineering* 197 (33-40) (2008) 2976–2988.
- [10] N. D. Manh, A. Evgrafov, A. R. Gersborg, J. Gravesen, Isogeometric shape optimization of vibrating membranes, *Computer Methods in Applied Mechanics and Engineering* 200 (13-16) (2011) 1343–1353.
- [11] X. Qian, O. Sigmund, Isogeometric shape optimization of photonic crystals via coons patches, *Computer Methods in Applied Mechanics and Engineering* 200 (25-28) (2011) 2237–2255.
- [12] X. Qian, Full analytical sensitivities in NURBS based isogeometric shape optimization, *Computer Methods in Applied Mechanics and Engineering* 199 (29-32) (2010) 2059–2071.
- [13] R. Simpson, S. Bordas, J. Trevelyan, T. Rabczuk, A two-dimensional isogeometric boundary element method for elastostatic analysis, *Computer Methods in Applied Mechanics and Engineering* 209–212 (2012) 87–100.
- [14] D. Benson, Y. Bazilevs, M. Hsu, T. Hughes, Isogeometric shell analysis: The Reissner–Mindlin shell, *Computer Methods in Applied Mechanics and Engineering* 199 (5-8) (2010) 276–289.

- [15] J. Kiendl, K. Bletzinger, J. Linhard, R. Wüchner, Isogeometric shell analysis with Kirchhoff-Love elements, *Computer Methods in Applied Mechanics and Engineering* 198 (49-52) (2009) 3902–3914.
- [16] D. Benson, Y. Bazilevs, M. Hsu, T. Hughes, A large deformation, rotation-free, isogeometric shell, *Computer Methods in Applied Mechanics and Engineering* 200 (13-16) (2011) 1367–1378.
- [17] L. Beirão da Veiga, A. Buffa, C. Lovadina, M. Martinelli, G. Sangalli, An isogeometric method for the Reissner-Mindlin plate bending problem, *Computer Methods in Applied Mechanics and Engineering* 209–212 (2012) 45–53.
- [18] T. Uhm, S. Youn, T-spline finite element method for the analysis of shell structures, *International Journal for Numerical Methods in Engineering* 80 (4) (2009) 507–536.
- [19] H. Gomez, T. Hughes, X. Nogueira, V. M. Calo, Isogeometric analysis of the isothermal Navier-Stokes-Korteweg equations, *Computer Methods in Applied Mechanics and Engineering* 199 (25-28) (2010) 1828–1840.
- [20] P. N. Nielsen, A. R. Gersborg, J. Gravesen, N. L. Pedersen, Discretizations in isogeometric analysis of Navier-Stokes flow, *Computer Methods in Applied Mechanics and Engineering* 200 (45-46) (2011) 3242–3253.
- [21] Y. Bazilevs, V. M. Calo, T. J. R. Hughes, Y. Zhang, Isogeometric fluid-structure interaction: theory, algorithms, and computations, *Computational Mechanics* 43 (2008) 3–37.
- [22] Y. Bazilevs, J. Gohean, T. Hughes, R. Moser, Y. Zhang, Patient-specific isogeometric fluid-structure interaction analysis of thoracic aortic blood flow due to implantation of the Jarvik 2000 left ventricular assist device, *Computer Methods in Applied Mechanics and Engineering* 198 (45-46) (2009) 3534–3550.
- [23] H. Gómez, V. M. Calo, Y. Bazilevs, T. Hughes, Isogeometric analysis of the Cahn-Hilliard phase-field model, *Computer Methods in Applied Mechanics and Engineering* 197 (49-50) (2008) 4333–4352.
- [24] C. V. Verhoosel, M. A. Scott, T. J. R. Hughes, R. de Borst, An isogeometric analysis approach to gradient damage models, *International Journal for Numerical Methods in Engineering* 86 (1) (2011) 115–134.
- [25] P. Fischer, M. Klassen, J. Mergheim, P. Steinmann, R. Müller, Isogeometric analysis of 2D gradient elasticity, *Computational Mechanics* 47 (2010) 325–334.
- [26] J. Cottrell, A. Reali, Y. Bazilevs, T. Hughes, Isogeometric analysis of structural vibrations, *Computer Methods in Applied Mechanics and Engineering* 195 (41-43) (2006) 5257–5296.

- [27] J. A. Evans, Y. Bazilevs, I. Babuška, T. Hughes, n-Widths, sup-infs, and optimality ratios for the k-version of the isogeometric finite element method, *Computer Methods in Applied Mechanics and Engineering* 198 (21-26) (2009) 1726–1741.
- [28] T. W. Sederberg, J. Zheng, A. Bakenov, A. Nasri, T-splines and T-NURCCs, *ACM Transactions on Graphics* 22 (2003) 477–484.
- [29] A. Buffa, D. Cho, G. Sangalli, Linear independence of the T-spline blending functions associated with some particular T-meshes, *Computer Methods in Applied Mechanics and Engineering* 1437-1445 (2010) 199.
- [30] M. Scott, X. Li, T. Sederberg, T. Hughes, Local refinement of analysis suitable T-splines, *Computer Methods in Applied Mechanics and Engineering* 213-216 (2012) 206–222.
- [31] Y. Bazilevs, V. Calo, J. Cottrell, J. Evans, T. Hughes, S. Lipton, M. Scott, T. Sederberg, Isogeometric analysis using T-splines, *Computer Methods in Applied Mechanics and Engineering* 199 (5-8) (2010) 229–263.
- [32] M. R. Dörfel, B. Jüttler, B. Simeon, Adaptive isogeometric analysis by local h-refinement with T-splines, *Computer Methods in Applied Mechanics and Engineering* 199 (5-8) (2010) 264–275.
- [33] M. A. Scott, M. J. Borden, C. V. Verhoosel, T. W. Sederberg, T. J. R. Hughes, Isogeometric finite element data structures based on Bézier extraction of T-splines, *International Journal for Numerical Methods in Engineering* 88 (2) (2011) 126–156.
- [34] H. Wang, Y. He, X. Li, X. Gu, H. Qin, Polycube splines, *Computer-Aided Design* 40 (2008) 721–733.
- [35] J. Deng, F. Chen, X. Li, C. Hu, W. Tong, Z. Yang, Y. Feng, Polynomial splines over hierarchical T-meshes, *Graphical Models* 70 (2008) 76–86.
- [36] T. Dokken, V. Skytt, Locally refined splines, in: *Proceedings of IV European Conference On Computational Mechanics. Solids, Structures and Coupled Problems in Engineering*, Paris, France, 2010.
- [37] N. Nguyen-Thanh, H. Nguyen-Xuan, S. Bordas, T. Rabczuk, Isogeometric analysis using polynomial splines over hierarchical T-meshes for two-dimensional elastic solids, *Computer Methods in Applied Mechanics and Engineering* 200 (21-22) (2011) 1892–1908.
- [38] N. Nguyen-Thanh, J. Kiendl, H. Nguyen-Xuan, R. Wüchner, K. Bletzinger, Y. Bazilevs, T. Rabczuk, Rotation free isogeometric thin shell analysis using PHT-splines, *Computer Methods in Applied Mechanics and Engineering* 200 (47-48) (2011) 3410–3424.

- [39] H. Kim, Y. Seo, S. Youn, Isogeometric analysis with trimming technique for problems of arbitrary complex topology, *Computer Methods in Applied Mechanics and Engineering* 199 (45-48) (2010) 2796–2812.
- [40] C. V. Verhoosel, M. A. Scott, R. de Borst, T. J. R. Hughes, An isogeometric approach to cohesive zone modeling, *International Journal for Numerical Methods in Engineering* 87 (15) (2011) 336–360.
- [41] N. Moës, J. Dolbow, T. Belytschko, A finite element method for crack growth without remeshing, *International Journal for Numerical Methods in Engineering* 46 (1) (1999) 131–150.
- [42] E. De Luycker, D. J. Benson, T. Belytschko, Y. Bazilevs, M. C. Hsu, X-FEM in isogeometric analysis for linear fracture mechanics, *International Journal for Numerical Methods in Engineering* 87 (6) (2011) 541–565.
- [43] S. S. Ghorashi, N. Valizadeh, S. Mohammadi, Extended isogeometric analysis for simulation of stationary and propagating cracks, *International Journal for Numerical Methods in Engineering* In Press.
- [44] F. Cirak, M. Ortiz, P. Schröder, Subdivision surfaces: a new paradigm for thin-shell finite-element analysis, *International Journal for Numerical Methods in Engineering* 47 (12) (2000) 2039–2072.
- [45] R. Sevilla, S. Fernández-Méndez, A. Huerta, NURBS-enhanced finite element method (NEFEM), *International Journal for Numerical Methods in Engineering* 76 (1) (2008) 56–83.
- [46] R. Sevilla, S. Fernández-Méndez, A. Huerta, 3D-NURBS-enhanced finite element method (NEFEM), *International Journal for Numerical Methods in Engineering* 88 (2) (2011) 103–125.
- [47] E. Cervera, J. Trevelyan, Evolutionary structural optimisation based on boundary representation of NURBS. Part I: 2D algorithms, *Computers and Structures* 83 (2005) 1902–1916.
- [48] M. Moumnassi, S. Belouettar, E. Béchet, S. Bordas, D. Quoirin, M. Potier-Ferry, Finite element analysis on implicitly defined domains: An accurate representation based on arbitrary parametric surfaces, *Computer Methods in Applied Mechanics and Engineering* 200 (5–8) (2011) 774 – 796.
- [49] D. Schillinger, L. Dedé, M. A. Scott, J. A. Evans, M. J. Borden, E. Rank, T. J. R. Hughes, An isogeometric design-through-analysis methodology based on adaptive hierarchical refinement of nurbs, immersed boundary methods, and t-spline cad surfaces, *Computer Methods in Applied Mechanics and Engineering* (0) (2012) –.
- [50] A. Vuong, C. Heinrich, B. Simeon, ISOGAT: a 2D tutorial MATLAB code for Isogeometric Analysis, *Computer Aided Geometric Design* 27 (8) (2010) 644–655.

- [51] C. de Falco, A. Reali, R. Vázquez., GeoPDEs: a research tool for Isogeometric Analysis of PDEs, *Advances in Engineering Software* 42 (12) (2011) 1020–1034.
- [52] D. Rypl, B. Patzák, From the finite element analysis to the isogeometric analysis in an object oriented computing environment, *Advances in Engineering Software* 44 (2012) 116–125.
- [53] D. J. Benson, Y. Bazilevs, E. De Luycker, M.-C. Hsu, M. Scott, T. J. R. Hughes, T. Belytschko, A generalized finite element formulation for arbitrary basis functions: From isogeometric analysis to XFEM, *International Journal for Numerical Methods in Engineering* 83 (6) (2010) 765–785.
- [54] Rhino, CAD modeling and design toolkit, www.rhino3d.com.
- [55] M. J. Borden, M. A. Scott, J. A. Evans, T. J. R. Hughes, Isogeometric finite element data structures based on Bézier extraction of NURBS, *International Journal for Numerical Methods in Engineering* 87 (15) (2011) 15–47.
- [56] T. Hughes, A. Reali, G. Sangalli, Efficient quadrature for NURBS-based isogeometric analysis, *Computer Methods in Applied Mechanics and Engineering* 199 (5-8) (2010) 301–313.
- [57] J. Chessa, Programming the finite element method with matlab, northwestern University, <http://www.tam.northwestern.edu/jfc795/Matlab/> (2002).
URL <http://www.tam.northwestern.edu/jfc795/Matlab/>
- [58] A. Henderson, ParaView Guide, A Parallel Visualization Application, Kitware Inc., 2007.
- [59] V. P. Nguyen, T. Rabczuk, S. Bordas, M. Duflo, Meshless methods: A review and computer implementation aspects, *Mathematics and Computers in Simulation* 79 (3) (2008) 763–813.
- [60] D. Wang, J. Xuan, An improved NURBS-based isogeometric analysis with enhanced treatment of essential boundary conditions, *Computer Methods in Applied Mechanics and Engineering* 199 (37-40) (2010) 2425–2436.
- [61] T. Rabczuk, R. Gracie, J. H. Song, T. Belytschko, Immersed particle method for fluid-structure interaction, *International Journal for Numerical Methods in Engineering* 81 (1) (2010) 48–71.
- [62] T. Belytschko, Y. Y. Lu, L. Gu, Element-free Galerkin methods, *International Journal for Numerical Methods in Engineering* 37 (1994) 229–256.
- [63] T. P. Fries, T. Belytschko, The extended/generalized finite element method: An overview of the method and its applications, *International Journal for Numerical Methods in Engineering* 84 (3) (2010) 253–304.

- [64] P. Laborde, J. Pommier, Y. Renard, M. Salaun, High order extended finite element method for cracked domains, *International Journal for Numerical Methods in Engineering* 190 (47) (2004) 6183–6200.
- [65] N. Sukumar, D. L. Chopp, N. Moës, T. Belytschko, Modelling holes and inclusions by level sets in the extended finite element method, *Computer Methods in Applied Mechanics and Engineering* 190 (2000) 6183–6200.
- [66] C. Miehe, F. Welschinger, M. Hofacker, Thermodynamically consistent phase-field models of fracture: Variational principles and multi-field FE implementations, *International Journal for Numerical Methods in Engineering* 83 (10) (2010) 1273–1311.
- [67] M. J. Borden, C. V. Verhoosel, M. A. Scott, T. J. Hughes, C. M. Landis, A phase-field description of dynamic brittle fracture, *Computer Methods in Applied Mechanics and Engineering* 217–220 (0) (2012) 77 – 95.
- [68] S. Natarajan, D. R. Mahapatra, S. P. A. Bordas, Integrating strong and weak discontinuities without integration subcells and example applications in an XFEM/GFEM framework, *International Journal for Numerical Methods in Engineering* 83 (3) (2010) 269–294.
- [69] S. P. Timoshenko, J. N. Goodier, *Theory of Elasticity*, McGraw-Hill, New York, 1987.
- [70] C. A. Felippa, Introduction to Finite Element Methods. Multifreedom constraints II (lecture notes), <http://www.colorado.edu/engineering/CAS/courses.d/IFEM.d/> (2001).
- [71] H. P. Tada, P. C. Paris, G. R. Irwin, *The Stress Analysis of Cracks Handbook*, Del Research Corporation, St. Louis, MO, 1985.
- [72] J. Shi, D. Chopp, J. Lua, N. Sukumar, T. Belytschko, Abaqus implementation of extended finite element method using a level set representation of three-dimensional fatigue crack growth and life predictions, *Engineering Fracture Mechanics* 77 (2010) 2840–2863.
- [73] R. Sevilla, S. Fernández-Méndez, A. Huerta, Comparison of high-order curved finite elements, *International Journal for Numerical Methods in Engineering* 87 (8) (2011) 719–734.
- [74] R. Sevilla, S. Fernández-Méndez, A. Huerta, NURBS-Enhanced Finite Element Method (NEFEM): a seamless bridge between CAD and FEM, *Archives of Computational Methods in Engineering* 18 (4) (2011) 441–484.
- [75] R. Sevilla, S. Fernández-Méndez, A. Huerta, NURBS-enhanced finite element method (NEFEM) for Euler equations, *International Journal of Numerical Methods in Fluids* 57 (9) (2008) 1051–1069.

- [76] R. Sevilla, S. Fernández-Méndez, A. Huerta, NURBS-enhanced finite element method (NEFEM), *International Journal for Numerical Methods in Engineering* 76 (1) (2008) 56–83.
- [77] R. Sevilla, S. Fernández-Méndez, Numerical integration over 2D NURBS shaped domains with applications to NURBS-enhanced FEM, *Finite Element Analysis and Design* 47 (10) (2011) 1209–1220.
- [78] M. Arroyo, M. Ortiz, Local maximum-entropy approximation schemes: a seamless bridge between finite elements and meshfree methods, *International Journal for Numerical Methods in Engineering* 65 (13) (2006) 2167–2202.
- [79] N. Sukumar, Construction of polygonal interpolants: a maximum entropy approach, *International Journal for Numerical Methods in Engineering* 61 (12) (2004) 2159–2181.

List of Figures

1 Linear and quadratic B-spline basis functions for a uniform knot vector $\Xi = \{0, 1, 2, 3, 4, 5, 6\}$. Note that for $p = 1$, we recover the standard Lagrange polynomial linear shape functions. This is similar to maximum entropy shape functions as proposed in [78, 79]. 62

2 Quadratic ($p = 2$) B-spline basis functions for an open non-uniform knot vector $\Xi = \{0, 0, 0, 1, 2, 3, 4, 4, 5, 5, 5\}$. Note the flexibility in the construction of basis functions with varying degrees of regularity. 63

3 A quadratic ($p = 2$) B-spline curve with a uniform open knot vector $\Xi = \{0, 0, 0, 1, 2, 3, 4, 5, 5, 5\}$. Control points are denoted by filled circles. Note that the curve is C^1 continuous everywhere except at the extremities where repeated knots are present. 64

4 A quadratic ($p = 2$) B-spline curve with a uniform open knot vector $\Xi = \{0, 0, 0, 1, 2, 3, 4, 4, 5, 5, 5\}$. Control points are denoted by filled green circles. Points corresponding to the knot values are denoted by red circles. Note that the curve is C^0 continuous at point \mathbf{P}_6 where the corresponding knot ($\xi = 4$) has a multiplicity of 2. 65

5 Knot insertion on a quadratic B-spline curve. The curve is not changed geometrically. Control points are denoted by filled green circles. Points corresponding to the knot values are denoted by red circles. These points divide the curve into segments or 'elements'. 66

6 $p + 1$ times knot insertion for a quadratic B-spline curve to introduce a C^{-1} discontinuity at $\xi = 0.5$. . . 67

7 Order elevation of a quadratic B-spline curve to cubic : B-spline curves and associated basis functions. . 68

8 Comparison between p - and k -refinement. 69

9 A bivariate cubic B-spline basis function with knots vectors $\Xi = \mathcal{H} = \{0, 0, 0, 0, 0.25, 0.5, 0.75, 1, 1, 1, 1\}$. 70

10 A 90° annular surface represented by a B-spline surface. Red points represent control points. Note that some control points are located outside the domain. 71

11 A C^1 B-spline surface for an L-shaped domain. The knots vectors are given as $\Xi = \{0, 0, 0, 0.5, 1, 1, 1\}$ and $\mathcal{H} = \{0, 0, 0, 1, 1, 1\}$. Note that there are four points in the ξ direction where the second and third points coincide (corner point on the left figure). 72

12 A B-spline surface representation of a half cylinder . The knots are $\Xi = \{0, 0, 0, 0.5, 0.5, 1, 1, 1\}$ and $\mathcal{H} = \{0, 0, 1, 1\}$. Green points denote control points. The figure was produced by the script **nurbs2d.m**. 73

13 The use of a NURBS curve to construct a quarter circle. The red curve indicates the B-spline curve (all weights are unity) which is unable to reproduce the circle exactly. For a NURBS curve with $w_1 = w_3 = 1$ and $w_2 = 1/\sqrt{2}$, the circular geometry is exact. 74

14 Example of a NURBS curve for a circle of unit radius. Note that the last control point coincides with the first point to close the circle. 75

15 Effect of decreasing weights on a NURBS curve: the weights at control point \mathbf{B}_4 are 1, 0.6 and 0.3 for the red, blue and cyan curves, respectively. As w_4 decreases the curve is pushed away from point \mathbf{B}_4 . . . 76

16 Control net and mesh for a plate with a circular hole. Knots vectors are defined as $\Xi = \{0, 0, 0, 0.5, 1, 1, 1\}$ and $\mathcal{H} = \{0, 0, 0, 1, 1, 1\}$. Note that, at the top left corner, there are two coinciding points. In the context of analysis, the right figure denotes a 'mesh'. 77

17 Mesh refinement using knot insertion on a B-spline surface. All refined meshes are generated from the initial mesh corresponding to the first figure on the left. 78

18 Mesh refinement with knot insertion for B-spline surfaces. 79

19 Definition of domains used for integration in isogeometric analysis. 80

20 One dimensional isogeometric analysis example: exact geometry, quadratic basis functions and mesh in the parametric space. 81

21 Comparison of the IGA result against the exact solution for the one dimensional PDE given in Eq. (33). 82

22	Two dimensional isogeometric analysis example: (a) exact geometry, (b) mesh in physical space and (c) mesh in the parametric space. The two rectangles are used to illustrate the control points belonging to each element.	83
23	Boundary mesh for external force computation. A linear basis is used in the η direction. Assume a traction is applied on the edge containing nodes 4, 8 and 12. The boundary mesh is composed of two linear isogeometric elements.	84
24	Pinched cylinder. Problem description and data [3].	85
25	Pinched cylinder: (a) mesh of one octant of the cylinder and (b) contour plot of the displacement in the direction of the point load.	86
26	Exact NURBS mesh (top left) and approximate Q4 mesh (top right) for visualization purposes. The nodes in the Q4 mesh are the intersections of ξ and η knot lines. The bottom figure shows a contour plot of the stress field in Paraview. It should be emphasized that the mesh in (b) can not give a smooth contour plot. The result given in (c) was obtained with a refined NURBS mesh (hence a refined Q4 mesh).	87
27	Illustration of imposing Dirichlet BCs. Black points denote corner control points where the NURBS basis satisfy the Kronecker delta property.	88
28	Illustration of the implementation of the least squares method: a quadratic NURBS surface with knot vectors $\Xi = \{0, 0, 0, 0.5, 1, 1, 1\}$ and $\mathcal{H} = \{0, 0, 0, 0.5, 1, 1, 1\}$. Essential BCs are imposed on the bottom and right edges. A one dimensional mesh for this boundary is created. The control points defining the essential boundary are numbered from one to the total number of boundary control points. Note that this numbering is required only for assembling the matrix \mathbf{A}	89
29	Illustration of enriched node sets \mathcal{S}^f and \mathcal{S}^c for a quadratic NURBS mesh. The thick red line denotes the crack.	90
30	Crack visualization in XIGA: (a) building a mesh that is compatible to the crack by putting double nodes along the crack (square nodes) and (b) the displacement jumps are assigned to these new nodes. Note that the square nodes in the tip element are only for compatibility purposes. Exact mode I displacements are imposed on the bottom, right and top edge using the Lagrange multiplier method while Neumann BCs from the exact stress field are enforced on the left edge. We refer to [59] for a detailed description of this problem.	91
31	Contour plots on a cracked mesh: (a) vertical displacement and (b) normal stress in the vertical direction.	92
32	Timoshenko beam.	93
33	Initial meshes for the Timoshenko beam. More refined meshes are created from these meshes using a global h -refinement (knot insertion) algorithm.	94
34	Timoshenko beam: distribution of vertical displacement u_y along the line $y = 0$ and comparison with exact solution. A quadratic NURBS mesh with 360 dofs was used.	95
35	Timoshenko beam: numerical σ_{xx}	96
36	Meshes of the Timoshenko beam for the computation of the energy and displacement norms: (a) initial mesh and (b,c,d,e) refined mesh obtained from (a) using a h -refinement. Circles denote the control points.	97
37	Timoshenko beam: energy and displacement norms. The mesh parameter h is defined as the ratio between the beam height and the number of elements in the vertical direction.	98
38	Infinite plate with a circular hole under constant in-plane tension: quarter model. Boundary conditions include: $u_y = 0$ (AB), $u_x = 0$ (CD), $\bar{\mathbf{t}}^T = (-\sigma_{xx}, -\sigma_{xy})$ (AE), $\bar{\mathbf{t}}^T = (\sigma_{xy}, \sigma_{yy})$ (ED).	99
39	Plate with a hole: distribution of numerical σ_{xx} obtained with a 32×16 quadratic mesh having 4488 dofs.	100
40	Infinite plate with a circular hole under constant in-plane tension: energy and displacement norms. The mesh parameter h is defined as the maximum distance (in the physical space) between diagonally opposite knots.	101

41	Infinite plate with a circular soft inclusion in uniaxial tension: geometry (square plate with a centered circular inclusion) and boundary conditions.	102
42	NURBS meshes for the plate with a center inclusion. Circles denote control points. The right mesh was obtained from the left mesh via the knot insertion process.	103
43	Stress distribution (σ_{xx}) in the plate: FEM and Isogeometric FEM solution.	104
44	Edge cracked plate in tension: geometry and loading.	105
45	Edge cracked plate: XFEM and XIGA meshes. Both have the same number of displacement dofs of 1296. The thick line denotes the crack. Square nodes denote tip enriched nodes whereas star nodes represent Heaviside enriched nodes.	106
46	Edge cracked plate: u_y contour plots on deformed configuration (enlargement factor of 30 used).	107
47	Distribution of weight function used in the computation of the interaction integral. Four-noded quadrilateral elements with bilinear Lagrange shape functions are used to interpolate the weight function.	108
48	Three-dimensional mode I fracture problem: infinite plate with a center planar crack. The plate thickness is 2, the crack length is 5 and the crack width is 2. The crack is located in the mid-plane of the plate.	109
49	Three-dimensional mode I fracture problem: mesh of linear NURBS elements and enriched control points (left); numerical deformed configuration (magnification factor of 40) superimposed on the exact deformed configuration (right).	110
50	Three-dimensional mode I fracture problem: mesh of quadratic NURBS elements and enriched control points (left); numerical deformed configuration (magnification factor of 40) superimposed on the exact deformed configuration (right).	111

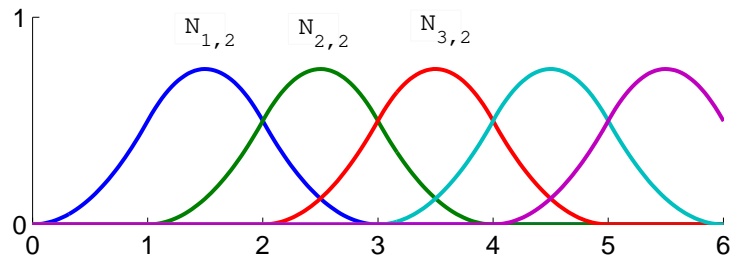
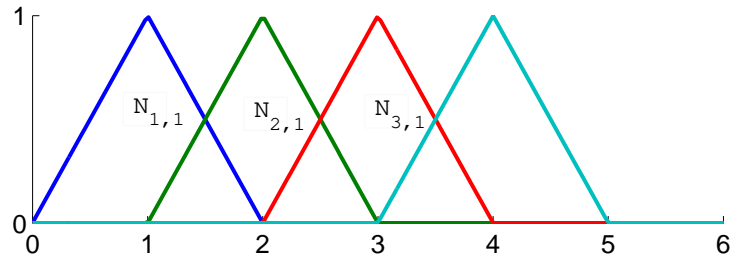


Figure 1: Linear and quadratic B-spline basis functions for a uniform knot vector $\Xi = \{0, 1, 2, 3, 4, 5, 6\}$. Note that for $p = 1$, we recover the standard Lagrange polynomial linear shape functions. This is similar to maximum entropy shape functions as proposed in [78, 79].

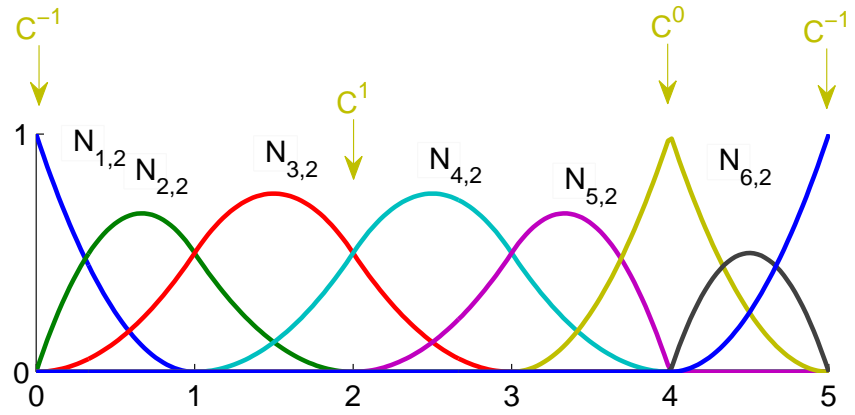


Figure 2: Quadratic ($p = 2$) B-spline basis functions for an open non-uniform knot vector $\Xi = \{0, 0, 0, 1, 2, 3, 4, 4, 5, 5, 5\}$. Note the flexibility in the construction of basis functions with varying degrees of regularity.

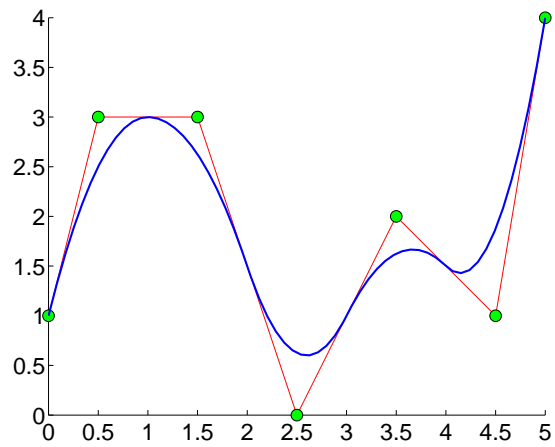


Figure 3: A quadratic ($p = 2$) B-spline curve with a uniform open knot vector $\Xi = \{0, 0, 0, 1, 2, 3, 4, 5, 5, 5\}$. Control points are denoted by filled circles. Note that the curve is C^1 continuous everywhere except at the extremities where repeated knots are present.

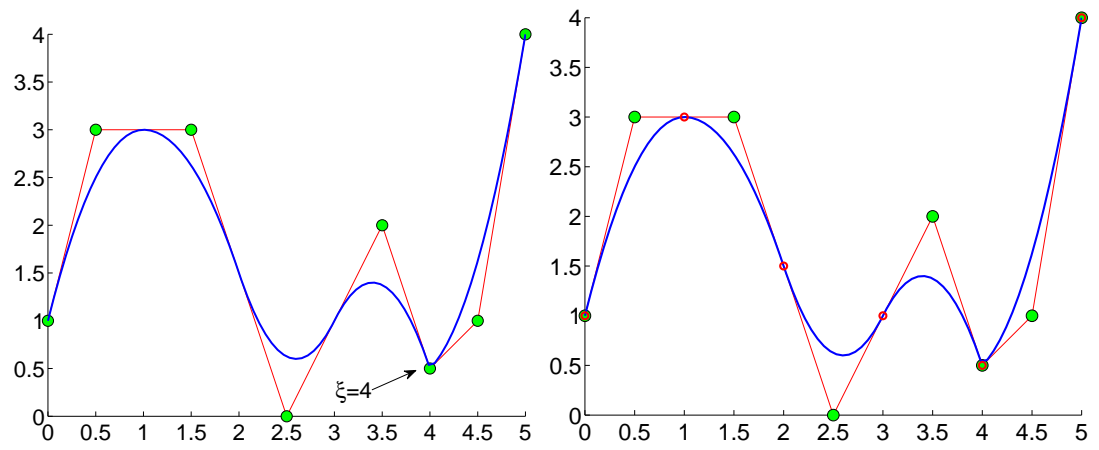


Figure 4: A quadratic ($p = 2$) B-spline curve with a uniform open knot vector $\Xi = \{0, 0, 0, 1, 2, 3, 4, 4, 5, 5, 5\}$. Control points are denoted by filled green circles. Points corresponding to the knot values are denoted by red circles. Note that the curve is C^0 continuous at point \mathbf{P}_6 where the corresponding knot ($\xi = 4$) has a multiplicity of 2.

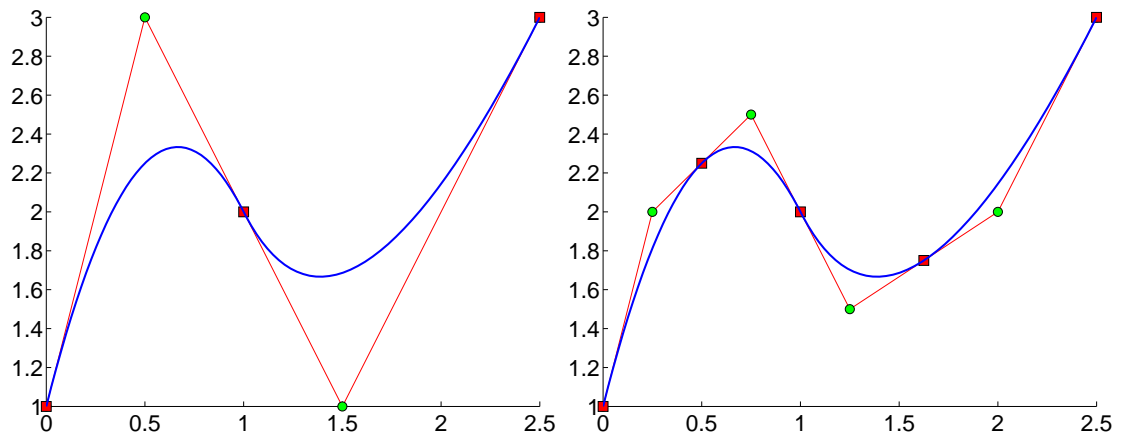


Figure 5: Knot insertion on a quadratic B-spline curve. The curve is not changed geometrically. Control points are denoted by filled green circles. Points corresponding to the knot values are denoted by red circles. These points divide the curve into segments or 'elements'.

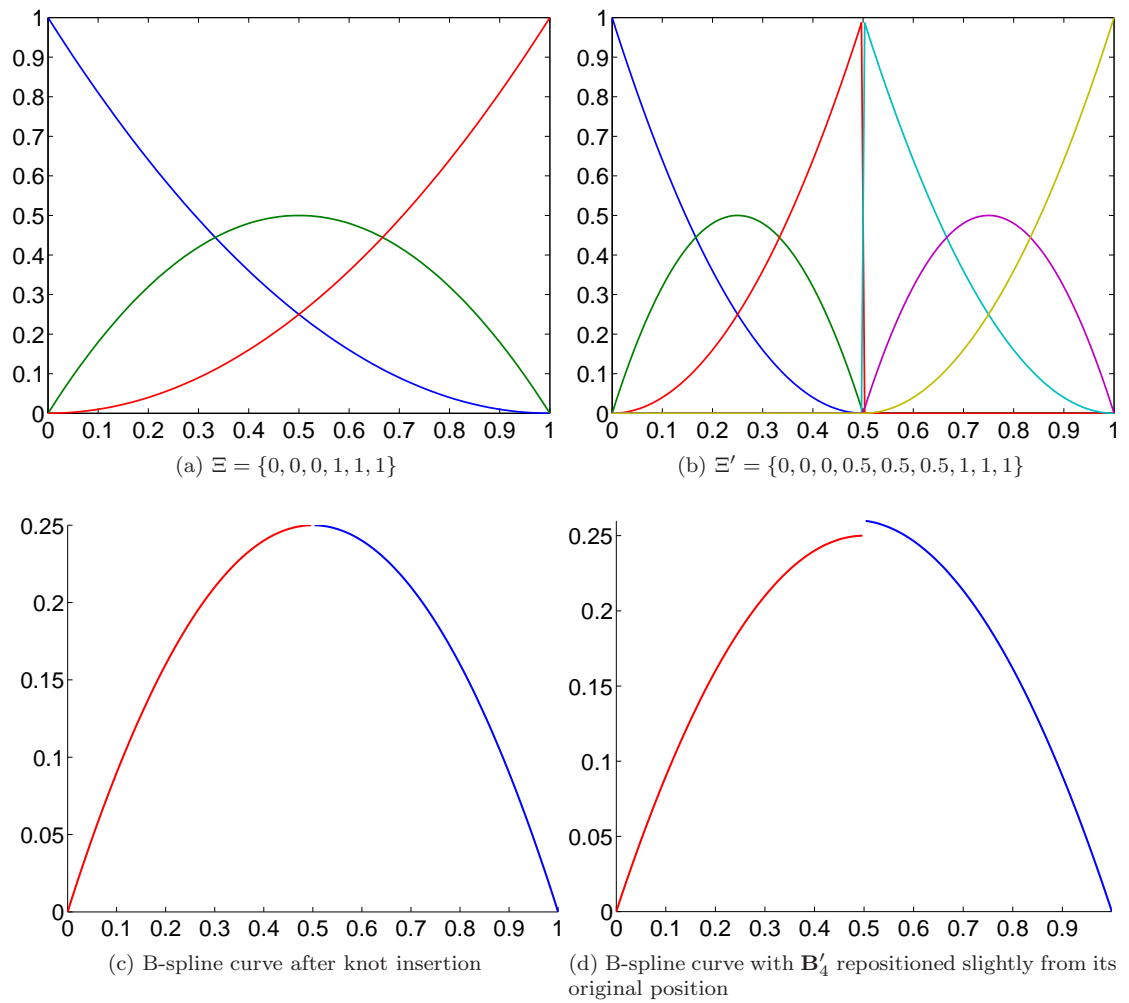


Figure 6: $p + 1$ times knot insertion for a quadratic B-spline curve to introduce a C^{-1} discontinuity at $\xi = 0.5$.

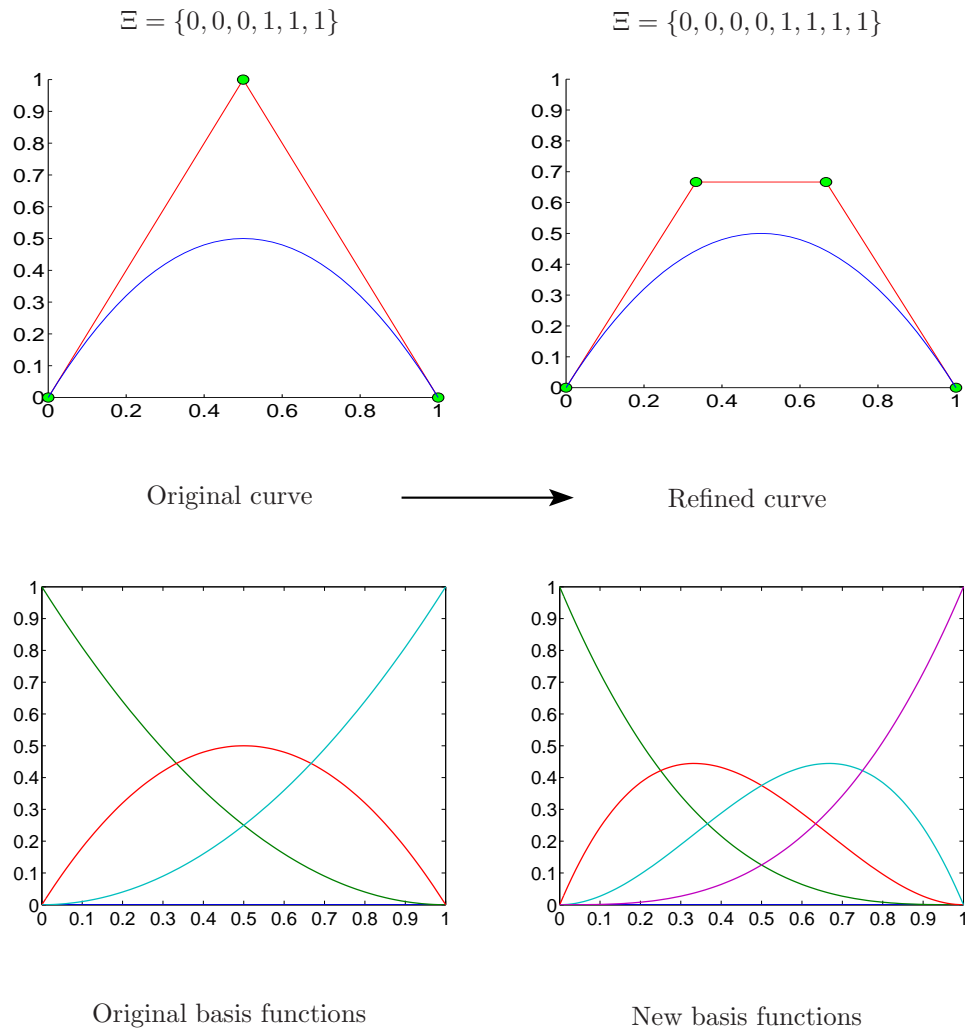


Figure 7: Order elevation of a quadratic B-spline curve to cubic : B-spline curves and associated basis functions.

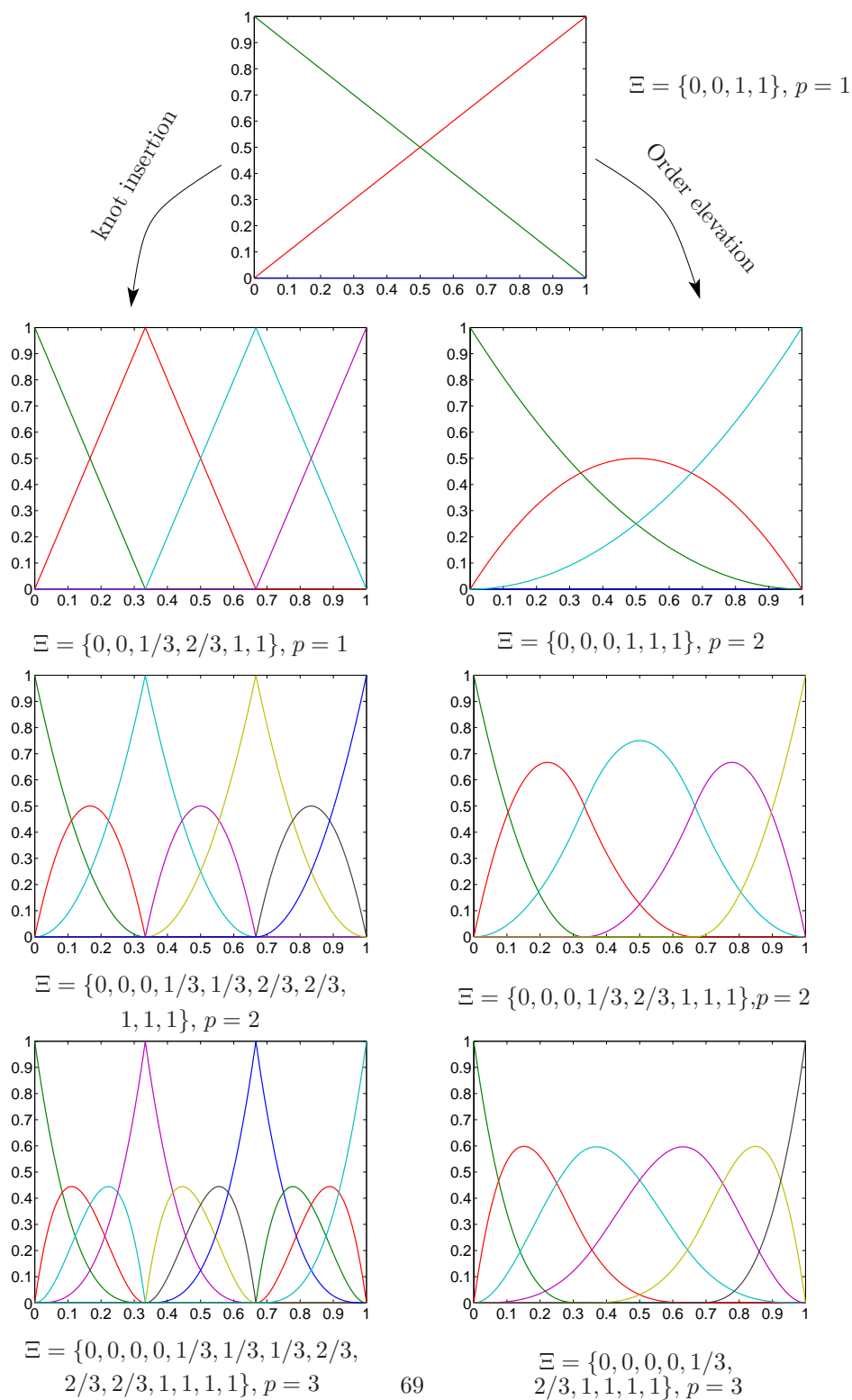


Figure 8: Comparison between p - and k -refinement.

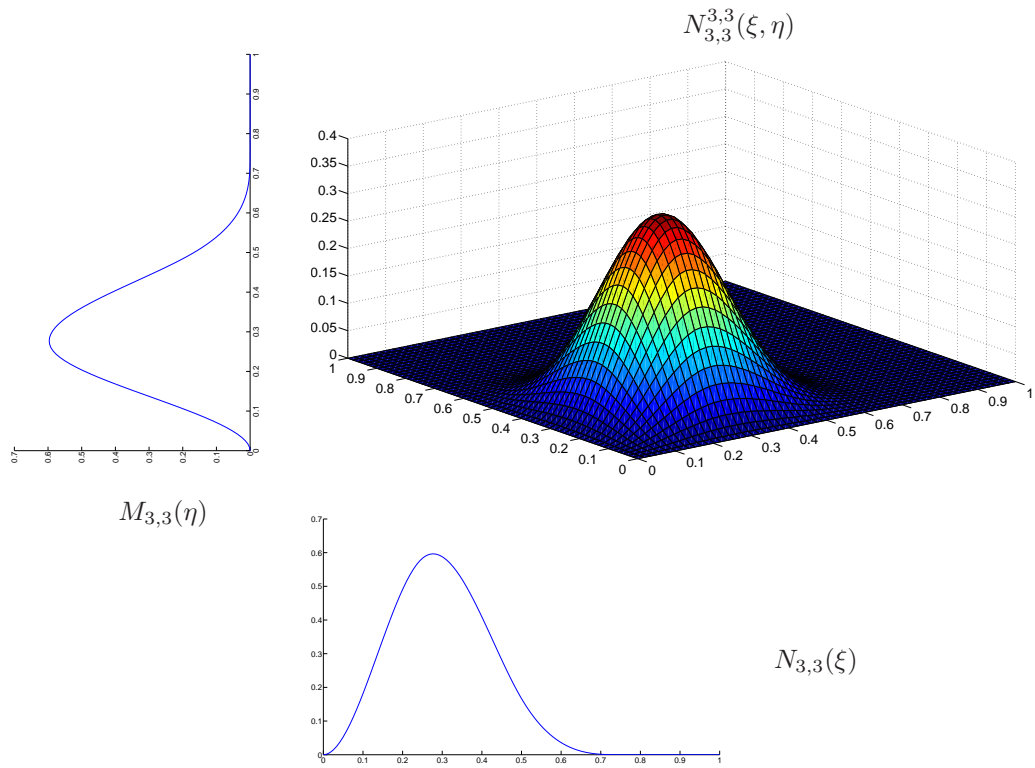


Figure 9: A bivariate cubic B-spline basis function with knots vectors $\Xi = \mathcal{H} = \{0, 0, 0, 0, 0.25, 0.5, 0.75, 1, 1, 1, 1\}$.

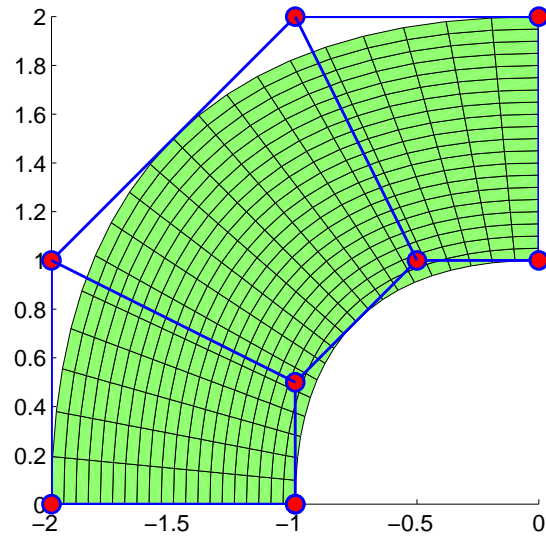


Figure 10: A 90° annular surface represented by a B-spline surface. Red points represent control points. Note that some control points are located outside the domain.

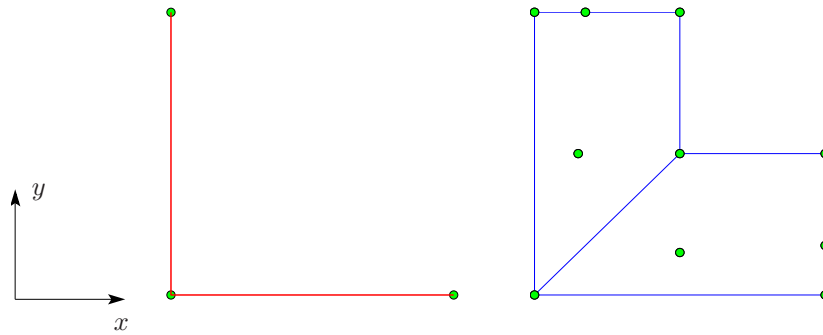


Figure 11: A C^1 B-spline surface for an L-shaped domain. The knots vectors are given as $\Xi = \{0, 0, 0, 0.5, 1, 1, 1\}$ and $\mathcal{H} = \{0, 0, 0, 1, 1, 1\}$. Note that there are four points in the ξ direction where the second and third points coincide (corner point on the left figure).

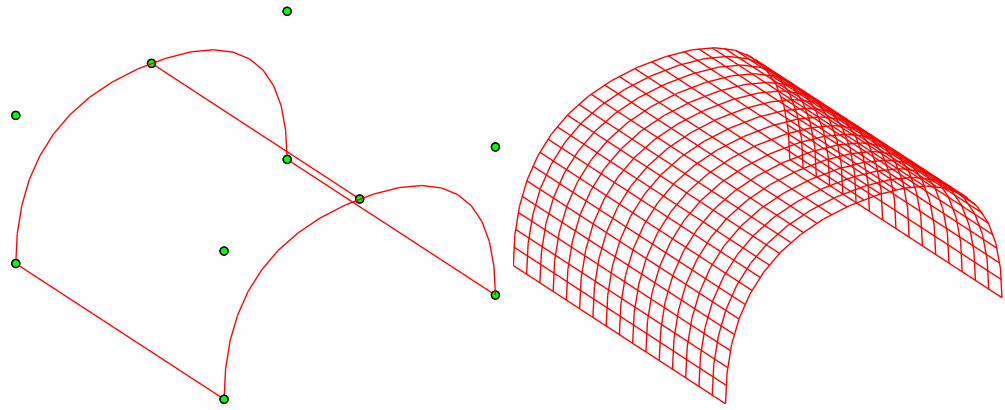


Figure 12: A B-spline surface representation of a half cylinder . The knots are $\Xi = \{0, 0, 0, 0.5, 0.5, 1, 1, 1\}$ and $\mathcal{H} = \{0, 0, 1, 1\}$. Green points denote control points. The figure was produced by the script **nurbs2d.m**.

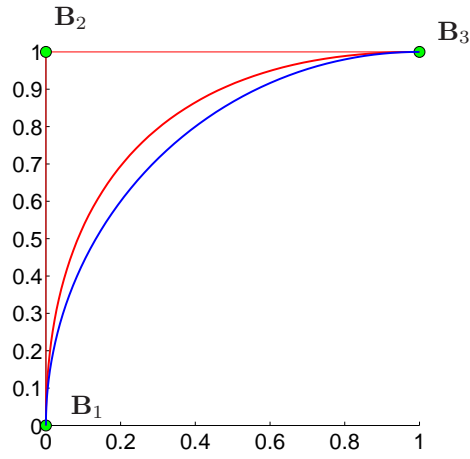


Figure 13: The use of a NURBS curve to construct a quarter circle. The red curve indicates the B-spline curve (all weights are unity) which is unable to reproduce the circle exactly. For a NURBS curve with $w_1 = w_3 = 1$ and $w_2 = 1/\sqrt{2}$, the circular geometry is exact.

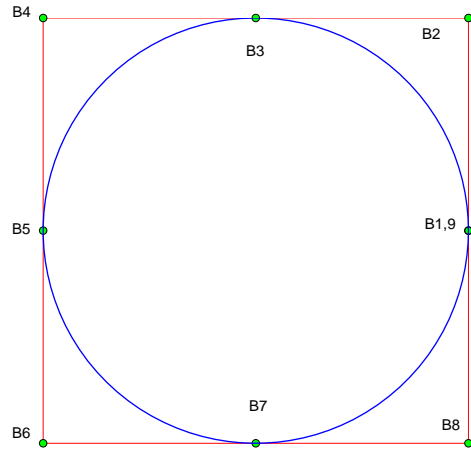


Figure 14: Example of a NURBS curve for a circle of unit radius. Note that the last control point coincides with the first point to close the circle.

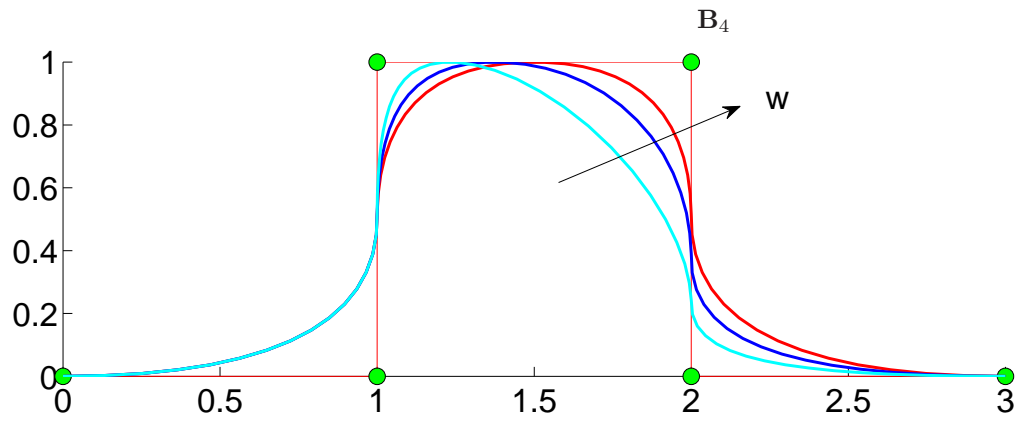


Figure 15: Effect of decreasing weights on a NURBS curve: the weights at control point B_4 are 1, 0.6 and 0.3 for the red, blue and cyan curves, respectively. As w_4 decreases the curve is pushed away from point B_4 .

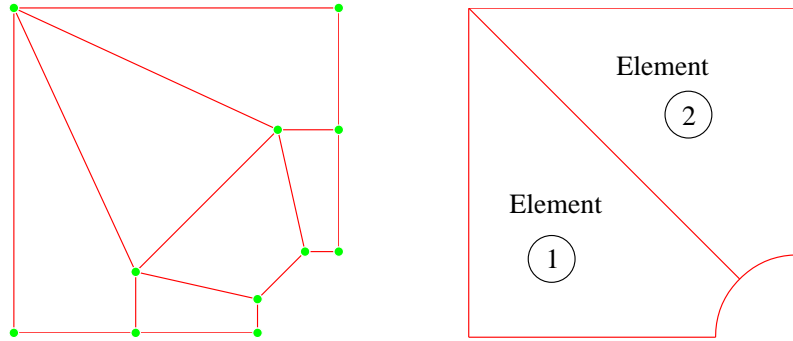


Figure 16: Control net and mesh for a plate with a circular hole. Knots vectors are defined as $\Xi = \{0, 0, 0, 0.5, 1, 1, 1\}$ and $\mathcal{H} = \{0, 0, 0, 1, 1, 1\}$. Note that, at the top left corner, there are two coinciding points. In the context of analysis, the right figure denotes a ‘mesh’.

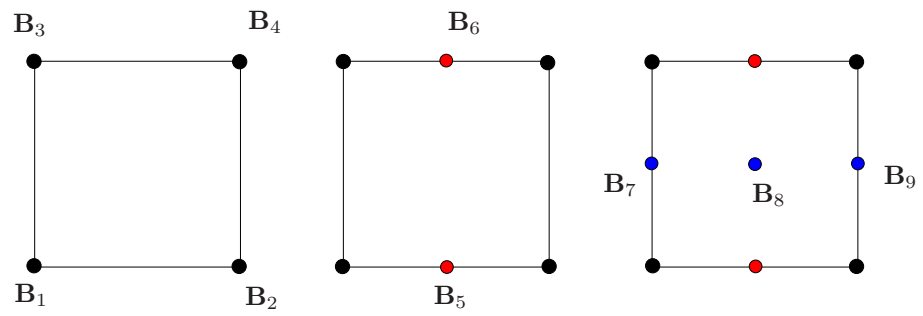


Figure 17: Mesh refinement using knot insertion on a B-spline surface. All refined meshes are generated from the initial mesh corresponding to the first figure on the left.

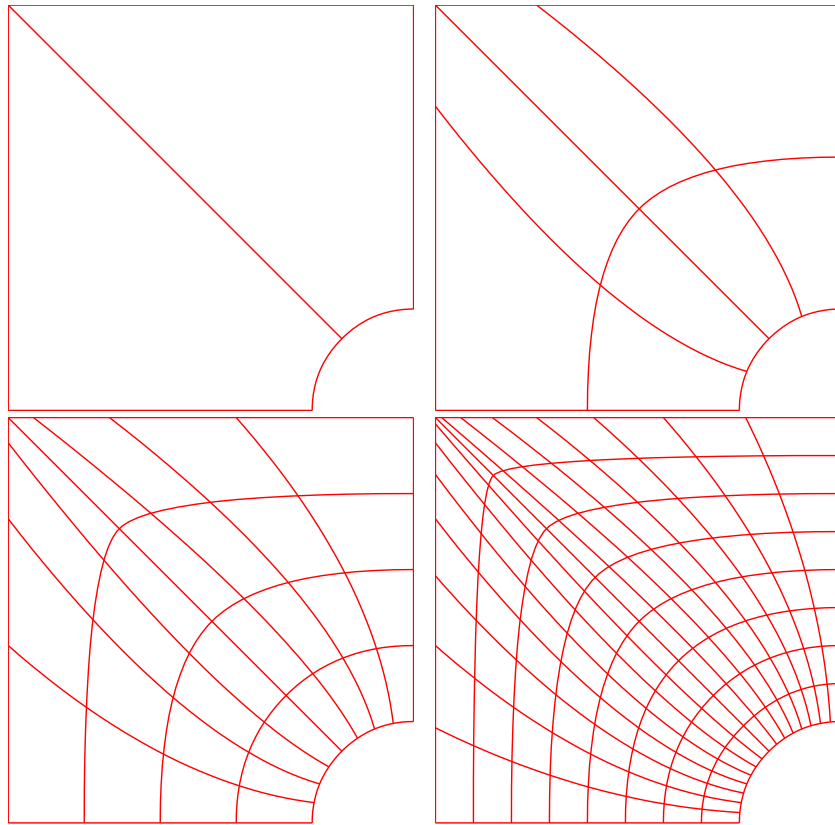


Figure 18: Mesh refinement with knot insertion for B-spline surfaces.

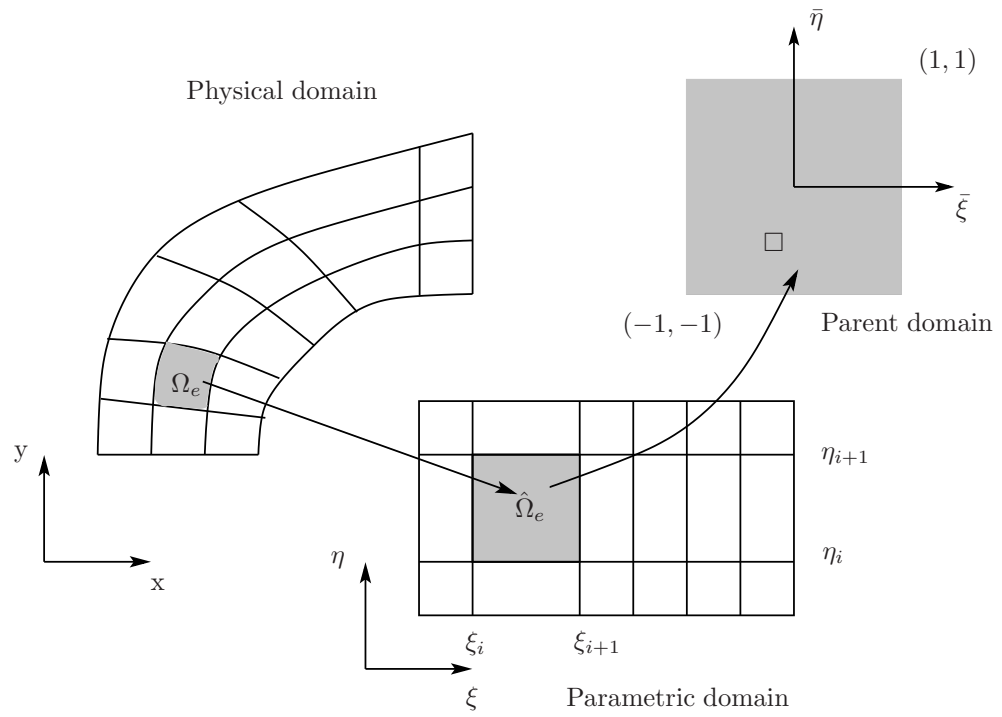
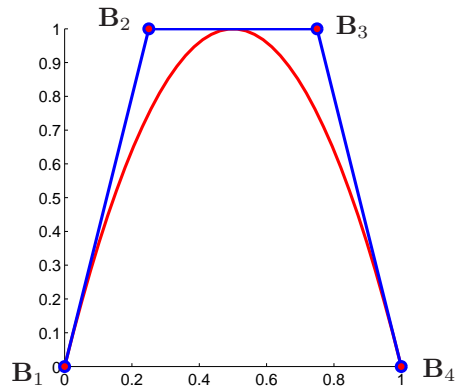
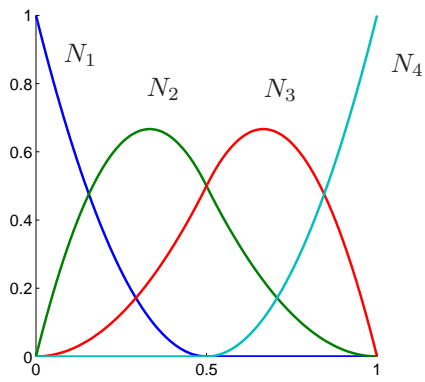


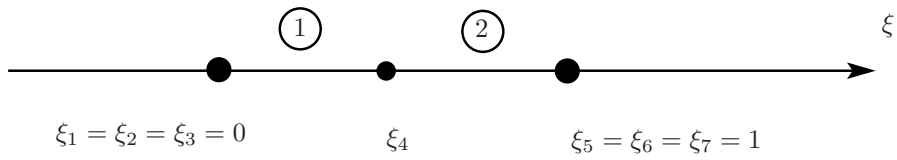
Figure 19: Definition of domains used for integration in isogeometric analysis.



A quadratic B-spline curve with 4 control points

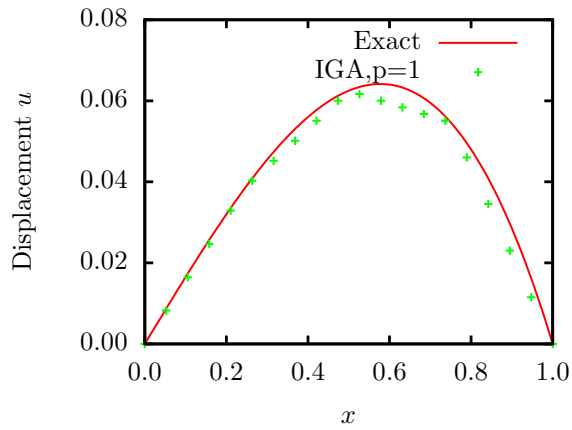


4 quadratic basis functions

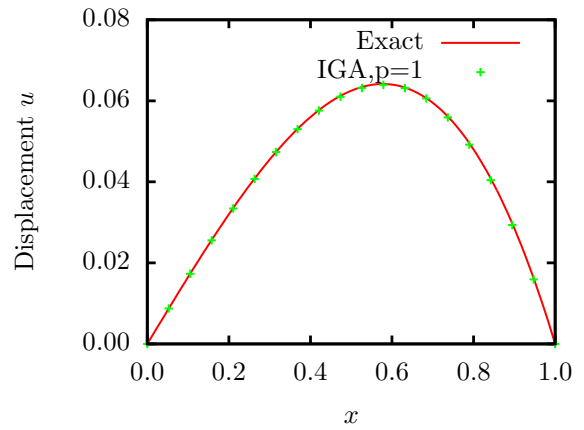


Parametric space

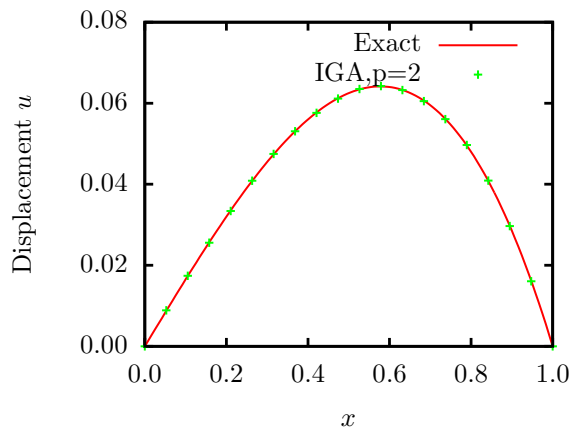
Figure 20: One dimensional isogeometric analysis example: exact geometry, quadratic basis functions and mesh in the parametric space.



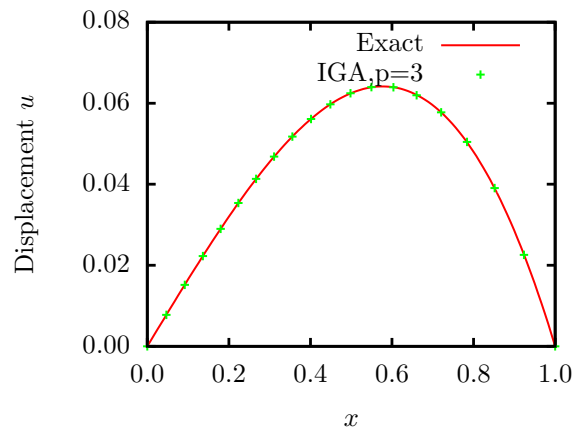
(a) 4 elements



(b) 16 elements



(c) 4 elements



(d) 4 elements

Figure 21: Comparison of the IGA result against the exact solution for the one dimensional PDE given in Eq. (33).

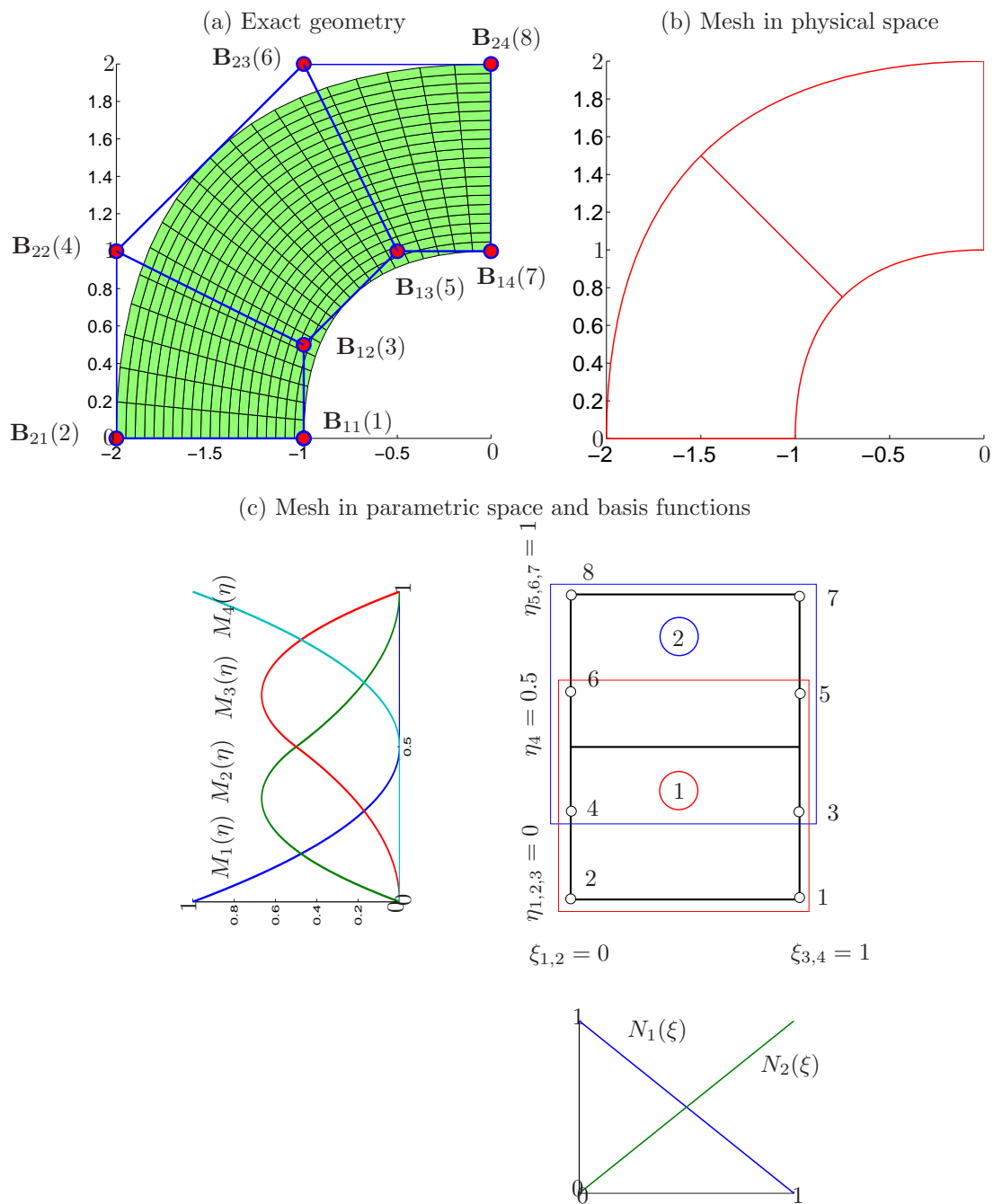


Figure 22: Two dimensional isogeometric analysis example: (a) exact geometry, (b) mesh in physical space and (c) mesh in the parametric space. The two rectangles are used to illustrate the control points belonging to each element.

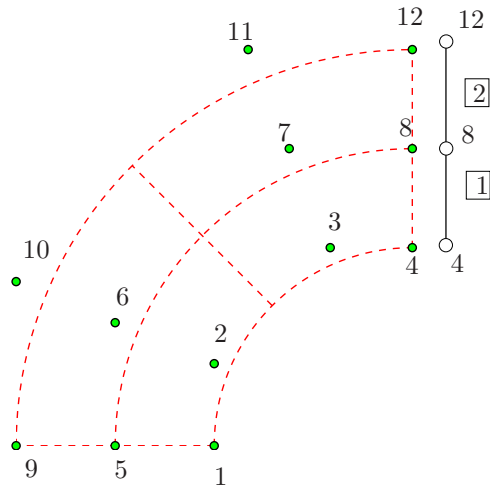


Figure 23: Boundary mesh for external force computation. A linear basis is used in the η direction. Assume a traction is applied on the edge containing nodes 4, 8 and 12. The boundary mesh is composed of two linear isogeometric elements.

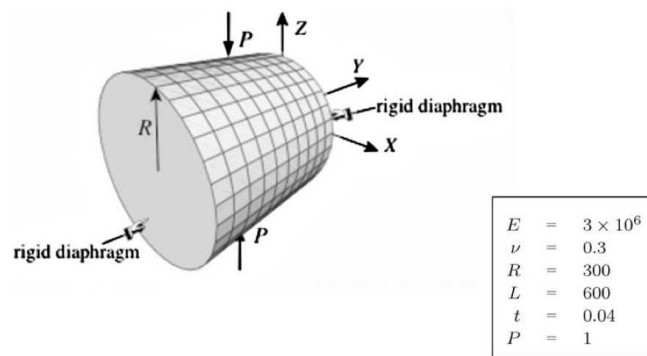


Figure 24: Pinched cylinder. Problem description and data [3].

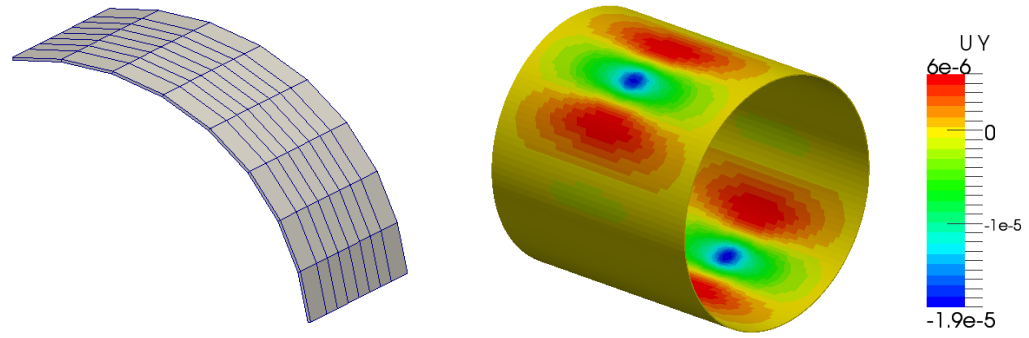


Figure 25: Pinched cylinder: (a) mesh of one octant of the cylinder and (b) contour plot of the displacement in the direction of the point load.

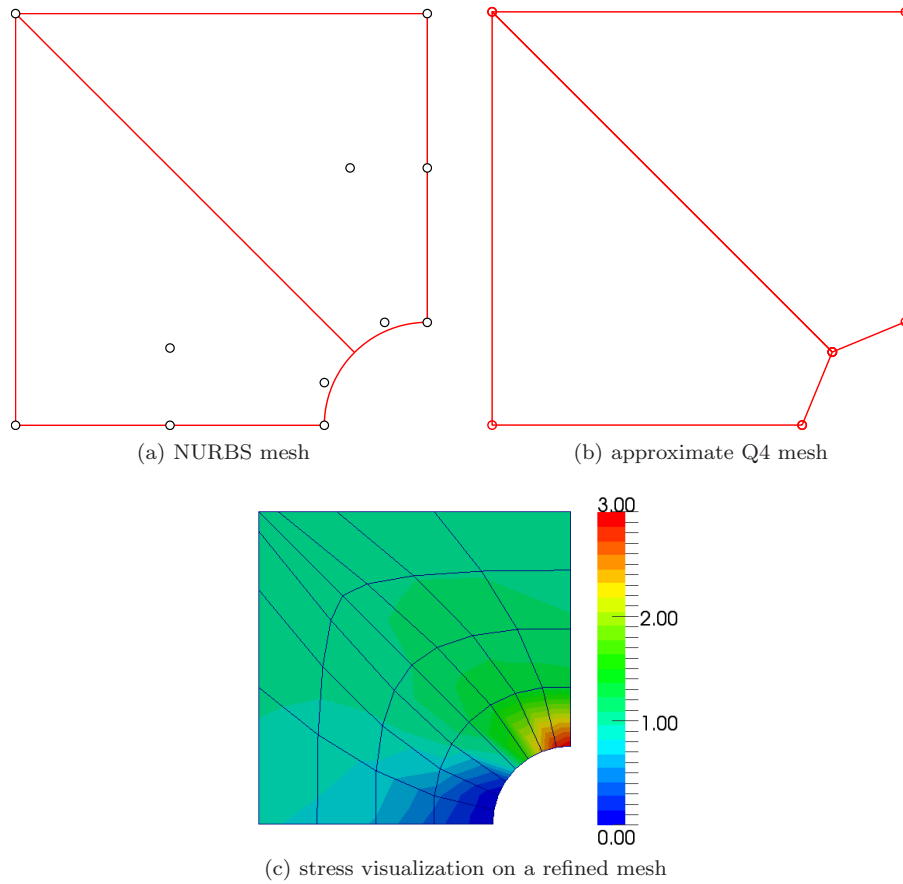


Figure 26: Exact NURBS mesh (top left) and approximate Q4 mesh (top right) for visualization purposes. The nodes in the Q4 mesh are the intersections of ξ and η knot lines. The bottom figure shows a contour plot of the stress field in Paraview. It should be emphasized that the mesh in (b) can not give a smooth contour plot. The result given in (c) was obtained with a refined NURBS mesh (hence a refined Q4 mesh).

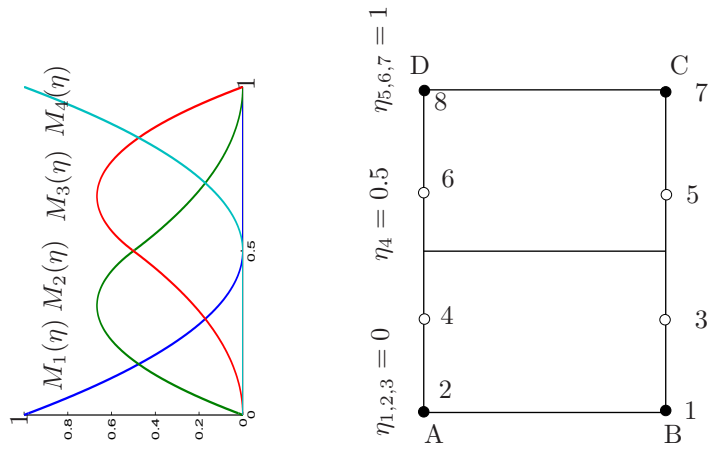


Figure 27: Illustration of imposing Dirichlet BCs. Black points denote corner control points where the NURBS basis satisfy the Kronecker delta property.

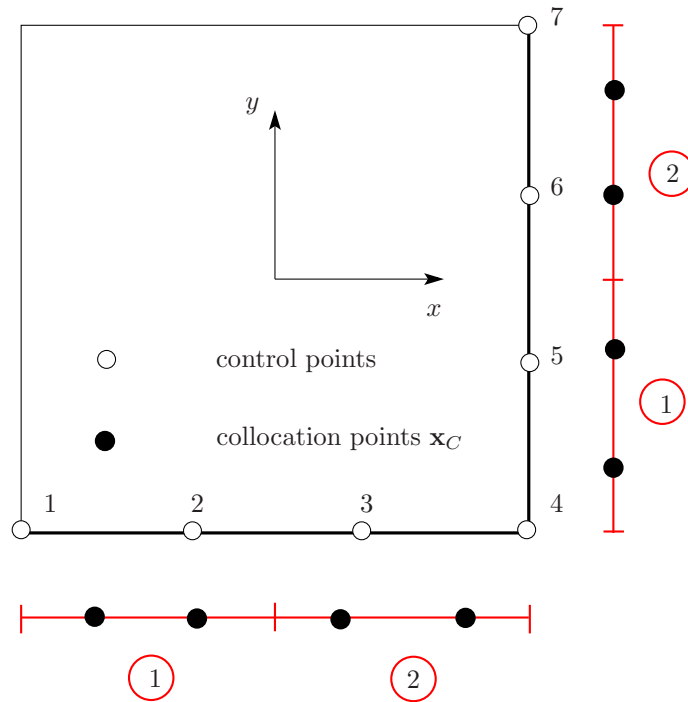


Figure 28: Illustration of the implementation of the least squares method: a quadratic NURBS surface with knot vectors $\Xi = \{0, 0, 0, 0.5, 1, 1, 1\}$ and $\mathcal{H} = \{0, 0, 0, 0.5, 1, 1, 1\}$. Essential BCs are imposed on the bottom and right edges. A one dimensional mesh for this boundary is created. The control points defining the essential boundary are numbered from one to the total number of boundary control points. Note that this numbering is required only for assembling the matrix \mathbf{A} .

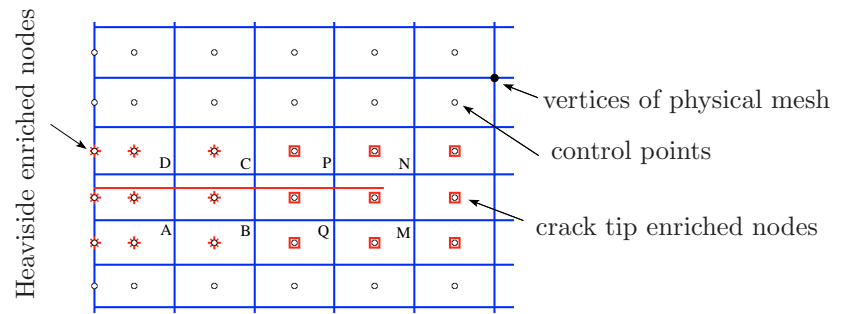


Figure 29: Illustration of enriched node sets \mathcal{S}^f and \mathcal{S}^c for a quadratic NURBS mesh. The thick red line denotes the crack.

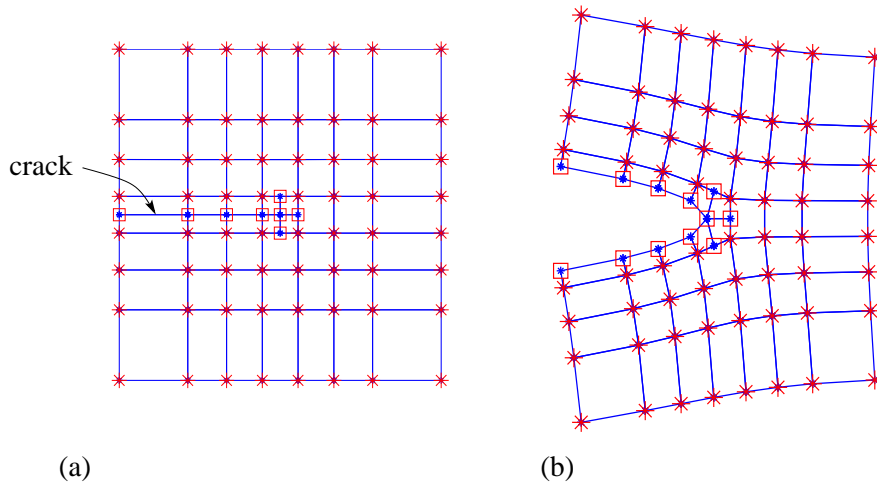


Figure 30: Crack visualization in XIGA: (a) building a mesh that is compatible to the crack by putting double nodes along the crack (square nodes) and (b) the displacement jumps are assigned to these new nodes. Note that the square nodes in the tip element are only for compatibility purposes. Exact mode I displacements are imposed on the bottom, right and top edge using the Lagrange multiplier method while Neumann BCs from the exact stress field are enforced on the left edge. We refer to [59] for a detailed description of this problem.

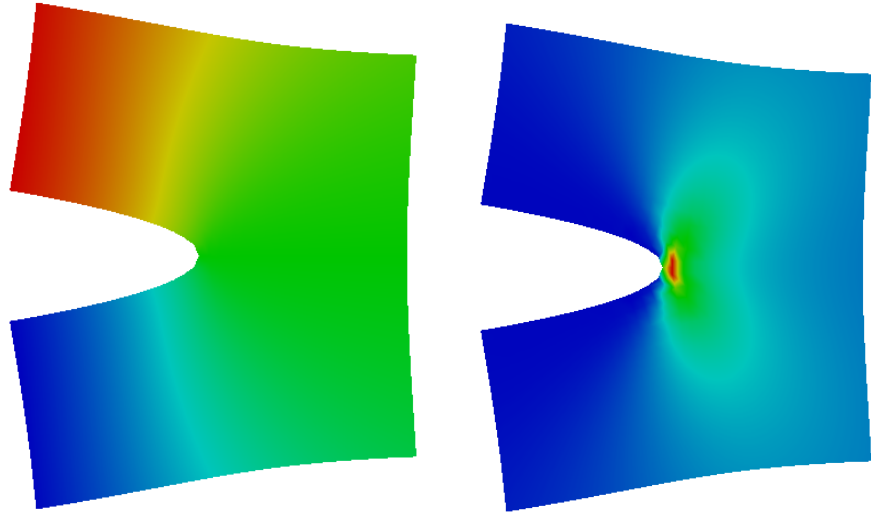


Figure 31: Contour plots on a cracked mesh: (a) vertical displacement and (b) normal stress in the vertical direction.

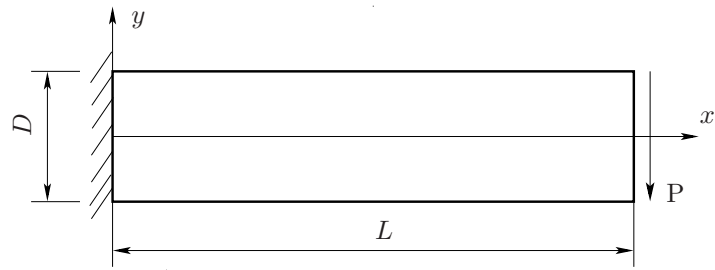
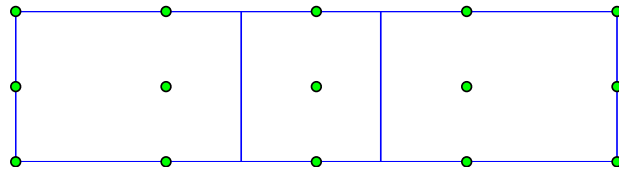


Figure 32: Timoshenko beam.



(a) 3 linear elements



(b) 3 quadratic elements

Figure 33: Initial meshes for the Timoshenko beam. More refined meshes are created from these meshes using a global h -refinement (knot insertion) algorithm.

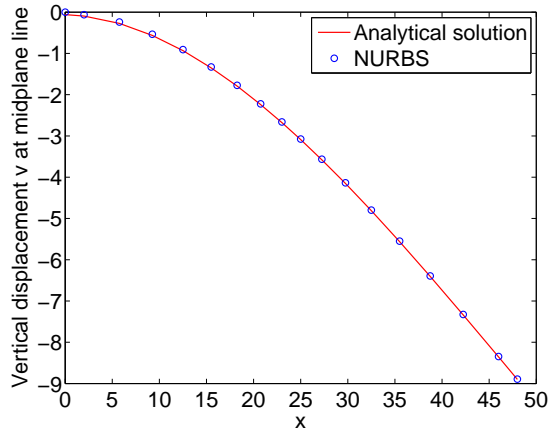


Figure 34: Timoshenko beam: distribution of vertical displacement u_y along the line $y = 0$ and comparison with exact solution. A quadratic NURBS mesh with 360 dofs was used.

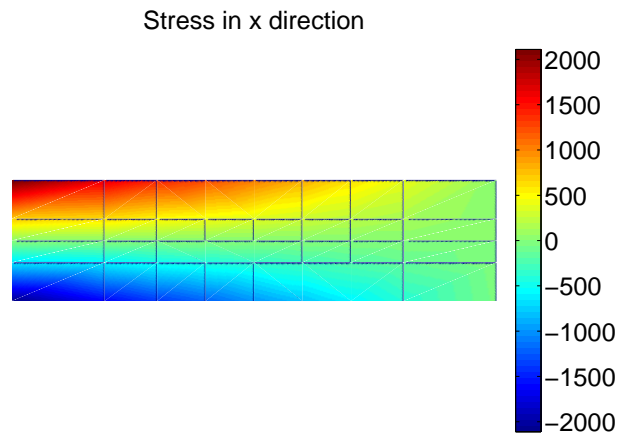


Figure 35: Timoshenko beam: numerical σ_{xx} .

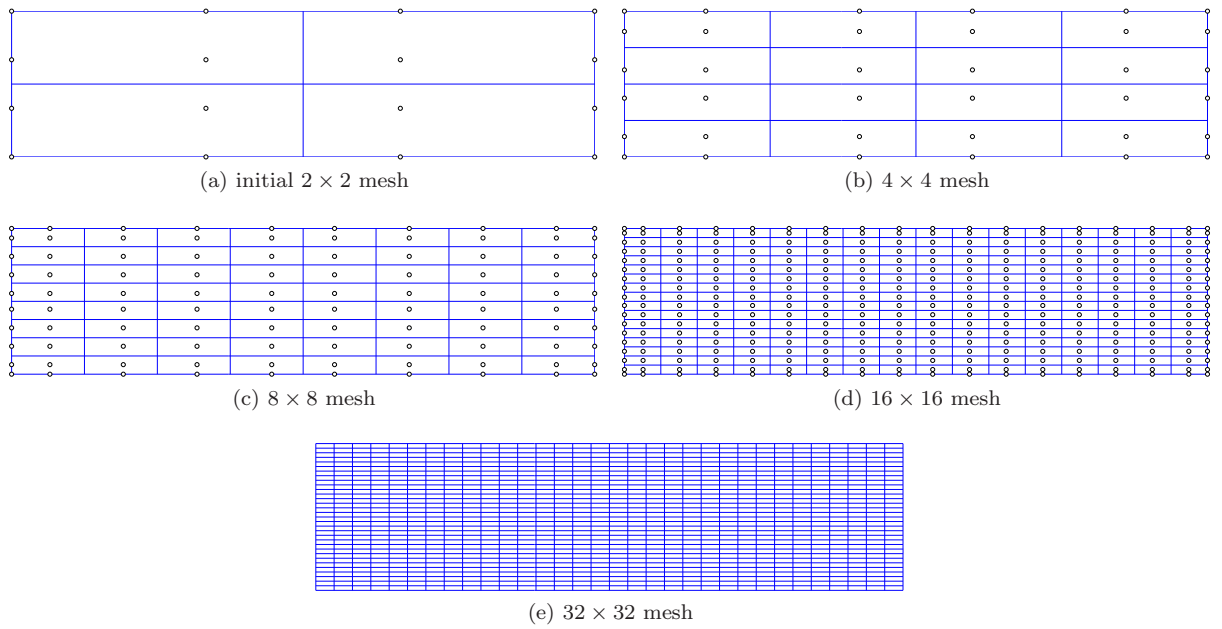


Figure 36: Meshes of the Timoshenko beam for the computation of the energy and displacement norms: (a) initial mesh and (b,c,d,e) refined mesh obtained from (a) using a h -refinement. Circles denote the control points.

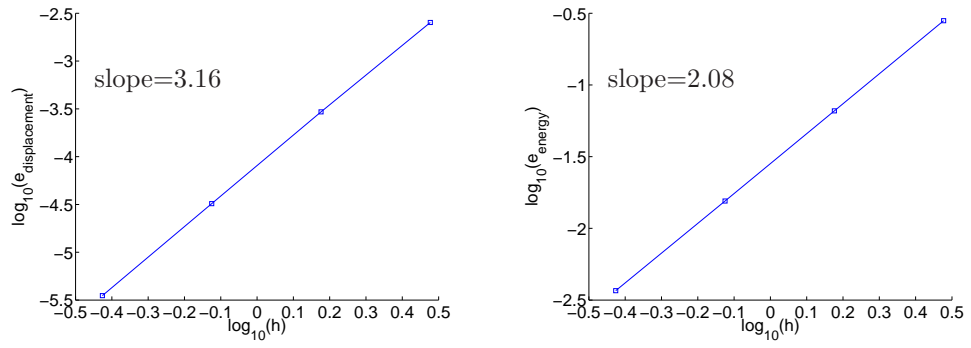


Figure 37: Timoshenko beam: energy and displacement norms. The mesh parameter h is defined as the ratio between the beam height and the number of elements in the vertical direction.

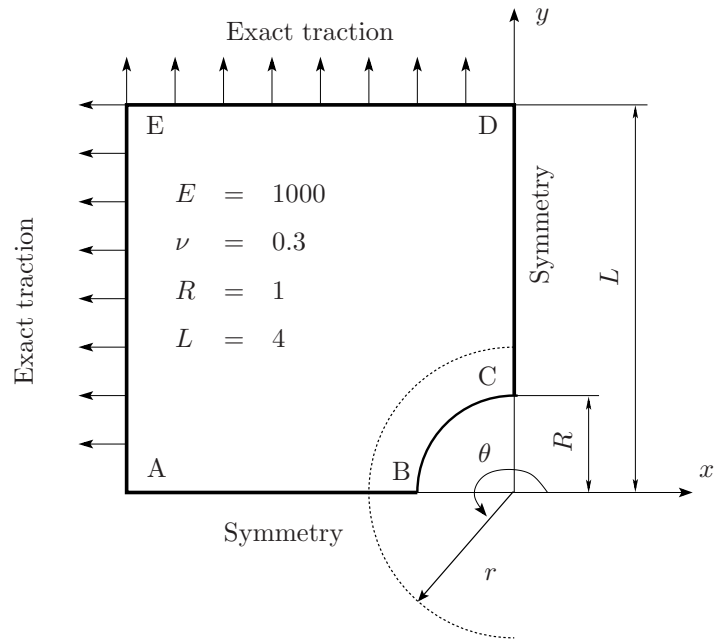


Figure 38: Infinite plate with a circular hole under constant in-plane tension: quarter model. Boundary conditions include: $u_y = 0$ (AB), $u_x = 0$ (CD), $\bar{\mathbf{t}}^T = (-\sigma_{xx}, -\sigma_{xy})$ (AE), $\bar{\mathbf{t}}^T = (\sigma_{xy}, \sigma_{yy})$ (ED).

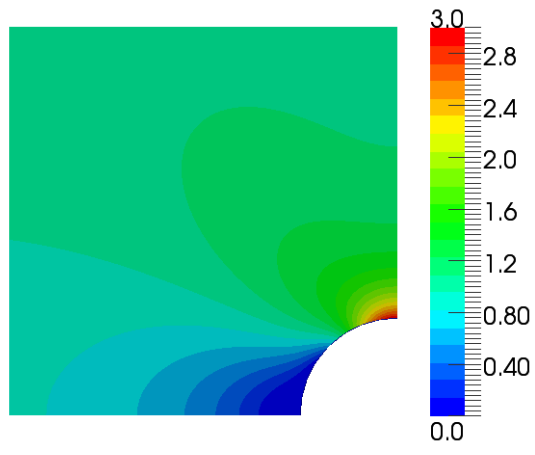


Figure 39: Plate with a hole: distribution of numerical σ_{xx} obtained with a 32×16 quadratic mesh having 4488 dofs.

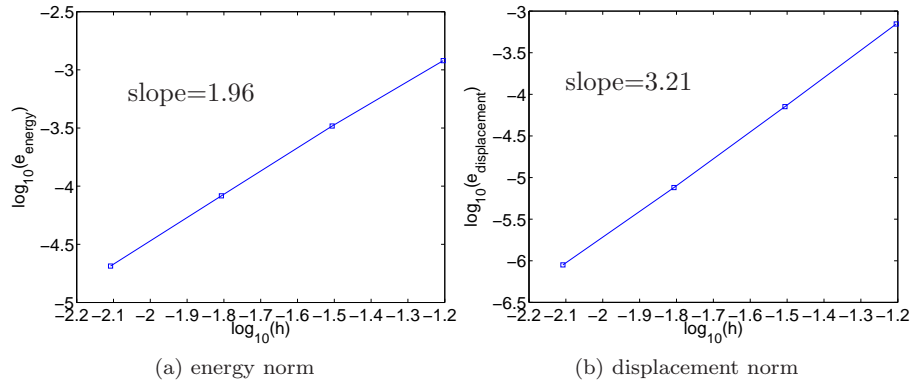


Figure 40: Infinite plate with a circular hole under constant in-plane tension: energy and displacement norms. The mesh parameter h is defined as the maximum distance (in the physical space) between diagonally opposite knots.

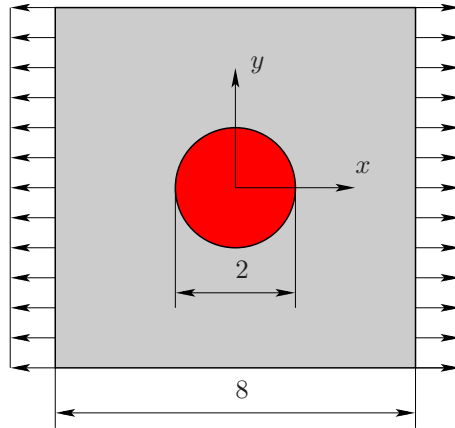


Figure 41: Infinite plate with a circular soft inclusion in uniaxial tension: geometry (square plate with a centered circular inclusion) and boundary conditions.

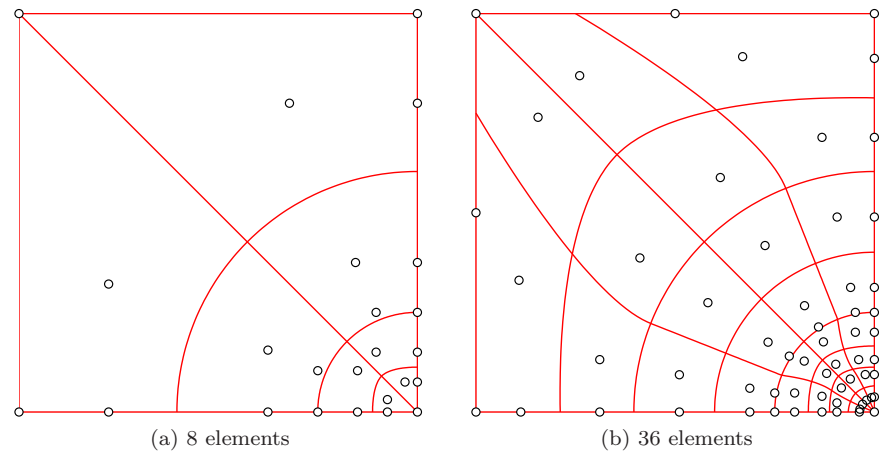


Figure 42: NURBS meshes for the plate with a center inclusion. Circles denote control points. The right mesh was obtained from the left mesh via the knot insertion process.

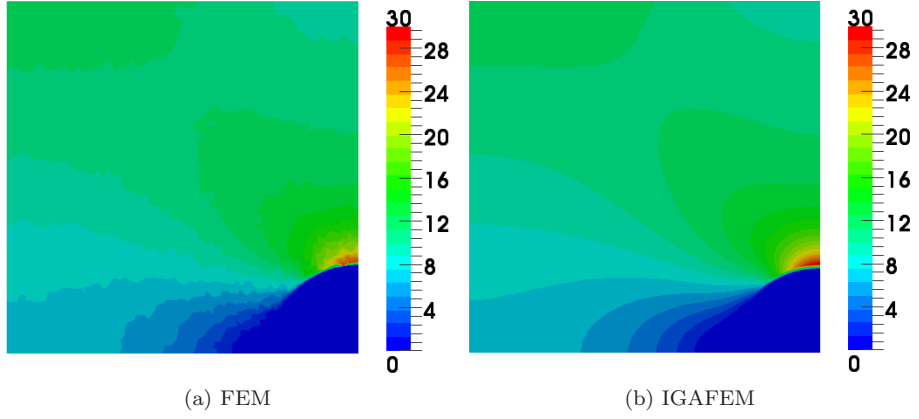


Figure 43: Stress distribution (σ_{xx}) in the plate: FEM and Isogeometric FEM solution.

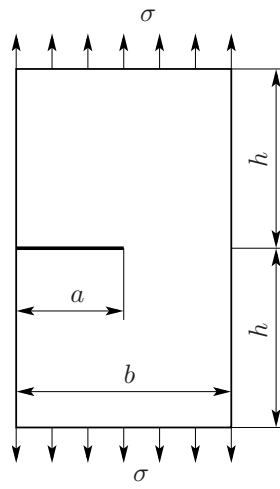


Figure 44: Edge cracked plate in tension: geometry and loading.

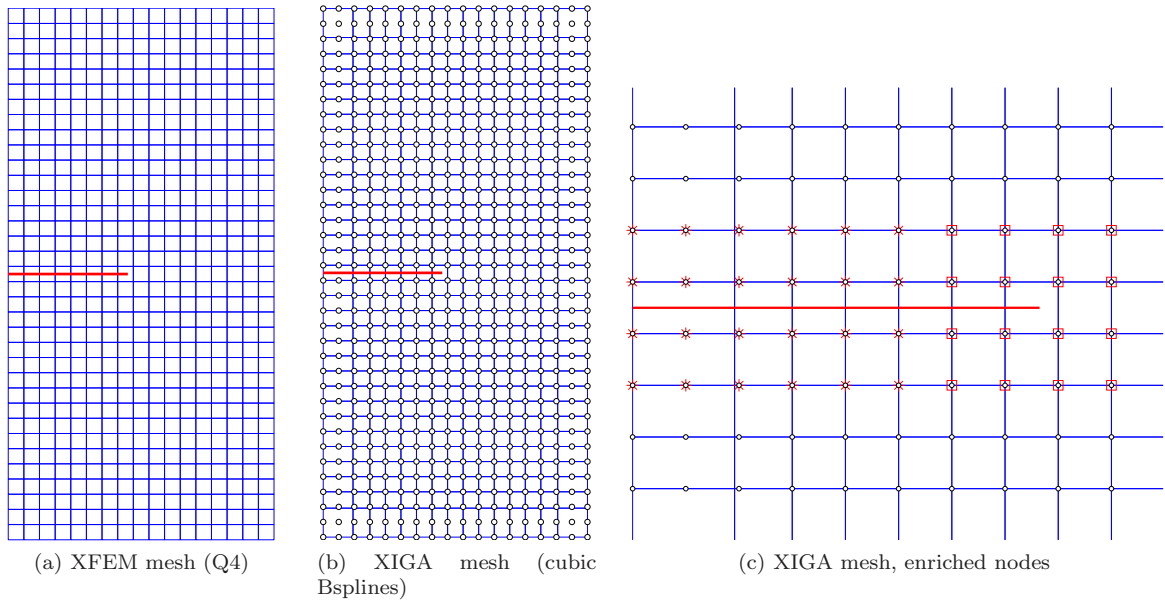


Figure 45: Edge cracked plate: XFEM and XIGA meshes. Both have the same number of displacement dofs of 1296. The thick line denotes the crack. Square nodes denote tip enriched nodes whereas star nodes represent Heaviside enriched nodes.

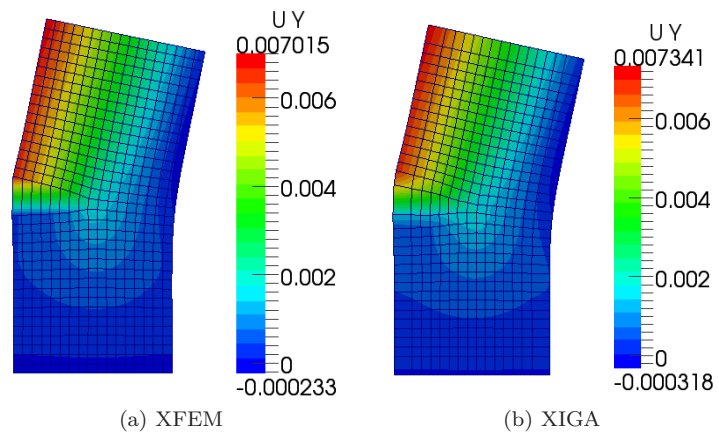


Figure 46: Edge cracked plate: u_y contour plots on deformed configuration (enlargement factor of 30 used).

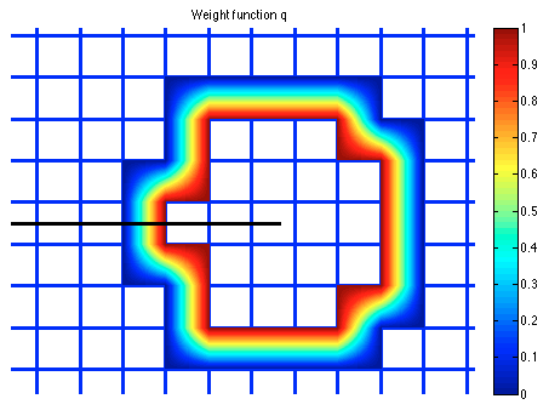


Figure 47: Distribution of weight function used in the computation of the interaction integral. Four-noded quadrilateral elements with bilinear Lagrange shape functions are used to interpolate the weight function.

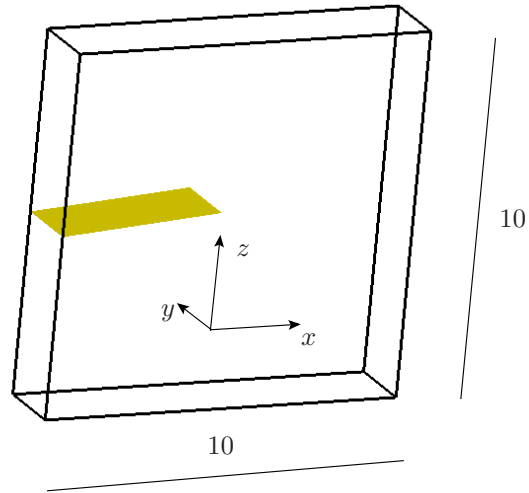


Figure 48: Three-dimensional mode I fracture problem: infinite plate with a center planar crack. The plate thickness is 2, the crack length is 5 and the crack width is 2. The crack is located in the mid-plane of the plate.

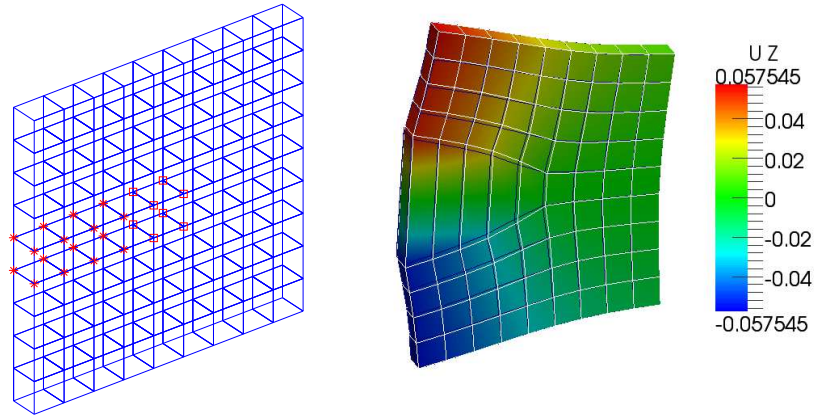


Figure 49: Three-dimensional mode I fracture problem: mesh of linear NURBS elements and enriched control points (left); numerical deformed configuration (magnification factor of 40) superimposed on the exact deformed configuration (right).

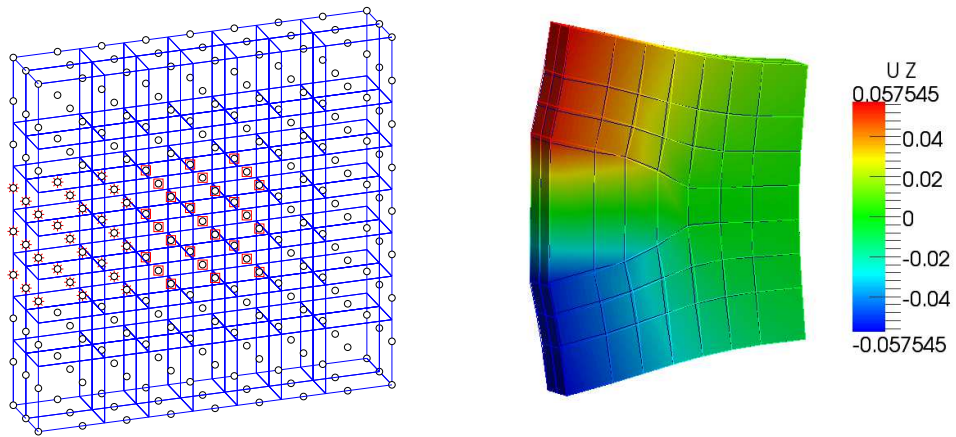


Figure 50: Three-dimensional mode I fracture problem: mesh of quadratic NURBS elements and enriched control points (left); numerical deformed configuration (magnification factor of 40) superimposed on the exact deformed configuration (right).

List of Tables

1 Timoshenko beam: comparison of numerical and exact solutions for the vertical displacement at point $(L, -D/2)$ 113

2 Edge cracked plate: SIFs results. The reference SIF is $K_I^{\text{ref}} = 1.6118$. Note that linear NURBS are equivalent to the conventional bilinear finite elements. 114

mesh	exact	IGA ($p = 1$)	IGA ($p = 2$)
3×1	-0.0089	-0.0052	-0.0082
6×2	-0.0089	-0.0074	-0.0088
12×4	-0.0089	-0.0085	-0.0089
24×8	-0.0089	-0.0088	-0.0089
48×16	-0.0089	-0.0089	-0.0089

Table 1: Timoshenko beam: comparison of numerical and exact solutions for the vertical displacement at point $(L, -D/2)$.

mesh	disp. dofs	K_I (linear)	Error (%)	K_I (cubic)	Error (%)
9×18	324	1.4997	6.96	1.5560	3.46
18×36	1296	1.5823	1.83	1.6150	0.20
36×72	5184	1.5968	0.93	1.6117	0.01

Table 2: Edge cracked plate: SIFs results. The reference SIF is $K_I^{\text{ref}} = 1.6118$. Note that linear NURBS are equivalent to the conventional bilinear finite elements.